



University of
Stavanger

Faculty of Science and Technology

MASTER'S THESIS

Study program/ Specialization: Construction and Materials / Energy	Spring semester, 2012 Open / Restricted access
Writer: Richard Kverneland (Writer's signature)
Faculty supervisor: Bjørn H. Hjertager External supervisor(s): Siri M. Kalvig	
Title of thesis: CFD – Simulations of wave-wind interaction	
Credits (ECTS): 30	
Key words: <ul style="list-style-type: none">• Wind speed• Wave state• Turbulence• Averaging• Sullivan et al. (2008)	Pages: 96 + enclosure: CD Stavanger, 15. June 2012

"The pessimist complains about the wind; the optimist expects it to change; the realist adjusts the sails."

William Arthur Ward (US Author)

ABSTRACT
CFD–SIMULATIONS OF WAVE-WIND INTERACTION

JUNE 2012

RICHARD KVERNELAND

MSc UNIVERSITY OF STAVANGER

Directed by: Professor Bjørn Hjertager and Siri Kalvig

Apart from solar energy, wind energy is the renewable energy which has the greatest potential. Offshore wind power is expected to have an annual growth of approximately 30 % in the decade to come. Even though the offshore wind industry tends to use larger turbines than over land, the standards used in designs, for the rotor-nacelle assembly, are similar to those used for onshore wind turbines. Recent studies by Kalvig et al. and Obhrai et al. (2012) reveal weaknesses in the simplifications made regarding the marine boundary layer (MBL) in the governing industry guidance and standards. Precise knowledge of wind speed is generally important for wind farm design and operations such as design basis, wind site assessment, energy yield assessment and power prediction. Wind profile and turbulence characteristics depend on the wave state, but this is usually ignored and the surface thought of as level and smooth. Field experiments and numerical simulations by Sullivan et al. (2008) and Smedman and Semedo et al. (2009) show that wave state need to be taken into account.

The goal of this study was to develop and use OpenFOAM to improve the understanding of the interactions between atmospheric wind field and surface waves. A Reynold's averaging Navier Stokes (RANS) standard k- ϵ model with the capability to resolve a moving sinusoidal wave at its lower boundary was implemented. It was set up as a 2-dimensional and grid independent case. It was used as a basis for testing several boundary conditions and averaging procedures. Since a transient model is used it is important to know what to do when interpreting the results. What can one get out of snapshots, what should be averaged and how is the averaging done? Interesting patterns in the velocity profile and the turbulence characteristics were looked for in sensitivity studies where different input parameters on the wind speed and wave state were used., A comparison with the LES experiments of Sullivan et al.'s (2008) was performed in order to investigated if the wave modified wind field will be captured with the simpler CFD code?

In order to answer the questions in Kalvig's PhD work to some extent the following research question was defined: "In which way does the sea state influence the wind field in the MBL?"

The answer to this is that surface waves impact the flow field and "footprints" are visible in the whole height of the domain. A "knee" is present as a result of speed up over the wave trough, supported by measurements from Smedman et al. (1999, 2009) and simulations from Sullivan et al. (2008). A good way of averaging was found as there is a need for averaging when studying varying wave parameters and when examining high wind speeds and rough wave states. Wind opposed with the wave propagation is decelerated close to the surface in accordance with Sullivan et al. (2008) and Smedman et al. (1999) and Kudryavtsev and Makin (2004). This implies highest vertical wind and resulting in the highest turbulent kinetic energy in an opposed situation. Although the LES experiment gives the most precise picture, the k- ϵ model used highlights many of the same features.

Using OpenFOAM requires a steep learning curve but the hard work pays off as there are no expensive licenses which other similar programs have. With the results from the sensitivity studies and comparisons with Sullivan et al. (2008) the interdependence of wave and winds, and the ability of the former to influence the flow field, are reflected. This can be used by wind park developers, professionals involved in the offshore industry, and last not least in the further PhD work of Kalvig.

ACKNOWLEDGEMENTS

I would like to make use of this opportunity to thank my thesis supervisor Prof. Bjørn Hjertager for all the guidance and assistance during the work on this thesis. His knowledge in computational fluid dynamics, discussions and help whenever needed has been of utmost value in establishing the model.

Bi-supervisor Siri Kalvig, PhD student StormGeo/UiS, has given excellent remote assistance. Throughout the work she has provided fantastic help and good explanations on several matters. Her enthusiastic approach to this somewhat comprehensive work has made it all good fun.

At UiS I am grateful to Lene Eliassen, PhD student, for clarifications regarding controlling of the power output; Theodor Ivesdal, senior engineer, for providing good service regarding computational issues on setting up the virtual machine; Charlotte Obhrai for systematization and publication of articles and papers on the learning platform “its-learning”.

I want to thank the Norwegian Centre for Offshore Wind Energy (NORCOWE) for allowing me to participate in their work package meeting at Grimstad. During three days I gained an in-depth understanding of wind-wave interactions and their importance for offshore wind energy, and had the chance to meet skilled and helpful people. One of them, Alistar Jenkins, Senior Scientist, Uni Computing, supported the preliminary results and showed how I was on the track of something interesting. In addition, Marwan Khalil, Research Engineer GexCon AS, showed commitment in helping me understand the basics of averaging in a transient CFD simulation.

For help with implementing the moving mesh and on boundary conditions I want to express my gratitude to Eirik Manger, PhD Fluid Flow Specialist, Acona Flow Technology AS.

My employer Norconsult AS has contributed financially and my colleagues and superiors there have facilitated and made it possible for me to complete my master’s degree.

Many thanks to the developers of OpenFOAM for providing the software made use of in this thesis. I am also grateful for the free-ware community www.cfd-online.com. Finally, I would like to express my gratitude to my friends, family and in particular my wife for the love, encouragement and support that I have received.

TABLE OF CONTENTS

1 INTRODUCTION	1
1.1 MOTIVATION.....	1
1.2 BACKGROUND.....	1
1.3 GOALS AND OBJECTIVES	3
2 THEORY	4
2.1 OFFSHORE WIND TURBINES	4
2.1.1 <i>Extraction of wind energy</i>	6
2.2 BOUNDARY LAYERS	7
2.3 WAVES.....	8
2.3.1 <i>Wind sea</i>	8
2.3.2 <i>Swells</i>	9
2.3.3 <i>Range of wave parameters</i>	10
2.4 WIND	11
2.4.1 <i>Wind profile laws</i>	11
2.4.2 <i>Range of wind parameters</i>	13
2.5 WAVE-WIND INTERACTION	14
2.6 COMPUTATIONAL FLUID DYNAMICS - CFD	15
2.6.1 <i>Governing equations</i>	15
2.6.2 <i>Discretisation</i>	17
2.7 TURBULENCE	17
2.7.1 <i>Turbulence length scales</i>	18
2.7.2 <i>Turbulent kinetic energy</i>	18
2.7.3 <i>Turbulence intensity</i>	19
2.7.4 <i>Averaging</i>	19
2.8 TURBULENCE MODELS	19
2.8.1 <i>k-ϵ model</i>	20
2.8.2 <i>Large-eddy simulations</i>	21
2.9 OPENFOAM.....	21
2.9.1 <i>OpenFOAM case structure</i>	22
2.9.2 <i>Fields</i>	22
2.9.3 <i>Dictionaries</i>	22
2.9.4 <i>Mesh</i>	23
2.9.5 <i>Boundary conditions</i>	23
2.9.6 <i>Solver</i>	23
2.9.7 <i>Post-processing</i>	24
3 METHODOLOGY	25
3.1 PRE-PROCESSING.....	25
3.1.1 <i>Mesh generation</i>	25
3.1.2 <i>Boundary and initial conditions</i>	26
3.1.3 <i>Physical properties</i>	27
3.2 SOLVING.....	27
3.2.1 <i>Code formulation</i>	27
3.2.2 <i>Running the code</i>	28
3.2.3 <i>Monitoring</i>	28
3.2.4 <i>Control</i>	28
3.3 GRID INDEPENDENCE STUDY	29

3.4 SULLIVAN ET AL. (2008) SETUP	30
3.5 POST-PROCESSING	30
3.5.1 <i>fieldAverage</i>	30
3.5.2 y^+	31
3.5.3 <i>Residuals</i>	31
4 RESULTS AND DISCUSSION	32
4.1 VALIDITY TEST OF <code>FIELD_AVERAGE</code>	33
4.2 CASE 1, WIND SPEEDS AND DIRECTION	34
4.2.1 <i>Case 1.A, wind speeds aligned</i>	35
4.2.2 <i>Case 1.B, wind speeds opposed</i>	36
4.3 CASE 2, WAVE STATES	37
4.4 CASE 3, SULLIVAN ET AL. (2008)	39
4.5 RESIDUALS	46
5 CONCLUSIONS	47
5.1 CONCLUDING REMARKS	47
5.2 FUTURE WORK	48
BIBLIOGRAPHY	49
APPENDICES	54

LIST OF FIGURES

Figure 1: Vindeby offshore wind farm [21].	4
Figure 2: Parts of an offshore wind turbine [23].	5
Figure 3: Wind flow past a wind turbine [31].	6
Figure 4: Schematic ABL structure in neutrally stratified conditions [24].	7
Figure 5: Sketch showing the solution domain for linear wave theory [45].	9
Figure 6: H_s and related maximum peak period, T_p [47].	10
Figure 7: Wind profiles plotted using the power law (eq. 5) and the logarithmic wind profile (eq. 6) [11].	12
Figure 8: Annual mean wind speed in 80 meters height based on 4 km models from WRF 2005-2006 [51].	13
Figure 9: Effect curve for a Vestas V90 3MW turbine [51].	14
Figure 10: A typical point velocity measurement in turbulent flow [53].	18
Figure 11: Case structure [57, 65].	22
Figure 12: Domain and mesh.	26
Figure 13: Grid independence study, vertical profile of horizontal wind speed and TKE at $x = 125$ m.	29
Figure 14: Grid independence study, horizontal profile of horizontal wind speed and TKE at $z = 15$ m.	29
Figure 15: y^+ on the bottom of the internal mesh.	31
Figure 16: Mean and instantaneous values at several time steps. Wind is aligned with wave propagation. Horizontal profiles of vertical wind speed at $x = 125$ m. Mean is calculated with <code>fieldAverage</code> .	33
Figure 17: Mean and instantaneous values at several locations downstream. Wind is aligned with wave propagation. Horizontal profiles of vertical wind speed. Mean is calculated with <code>fieldAverage</code> .	33
Figure 18: Various wind speeds aligned with wave propagation. Vertical profile of horizontal wind speed and mean horizontal wind speed at $x = 210$ m.	35
Figure 19: Various wind speeds aligned with wave propagation. Vertical profile of mean vertical wind speed and TKE at $x = 210$ m.	35
Figure 20: Various wind speeds aligned with wave propagation. Horizontal profile of horizontal wind speed and TKE at $z = 15$ m.	35
Figure 21: Various wind speeds opposed with wave propagation. Vertical profile of horizontal wind speed and mean horizontal wind speed at $x = 210$ m.	36
Figure 22: Various wind speeds opposed with wave propagation. Vertical profile of mean vertical wind speed and mean TKE at $x = 210$ m.	36
Figure 23: Various wind speeds opposed with wave propagation. Horizontal profile of horizontal wind speed and TKE at $z = 15$ m.	36
Figure 24: Various wave states opposed with wave propagation. Vertical profile of horizontal wind speed and mean horizontal wind speed at $x = 210$ m.	38
Figure 25: Various wave states opposed with wave propagation. Vertical profile mean TKE at $x = 210$ m.	38
Figure 26: Various wave states opposed with wave propagation. Horizontal profile of horizontal wind speed and TKE at $z = 15$ m.	38
Figure 27: Contours of the horizontal wind field for the situation of aligned (top) and opposed with wave propagation (middle), and stationary waves (bottom) from the $k-\epsilon$ model. The non-dimensional field shown is mean U_x / U_g .	39
Figure 28: Contours of the horizontal wind field for the situation of aligned (top) and opposed with wave propagation (middle), and stationary waves (bottom) from Sullivan's LES model. The non-dimensional field shown is mean U_x / U_g .	40
Figure 29: Contours of the vertical wind field for the situation of aligned (top) and opposed with wave propagation (middle), and stationary waves (bottom) from the $k-\epsilon$ model. The non-dimensional field shown is mean U_z / U_g .	41
Figure 30: Contours of the vertical wind field for the situation of aligned (top) and opposed with wave propagation, (middle) and stationary waves (bottom) from Sullivan's LES model. The non-dimensional field shown is mean U_x / U_g .	42

Figure 31: Contours of the pressure for the situation of aligned (top) and opposed with wave propagation (middle), and stationary waves (bottom) from the k-ε model. The non-dimensional pressure field shown is p / U_g^2	43
Figure 32: Contours of the pressure for the situation of aligned (top) and opposed with wave propagation, (middle) and stationary waves (bottom) from Sullivan’s LES model. The non-dimensional pressure field shown is p / U_g^2	44
Figure 33: Vertical profile of the deviation of mean horizontal wind speed from geostrophic wind speed and mean vertical wind speed for the situation of aligned (diamonds) and opposed with wave propagation (triangles), stationary (squares) and no waves (dotted) from the k-ε model at $x = 1050$ m (left) and Sullivan’s LES model (right)	44
Figure 34: Vertical profile of mean vertical wind speed and mean TKE for the situation of aligned and opposed with wave propagation, opposed, stationary and no waves at $x = 1050$ m.....	45
Figure 35: Final residuals “standard-case”	46

1 INTRODUCTION

1.1 MOTIVATION

A major cause of concern for mankind is the energy challenge we are facing due to the rapid depletion of fossil fuels. The Energy Information Administration has estimated that approximately 86 per cent of the world's total energy production results from the burning of fossil fuels [1]. This has resulted in a net increase of 10.65 billion tons of atmospheric carbon monoxide which affects the environmental balance and will to some extent contribute to what is called global warming [2].

The European Union is aiming at reducing its overall emissions to at least 20 % below the 1990 level and increasing the share of renewable energy use to 20% by 2020. One of the most favourable alternatives to fossil fuels is wind energy because it is clean, readily available, renewable, produces no emissions in use and is therefore considered essential to achieve the goals in the Kyoto Protocol. Due to the environmental issues surrounding wind turbine energy, such as their great size and aesthetic disturbance, onshore wind turbine technology is gradually moving offshore. Offshore wind should be considered an incipient market; it is nevertheless growing business and there will be vast investments in offshore wind technology in the near future. Until 2009 only 1500 MW of offshore wind turbines were installed, most of which were pilot projects. Over the next ten years 6000 new turbines will be installed. Even though offshore wind technology has many similarities with wind energy on land, it is still recognized as an immature industry and there are special challenges associated with the offshore environment. In particular we do not know much about how the wave field influences the wind field and hence the potential for harvesting power over the sea [3, 4, 5].

Over the last decade there has been advancement in science and technology which has made it possible to simulate atmospheric turbulence effects on wind turbines. Computational Fluid Dynamics (CFD) has become an important tool for simulation and prediction of wind turbine aerodynamics. As a part of this master thesis, an open source CFD software package called OpenFOAM (see Ch. 2.9 OpenFOAM) will be used for the simulations.

The personal motivation behind this thesis is getting to know a growing and exciting field. As of now there is an interesting development at University of Stavanger (UiS) and Norwegian Centre for Offshore Wind Energy (NORCOWE) in offshore wind turbines. This master thesis will be connected to on-going research activities in the Regional research found project "Better design criteria's and forecast for offshore wind turbines" undertaken by UiS and StormGeo. The supervising team consists of PhD student StormGeo/UiS, Siri Kalvig, and Professor at the Department of Mathematics and Natural Science, Bjørn Hjertager, who are considered cooperative and skilled in many ways.

1.2 BACKGROUND

The wind field over the oceans is commonly thought of as more uniform and less turbulent than over terrain. This might be a valid assumption in some situations, but recent studies of wave-wind interactions by Sullivan et al. (2008) [6] and Smedman [7] and Semedo et al. (2009) [8] shows that the wave state needs to be taken into account in order to simulate turbulence levels [9]. In the design phase, the possible impact of wave modified turbulence is not treated as something of value. This might be the reason why wind parks experience an uncertain power production and unforeseeable dynamic load. The common assumption that neutral stratification gives the lowest fatigue damage on the rotors is questionable, and newly published literature shows that the approach may not hold [10].

To control the aspects mentioned in the above section and for conducting accurate wind energy assessments, careful and punctual estimations of the wind profile is of utmost significance. The energy output is vulnerable to fluctuations because it is proportional to the wind speed in third power, $E \propto U^3$ (eq. 1) [11, 12]. The

difference between planned and actual output for a power producer can vary between 25 and 45 per cent. In such cases, they gain an extra balancing cost that can be about 5 per cent of the total revenues [13].

Wave-wind interaction in the Marine boundary layer (MBL) can have an impact on the offshore wind turbines, which is so far almost unknown. A wind turbine might be exposed to different wind shear and turbulence than it was designed for. In 2008 Sullivan et al. [6] showed “fingerprints” of the surface wave high up in the MBL with a large-eddy simulation (LES) of wind flow over a moving 2-dimensional (2-D) sinusoidal wave [12]. Their results on wind opposing fast moving swells is interesting and will therefore be thoroughly examined in this thesis.

The ability of OpenFOAM to carry out wind simulations was tested in the Bolund experiment where simulation results using this software ranked first and fifth, and it was stated that it has better performance than commercial codes. Bolund is a coastal hill where Risø DTU invited over 50 modellers to a blind test in order to simulate flow over complex terrain. In the Bolund blind test it was concluded that Reynolds-averaged Navier-Stokes (RANS) predictions achieved better overall results than LES [9].

During a project work, Kalvig [9] pointed out the shortcomings with the stationary wave approach and that further research is needed on how wave-wind interactions will influence a turbine. The PhD work of Kalvig started with performing simplified wind simulation over a wave surface and comparing it to a flat surface in order to investigate if some of Sullivan et al.’s [6] features can be seen using RANS turbulence model. It was desirable to simulate swell like movement which resembles a sinusoidal wave (see Ch. 2.3 Waves). A good way of doing this is to perform reliable simulations of wind over different wave states with realistic turbulence and boundary settings for simulation of wave-wind interaction [9].

Different approaches have been tried but the approach that seems most promising is to describe the wave movement in a moving mesh. After implementing the mesh a transient solver called `pimpleDyMFoam` was used in order to handle the movement (see Ch. 2.9.6 Solver). A specification of which wave movement to implement was given to OpenCFD¹ and they slightly modified the code. Fading wave ends were needed in order to ensure stability and was one of the things implemented by Eirik Manger, Acona Flow technology [9]. In this master thesis a larger domain, more realistic inlet conditions and wave state will be used.

Kalvig has performed basic Horizontally Homogeneous Turbulent Surface Layer (HHTSL)² testing and the results match the theory when using OpenFOAM and the $k-\epsilon$ turbulent model [9]. Offshore wind Industry guidance and standards have been reviewed with regards to boundary layer processes in the MBL by Kalvig et al. [10] and Obhrai et al. (2012) [14]. Wave-wind interaction is not taken into consideration in any of the governing offshore wind standards. So far no conclusions have been made about the specific implications the feature gives regarding design considerations. In any case, it has been pointed out that the boundary layer over the sea is quite different from that over land, which is the basis for the governing standards used in the offshore wind industry. It has become clearer that there is a gap between science and codes/standards [10].

Time- and point-specific values for wind speed, U , and turbulent kinetic energy (TKE), k , (see Ch. 2.7.2 Turbulent kinetic energy) give an instant picture and reveal a need for calculating more representative time averaged values. The quality of the picture the TKE-values give was questioned initially and a better estimate of using instant velocity fluctuations over a certain time period was sought (see 2.7.4 Averaging).

¹ OpenCFD is producing the OpenFOAM toolbox in addition to providing support and training for OpenFOAM users [76].

² Horizontally Homogeneous Turbulent Surface Layer is the simplest realistic condition in the surface layer and is here referred to as the HHTSL [9].

There are several standards for the offshore wind energy industry such as Det Norske Veritas (DNV) the Germanischer Lloyd and The International Electro-technical Commission (IEC). The former is the most detailed but the latter has the most widespread use and will be used as a reference in the theory part of this thesis. [15].

1.3 GOALS AND OBJECTIVES

The goal of this master thesis is to improve the understanding of wave-wind interactions applied to offshore wind turbines and seek to make a contribution to the on-going research project mentioned at UiS and StormGeo. The overall research question in Kalvig's PhD work is "Will wave-wind interaction at an offshore wind site result in more turbulence than expected – and if so, how will this affect the turbines?" The research question for this thesis is: In which way does the wave state influence the wind field in the MBL? In order to answer this question, interesting patterns will be investigated in the velocity profile and the turbulence characteristics when winds from different directions are blowing over a moving wave surface. Learning and handling the challenges and complications associated with using OpenFOAM is necessary. As mentioned in the previous chapter, a case study set up with wind flow over moving waves, developed by; Kalvig, Manger and OpenCFD, will be used as a basis for further work. The initial phase of this thesis will largely consist of studying and getting an overview of relevant literature, as well as getting to know some other CFD projects on the same topic.

Several relevant approaches to this task were outlined at the beginning of the thesis. The idea considered most interesting at first was to run one realistic case with different wind inlet conditions and directions, and another with different wave states, named case 1 and 2 respectively, in order to check the sensitivity of the response to wind sea in the domain. If time allows, further comparisons with other CFD simulations like Sullivan et al.'s (2008) [6] LES experiments on swell conditions will be very exciting and instructive. In addition, an effective way of post-processing the turbulence will be sought for. What can be studied without averaging and when is there a need for looking at the mean values?

The objective is to gain an in-depth understanding of the important factors related to turbulence modelling and wave-wind interaction. Although not vital, it is also desirable to achieve which can be used in the on-going PhD work by Kalvig. It can be worthwhile using CFD time series as input to structural design tools in order to test impact on turbine loads and wakes. If averaging the turbulence is shown to be successful, a time series might be given to Lene Eliassen, PhD student at UiS, which can be used for calculating the fatigue load on offshore wind turbines.

2 THEORY

2.1 OFFSHORE WIND TURBINES

Windmills were invented in Persia more than 1000 years ago. They were simple horizontal mills with sails on a vertical axis driving a single pair of stones, for corn crunching, directly [16]. Until today the wind industry has gone through several changes and during the industrial revolution when they were unable to compete with the production of large-scale steam-powered mills [17]. In 1991 the first real offshore wind farm, Vindeby, off the coast of Denmark, consisting of 11 units with a total capacity of 4.95 MW, became operational (see Figure 1) [18]. Statoil's Hywind was the first full scale floating offshore wind turbine [19].

The European Union's primary energy needs are covered by renewable energy resources in a small scale [20]. A potential analysis done by ENOVA³ has estimated the physical potential from offshore wind energy to be 14 000 TWh. Obviously this will be limited by technological capabilities, knowledge and willingness to invest. It is worth mentioning that, by comparison, Norway's annual electricity consumption stands at 125 TWh [11].



Figure 1: Vindeby offshore wind farm [21].

Wind turbines produce electricity by using natural wind power to drive a generator. Wind is an unlimited, clean and sustainable energy source which does not create any pollution after installation. Wind energy technology is under serious development; turbines are becoming cheaper and more powerful, bringing the cost of renewably-generated electricity down.

Almost all wind turbines producing electricity for the national grid consist of three rotor blades which rotate around a horizontal hub. The blades rotate at 10-30 revolutions per minute at constant speed or even more likely at a variable speed. To be protected from damage, machines are stopped at very high wind speeds. Turbines with direct drives are increasingly used but nevertheless turbines with gearboxes are most common. In order to collect as much energy as possible, sensors monitor wind directions and yaw mechanism turns the tower head so that it always faces the wind. Most turbines are upwind turbines; they face into the wind with the nacelle and tower behind. However, there are also downwind designs, where the wind passes the tower before reaching the blades [20].

³ ENOVA is a public enterprise owned by the Norwegian Ministry of Petroleum and Energy which promote, e.g., production of renewable energy [80].

The hub is connected to a gearbox and generator, which are located inside the nacelle. The rotor-nacelle assembly houses the electrical components and is mounted at the top of the tower [22]. This type of turbine is referred to as a horizontal axis wind turbine (HAWT) (see Figure 2).

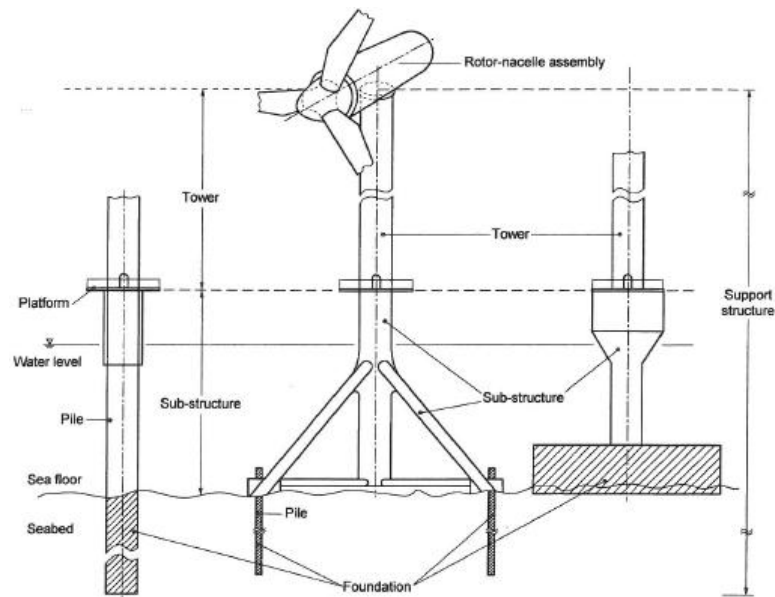


Figure 2: Parts of an offshore wind turbine [23].

The offshore wind industry tends to use larger turbines than onshore. At present, modern wind turbines have a rotor diameter of around 100 meters [24]. Hence there being a need for accurate calculations of wind profiles in the range of 40-160 m in height (i.e., the swept area by the rotor) (see Figure 3). Commercial turbines range in capacity from 3-6 MW. At the planned offshore wind park "Havsul", outside Sandøy municipality in Møre og Romsdal county, 70 wind turbines will be installed, each with an installed output of 5 MW. The wind turbines' rotors are approximately 120 metres in diameter and the hubs will rise about 90 metres above the ground [25].

In offshore wind farms, piles (see Figure 2) with erosion protection are driven into the seabed to take up the environmental loads acting on the structure. The top of the foundation is painted a bright colour to make it visible to ships and has an access platform to allow maintenance teams to dock. Subsea cables take the power to an offshore transformer which converts the electricity to a high voltage (33kV), before running it back to connect to the grid at a substation on land [22].

As mentioned, one of the main challenges with wind energy is that production goes up and down. Wind turbines seem to be most productive in the winter months, which coincide well with period of peak electricity demand [20]. On the other hand high pressure is a frequent occurrence on cold winter days resulting in quiet wind. Storing the excess energy by the use of batteries, pumps to get the water back in the hydropower reservoirs in reservoirs, hydrogen-based energy storage system etc. would be a major benefit. Nowadays, a tremendous effort is made on improving the efficiencies and capabilities of these although the use, so far, is limited as it is more expensive than grid expansion [26, 27].

2.1.1 EXTRACTION OF WIND ENERGY

There are two main methods of controlling the power output from the rotor blades; pitch and stall (passive) control. The former is when the angle of the rotor blades can be actively adjusted by a pitch actuator receiving information on the wind speeds from an anemometer mounted on top of the nacelle. The intention behind this is capturing the energy from the wind most efficiently. The latter method is considered less efficient but more robust because there are no moving parts. It has a locked angle of the blades where the angle of attack⁴ increases until the “stall” is obtained, and the blades lose their lifting power. Due to the simple controlling mechanism, a lesser amount of energy transferred reduces power output at higher speeds [20, 28].

In “Guidelines for Design of Wind Turbines”, [29] efficiency is explained as being “the fraction of wind energy, which is extracted from the wind when it passes through the rotor disc”. In 1919, Albert Betz developed “Betz law”, which states that the maximum kinetic energy converted into mechanical energy by a wind turbine, (i.e., power coefficient) C_p , is 0.59. This is due to the very nature of wind turbines and has nothing to do with design [30]. It occurs when the turbine reduces the wind speed downstream, U_3 , to one-third of the free wind speed, U_0 (see Figure 3). The the electrical power produced by the wind turbine can be written as follows [28].

(eq. 1)

$$P_{turbine} = \frac{1}{2} * C_p * \rho * A * U^3$$

Excluding C_p gives the power of the wind in the absence of the wind turbine. Here ρ is the density of air and $A = \pi R^2$ and U are as shown in Figure 3. Thus that the electrical power is proportional to the square of the rotor diameter and to the cube of the wind speed provided the other parameters are kept unchanged. Representatively the electrical power reaches the rated power (the maximum continuous electrical power, i.e., effective power of the turbine at a wind speed $U \approx 14-15$ m/s [29].

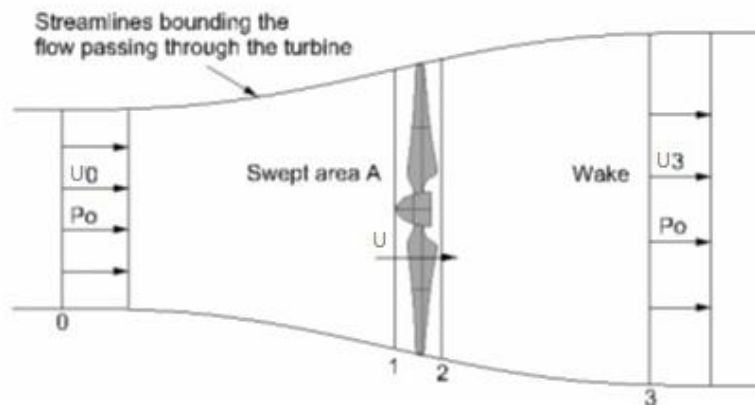


Figure 3: Wind flow past a wind turbine [31].

NEK IEC 61400-1 standard (Wind turbines - Part 1: Design requirements for wind turbines, hereafter named as IEC 61400-1) [32], issued in 2005, defines the swept area, A , as being “the projected area perpendicular to the wind direction that a rotor will describe during one complete rotation”. Thereby it follows from (eq. 1) that that the incline of the wind in the x -direction is critical for the power output. For large rotors the variation in the vertical direction may also make an impact which is not taken account to (eq. 1). In addition the wind flow in the z -direction is significant [33].

⁴ The angle of attack is measured form the chord line, being the straight line from the very front to the end of the aerofoil [28].

2.2 BOUNDARY LAYERS

In order to understand the behaviour of the wind there is a need for understanding the behaviour of the boundary layers and the different characteristics it has over land and over sea. There are two characteristic length scales that apply to the boundary layer. The dominant length scale, in the lower part, is a measure of surface roughness (eq. 7) and the boundary layer height in the part close to the free flow regime. Examining the metocean conditions⁵ is pivotal. The surface of the earth is a boundary in the domain of the atmosphere when we are dealing with numerical methods [9, 34].

Extended research has been carried out to understand the interdependence of the ocean and atmosphere and how the upper ocean responds to the atmosphere and vice versa. The coupled marine boundary layers are driven by a myriad of processes. The Coupled Boundary Layers and Air-Sea Transfer (CBLAST) work of Edson et al. (2007) [35], which was aimed at getting high quality, undisturbed datasets and thereby being able to investigate the air-sea interface, indicated that ocean waves and wave-related processes have a significant impact on air-sea exchange and coupled boundary layer processes even under light wind conditions [35].

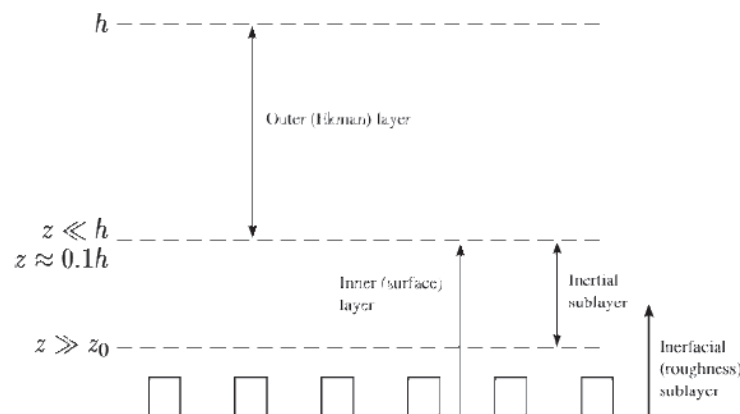


Figure 4: Schematic ABL structure in neutrally stratified conditions [24].

Figure 4 shows several regions in the ABL, such as the interfacial sub-layer, the inner layer and the outer (i.e., Ekman Layer) [24]. Explanations of some important terms follow.

- Atmospheric boundary layer (ABL) – the part of the troposphere that is directly influenced by the presence of the earth’s surface, and responds to the surface forcing’s with a timescale of about an hour or less [36].
- Ekman layer – where the rotation of the Earth (the Coriolis force) plays the major role and the influence of the nature of the surface is minor [24].
- Surface layer - the bottom 10 % of the ABL where the fluxes⁶ are anticipated to vary slightly with height. It may further be divided into an inertial and interfacial sub-layer (see Figure 4) [10, 24].
- Marine boundary layer (MBL) – the part of the atmosphere that has direct contact and, as a result, is directly influenced by the ocean (ABL and MBL are sometimes referred to as the Planetary Boundary layer (PBL) [11] [37].
- Wave boundary layer (WBL) – the layer directly influenced by the waves, where the wave-induced influence cannot be neglected [38].

⁵ “Metocean” is here used as an abbreviation for “meteorological and oceanographic”.

⁶ In this context flux is defined as “flow per unit area, where the flow is the movement of some quantity per unit time” [79].

The depth of the ABL will vary seasonally and diurnally, ranging from 100 m up to 3000 m of the atmosphere. Turbulent motions, on the scale of the boundary layer or less, carry momentum, heat and passive scalars (i.e., dust and pollution). The turbulence (see Ch. 2.7 Turbulence) in this layer is generated by thermal convection and mechanical wind shear [9, 24].

The most noticeable difference found when comparing boundary layers over land with boundary layers over sea is the presence of the waves. Several researchers are investigating how to get a proper prediction of the wind field over the ocean, level of stress from the ocean surface and the appropriate roughness length (eq. 6).

The MBL plays a critical role in regulating and exchanging large amounts of heat, surface energy, moisture and momentum primarily via turbulent transport [37]. Although actual measurements are fragmentary the whole MBL is, to a greater degree than previously assumed, under influence by the fast moving long ocean waves or swells [6, 7, 8].

In previous studies the WBL has been estimated to be of the order of one to two wave heights [38]. However more recent studies have shown that it may be considerably deeper, in particular for light winds [39]. The total momentum flux in the WBL, even if assumed to be constant with height, has appreciable turbulent and wave-induced components [40]. A common assumption is that the same theories that are applied over land should also be valid over sea provided there is a shallow WBL [38], but with the latest finding of how different wave states influences the atmosphere this assumption is probably not valid [6, 7, 8, 10, 39, 40, 41, 42].

2.3 WAVES

When investigating the wave-wind interaction it is essential to have a basic understanding of the behaviour of waves. Waves are irregular in shape; they vary in height, length and speed of propagation. The stochastic wave model reflects the features of a real sea in the best way, see NEK IEC 61400-3 standard (Wind turbines - Part 3: Design requirements for offshore wind turbines, hereafter named as IEC 61400-3 [23]), issued in 2009.

There are two types of waves. Wind sea refers to the generation and growing process related to the local wind, while swells broadly speaking are waves travelling faster than the wind [7]. There is a strong coupling between the wind seas and the local wind field, while swells are not coupled directly and generated remotely [43]. The wave age may be used to distinguish between the two types mentioned.

(eq. 2)

$$\frac{c_p}{u_*} = \frac{c_p}{\bar{U} * \cos \theta}$$

Where c_p is the phase speed of the component in the peak of the surface wave spectrum⁷, u_* is the friction velocity, \bar{U} is the mean wind speed, and θ is the relative angle between the wind and wave directions. The sea state is described as being young/developing or mature when the wave age is under or over 1.2 respectively [38]. This value is often referred to as the equilibrium value which is a rare wave age [6].

2.3.1 WIND SEA

From the calm sea the wind whips up the water on a scale which gives a little ripples and waves. It then transfers more and more energy to the waves while energy moves towards lower frequencies and longer wavelengths. As shown in Figure 5, we can assume that all the waves are similar, monochromatic sea, and resemble a sinusoidal manner and is periodic in both space (wavelength L) and time (period - being the time from one wave crest to another passes the same point) [44, 45].

⁷ A wave spectrum describes the total energy transmitted by a wave field at a given time [45].

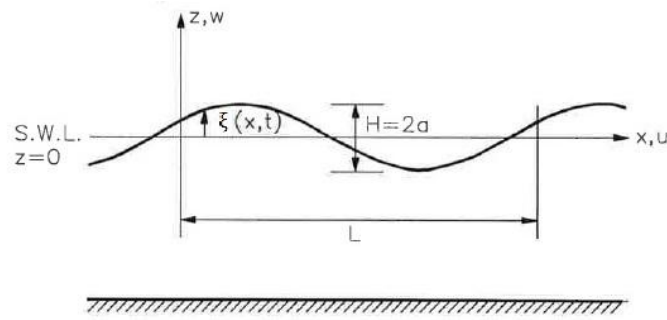


Figure 5: Sketch showing the solution domain for linear wave theory [45].

Although it is restricted by simplifying assumptions, linear wave theory is applicable for a wide range of cases. The wave profile on its simplest form is;

$$\xi = \xi(x, t) = a * \sin(kx - \omega t) \tag{eq. 3}$$

where a is the amplitude, x is position in the longitude direction, t is time and ω is the wave angular frequency [45]. It is found that the theoretical steepest wave is $a/L \approx 1/14$ [46]. The short-crestedness of wind-induced waves may be described as a spreading function [47]. Nevertheless in this context, where the wave is assumed to be 2-D and small with respect to the water depth, the linear dispersion relation gives a good description [45].

$$c^2 = \frac{gL}{2\pi} \tag{eq. 4}$$

Where g is the gravitational acceleration and c is the phase speed of the moving wave i.e., wave speed [45]. In this context c is equal to c_p as a result of the assumption of a monochromatic sea.

2.3.2 SWELLS

Recent wave climate studies has revealed swell to be predominant on the world oceans and prevalent almost at all times [39]. When the wave speed of sea waves overcomes the overlaying wind speed, the waves radiate across the ocean basin as swells. They are therefore characterized, in contrast to wind sea, by longer periods and faster wave speed (long-crested). Because the local wind direction is not correlated with the swell direction, swells will occasionally oppose the wind field. Swell conditions may apply if the wind speed is relatively low, less than 5 m/s, and the wave age is greater than 20. [24, 48].

Swell produced by a storm can travel for thousands of kilometres across the ocean, carrying considerable energy. Swell propagating into a light wind observation region has a period and wavelength that is not associated with the local wind field. Grachev and Fairall [38] have shown that swells dramatically affect the wind field. Swells have a non-linear behaviour because of their dissipation of energy [38, 48].

Recently there has been a renewed interest in the study of swell from propagation and to the swell impact on the MBL. In 2008, Makin [49] concluded that under certain swell parameters the impact of swell can be significant and even change the structure of the entire ABL. The swell energy dominates the overall wave

energy field. Semedo et al. (2011) [43] used ERA-40⁸ data for 6-hourly global fields for atmospheric variables and wave parameters. The 6-hourly gridded values of wind and wave parameters were processed to seasonal means, organized as December, January and February (DJF) and June, July and August (JJA). It is clear from the the significant wave height (H_s^g) for swell and wind sea (H_s^s and H_s^w) seasonal fields, that H_s^s are always larger than the H_s^w (see Appendix A). The figures further shows that wind sea and swells are physically independent, and their maxima occur in different regions, therefore their low correlations are not surprising. [43].

2.3.3 RANGE OF WAVE PARAMETERS

In IEC 61400-3 the marine conditions are divided into two categories; the normal marine conditions which occur more frequently than once per year during normal operation, and the extreme marine conditions which are defined as having a 1-year or 50-year recurrence period.

Vikebø et al. (2002) [50] has analysed Norwegian Meteorological Institute (DNMI) annual maximum H_s based on 6 h values. It indicates continuously increasing wave heights and rougher wave climate off the coast of mid-Norway in the last 45 years of the 20th century. Measurements from station 4 and 5 at position 2.07 E, 60.88 N and 7.17 E, 65.14 N in the North Sea shows DNMI hindcast¹⁰ annual maximum H_s , with linear regression from 1955-1999, to be about 10,2 m and 10,4 m respectively. Havsul is located between these two stations, somewhat closer to station 4.

Figure 6 below shows H_s for the North Sea with annual propility of exceedance of 0.01 for wave states of 3 h duration. Isocurves for wave heights are plotted with solid lines while wave period lines are dotted [47].

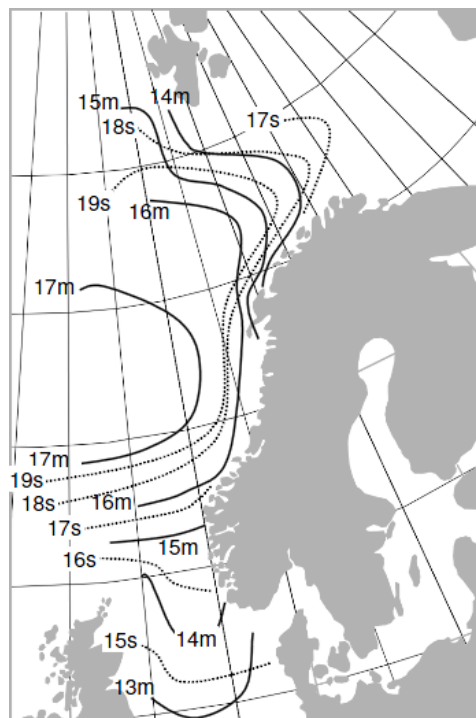


Figure 6: H_s and related maximum peak period, T_p [47].

⁸ ERA-40 is a reanalysis of meteorological observations from September 1957 to August 2002, produced by the European Centre for Medium-Range Weather Forecasts (ECMWF) [43].

⁹ H_s is the mean of the highest (trough to crest) third of all individual waves in a record [34, 49]

¹⁰ Hindcast is a “method of simulating historical (metocean) data for a region through numerical modelling” [23].

When examining the damage on the turbine extreme values as described above are of interest, while average values should be looked at when studying energy output. Based on the work of Semedo et al. (2011) [43] average values of H_s outside the west coast of Norway are found to be as listed in the table below (see Appendix A).

Table 1: Average H_s for waves, swell and wind sea, outside the west coast of Norway, during summer and winter [43].

	DJF	JJA
H_s [m]	3	1,4
H_s^s [m]	2,2	1,0
H_s^w [m]	1,5	0,5

2.4 WIND

To ensure an optimal configuration of a wind park, as well as optimal power harvesting, wind mapping and wind forecast are essential. The wind climate can be described by the following three categories; micro-scale as being less than 2 km, the meso-scale as 2-2000 km and macro-scale as 2,000-20,000 km. On the two former convective up- and downdrafts called cells and longitudinal roll vortices can lead to organized convective precipitation [37].

The design requirements for offshore wind turbines use the Charnock relation (eq. 7) to some degree. However, they do not take into account how the wave state can directly affect the wind profile and the turbulence. The differences in the momentum and heat fluxes over sea versus land and how this affects the rotor-nacelle assembly are neither taken into account [10].

2.4.1 WIND PROFILE LAWS

The IEC standards for wind turbines state that both normal and extreme wind conditions need to be considered. The wind profile is given by the power law and IEC 61400-3 refers to IEC 61400-1.

(eq. 5)

$$\bar{U}(z) = U_{hub} \left(\frac{z}{z_{hub}} \right)^\alpha$$

Where $\bar{U}(z)$ ¹¹ is the mean wind speed at a height z over seawater level, U_{hub} is the wind speed at the hub height, z_{hub} , and α is the power law exponent. For normal wind conditions offshore $\alpha = 0.14$ [23]. The power law is an empirical function proved to fit the logarithmic wind profile [10].

The logarithmic wind profile only accounts for the surface roughness, and is therefore only valid up to 50-100 m above terrain. It assumes a flat terrain upstream and geostrophic wind, U_g ,¹² wind being constant with height (i.e., barotropic). These neutral conditions (see [24] for non-neutral conditions), combined with the oft-used Monin-Obukhov similarity theory, lead to the following useful expression for the logarithmic wind profile;

(eq. 6)

$$\bar{U}(z) = \left(\frac{u_*}{K} \right) \ln \left(\frac{z}{z_0} \right)$$

¹¹ Notation for wind speed, V , used in IEC standards is consistently changed to U in this thesis.

¹² Geostrophic wind is the balance between the pressure gradient force and the Coriolis force [36]. The wind flow is hence parallel to the isobars and unaffected by the surface [11].

where $K = 0.4$ is the Von Kármán constant [10, 24]. It does however not hold for swell conditions because it overlooks the wind-following swell effect [11, 39].

By the use of power law (eq. 5) and the logarithmic wind profile equation (eq. 6), the wind speed in typical hub height, e.g., in 100 m, will be largest by the use of the former. Figure 7 shows wind profiles over land giving the highest wind speed values above reference height ($z = 10$ m). Blue curves indicate z_0 and α values that are recommended to use over sea and curves with typical values for land are red (reference wind speed average over 10 min, $U_{ref} = 10$ m/s) [11].

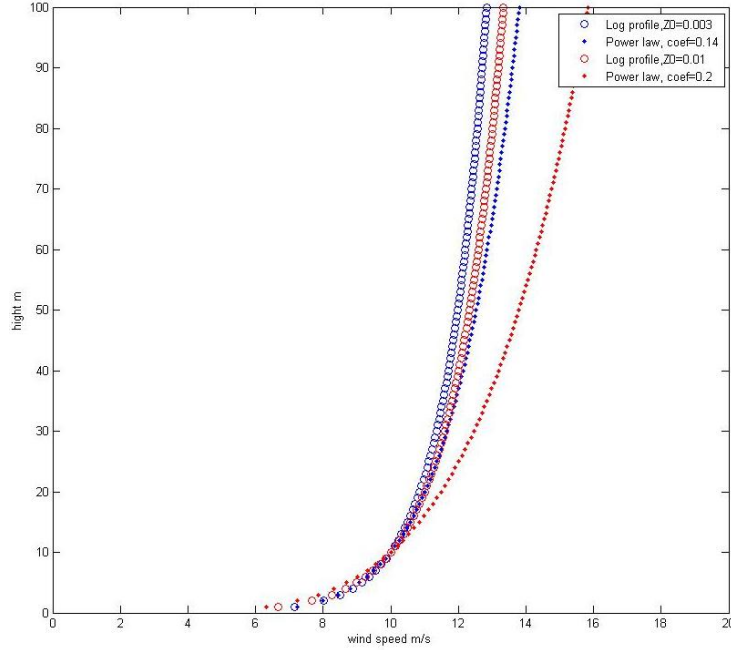


Figure 7: Wind profiles plotted using the power law (eq. 5) and the logarithmic wind profile (eq. 6) [11].

In IEC 61400-1 roughness length, z_0 , is defined to be “extrapolated height at which the mean wind speed becomes zero if the vertical wind profile is assumed to have a logarithmic variation with height”. The surface roughness onshore is only a function of the surface characteristics, while it increases with wind speed and hence increasing wave height offshore [15]. Measurements of wind speed at various heights are the only true way of determining the parameter, which is not really a physical length and should therefore rather be treated as length-scale [24]. IEC 61400-3 recommends expressing the surface roughness by the use of the Charnock relation and then using this for calculation of the turbulence, when there are no observations available. The Charnock relation, based on dimensional reasoning, defines the relationship between the surface roughness and wind speed in the following way.

(eq. 7)

$$z_0 = \frac{A_c u_*^2}{g}$$

Where g is the acceleration due to gravity and the empirical constant, A_c is the Charnock constant. The Charnock constant in open sea is recommended to be 0.011 and for near coastal waters 0.034 [23]. The last component in the above equation is the friction velocity u_* and is defined as;

(eq. 8)

$$u_*^2 \equiv \frac{\tau_0}{\rho}$$

where τ_0 is the force per unit area exerted by the ground surface on the [11, 24].

2.4.2 RANGE OF WIND PARAMETERS

The wind conditions vary geographically and over time. The wind regime is divided into the same categories of recurrence period as used for waves (see Ch. 2.3.3 Range of wave parameters). Long term observation sets are important in order to identify the normal wind conditions in an area. Over the sea there are not as many observations as over land and therefore the use of “virtual observation” is much more common. Numerical weather forecasting models can be used in order to create such “virtual observations” and hence long term time series of weather conditions on specific locations. The hindcast archive was created by forecasting models in historical modus and is used in order to identify extreme values of wind (and waves) over the sea.

Simulations with a meso-scale weather forecasting model the “Weather Research and Forecasting model” (WRF), show the annual mean wind speed in the North Sea in 80 meters height to be around 10 m/s (see Figure 8).

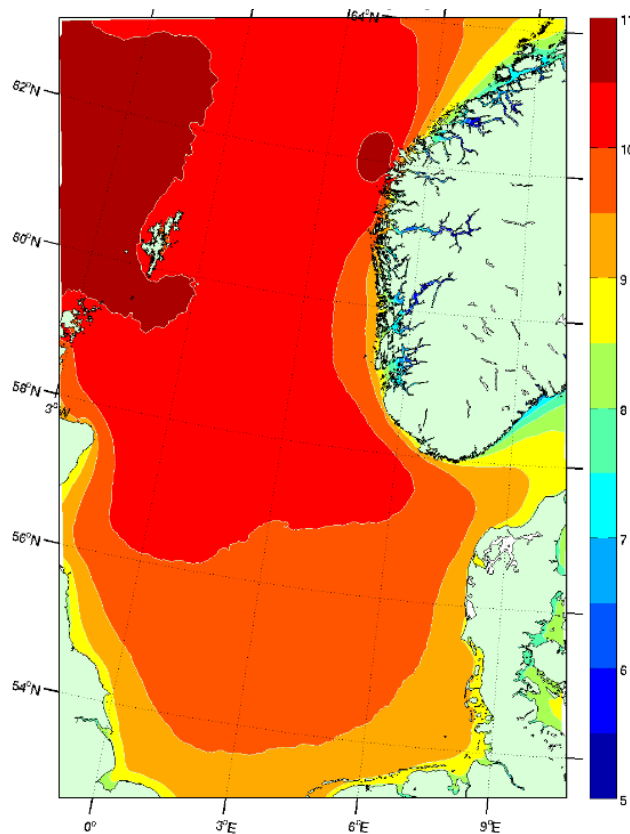


Figure 8: Annual mean wind speed in 80 meters height based on 4 km models from WRF 2005-2006 [51].

It is common to use a cut-out hysteresis by shutting the turbines when wind speed exceeds 25 m/s, U_{out} , and resume production when the wind speed is below 20 m/s, U_{in} (see Figure 9) [32]. Outside Stadt on the Norwegian coast, the wind speed exceeds the cut out speed 100-150 hours per year [51].

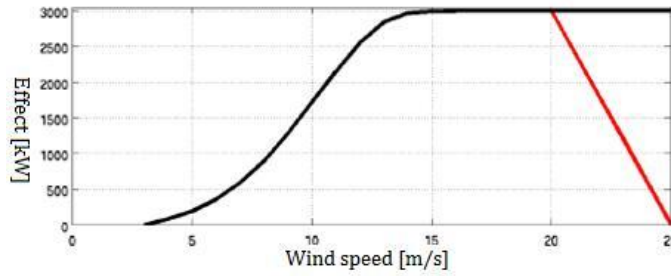


Figure 9: Effect curve for a Vestas V90 3MW turbine [51].

National Oceanic & Atmospheric Administration (NOAA), Minerals Management Service (MMS) and the Petroleum Safety Authority Norway (PSA) require that all installations on the Norwegian continental shelf to be undamaged after a hundred year storm. The wind speed that statistically occurs once in a hundred year period can be up to 40 m/s, but is not equal all over the Norwegian continental shelf. All facilities built after 1984 must also withstand a ten thousand year storm without major security breakdown and without injuries to personnel – or significant contamination. The wind force that statistically would occur once during a ten thousand year period can be up to 50 m/s [52].

2.5 WAVE-WIND INTERACTION

Conventional theory used onshore describes the wind field in the MBL insufficiently. The influence the mobile sea surface has on the velocity profile and the TKE is not yet satisfactorily explained, despite many studies. Determining energy transfer from wind to waves and from waves to wind is rather comprehensive. As a consequence, metocean models often neglect the wind/wave/current coupling mechanisms. These wave-induced processes are important for both the shape of the wind profiles and the turbulent characteristics – two features that are of great important for offshore wind energy harvesting. An empirical sea state dependent drag coefficient has been used, but it is not thoroughly understood. In the presence of waves the air flow is influenced by a wave-induced stress [38, 40, 41].

A parameterization of the total wind stress can be;

$$\tau = \rho C_D \overline{U}^2 \quad (\text{eq. 9})$$

where C_D is the surface drag coefficient for the given height. The surface drag relies on the sea state. Forecast and hindcast needs a decent parameterization as a basis for atmospheric modelling [10, 11].

In 1998 Janssen [41] studied resonant wave-mean flow interaction using quasi-linear theory of wave-wind generation. It was found that the coupling between the waves and wind was sensitive to how the energy level of the high-frequency wave depends on the wave age and the strongest coupling was seen for a young sea state. In addition it was stated that the stress in the ABL varies by a factor of two depending on the sea state and the effect of the long waves on the airflow must be taken into account. The CBLAST campaign proved that disequilibrium between the wave field and local winds was concluded to be more likely when winds are light.

During swell conditions the wind can both be aligned and opposed with the direction of the swell (see Ch. 2.3.2 Swells). The flow response to these two situations is radically different. With the former, the resolved form stress is negative while it is positive in the latter. As mentioned in the last section, the advanced coupling mechanisms between the horizontal wind and waves result in a speed up above each wave trough when aligned. In contrast, opposed winds in the surface layer are slower and the resultant drag coefficient is less by a factor of four compared to an aligned situation and results in deviations from the geostrophic winds in the top of the domain. Swells opposing surface winds generate turbulence variances larger than a neutrally flat surface [6, 10].

2.6 COMPUTATIONAL FLUID DYNAMICS - CFD

In “An Introduction to Computational Fluid Dynamics” [53] CFD is explained as being “the analysis of systems involving fluid flow, heat transfer and associated phenomena by means of computer-based simulation”. Due to its complexity it requires high performance hardware¹³ and has therefore had resurgence in the last two decades. Numerical algorithms are used to solve the problem and normally different codes contain three main elements.

- 1) Pre-processor – consists of the input and involves activities as defining the geometry (domain), grid generation (a grid of cells), selection of the phenomena to be modelled, definition of fluid properties, and specification of boundary conditions.
- 2) Solver – numerical solution technique, in our case the finite volume method, includes integration of the governing equations, discretisation (converting integral equations into system of algebraic equations), and solving of algebraic equation.
- 3) Post-processor – graphics, e.g., vector plots, contour plots, surface plots and particle tracking and animation for dynamic result display [53].

All fluid flows are governed by three fundamental principles;

- Conservation of mass
- Conservation of energy (1st law of thermodynamics)
- Newton's second law (force equals the rate of change of momentum).

By the use of these principles one can derive the Navier-Stokes (NS) equation which is a set of partial differential equations that describes the flow of a fluid. Determine numerical solutions to the NS equation that can be propagated in time and space are the main issue of CFD. The following governing equations should be solved on a grid inside the region of interest [24, 53].

2.6.1 GOVERNING EQUATIONS

This chapter will briefly describe the governing equation solved with focus on incompressible flows. The dependent variables in a 3-dimensional (3-D) numerical analysis are;

p	pressure
T	temperature
μ	viscosity
γ	heat conductivity
ρ	density
u	velocity in x-direction
v	velocity in y-direction
w	velocity in z-direction

Transport equations for momentum, enthalpy, TKE (eq. 21) and dissipation of TKE are to be solved. In each control volume¹⁴ mass balance is satisfied. In total there are 8 unknown variables and therefore 8 equations are needed for solving CFD-problems [24, 53, 54].

¹³ The computational cost is proportional to Re^3 [24].

¹⁴ Control volume refers to one grid cell of the computational domain and is determined by the local grid resolution [24].

Eq. 1 - Conservation of mass (continuity equation)

(eq. 10)

$$\frac{\partial \rho}{\partial t} + \nabla(\rho \vec{u}) = 0$$

Eq. 2, 3 and 4 - Momentum balance in x, y and z- directions (on vector form)

(eq. 11)

$$\rho \frac{D\vec{V}}{Dt} = -\vec{\nabla}T + \vec{\nabla}\vec{\tau} + \vec{F}$$

\vec{V} is the velocity vector, $\vec{\tau}$ is the viscous stress vector and \vec{F} is the force.

Eq. 5 – Conservation of energy (on differential form)

(eq. 12)

$$\frac{\partial(\rho h)}{\partial t} + \frac{\partial(\rho u_j h)}{\partial x_j} = -\frac{\partial q_j}{\partial x_j} + \frac{Dp}{Dt} + \tau_{ij} \frac{\partial u_i}{\partial x_j} + \dot{S}$$

\dot{S} is the source term and h is enthalpy. The index (i, j) in 2-D directly addresses each cell in the grid, saving computational effort [55].

Eq. 6 - Equation of state (general transport equation)

(eq. 13)

$$\frac{\partial(\rho\varphi)}{\partial t} + \frac{\partial(\rho u_i \varphi)}{\partial x_i} = \frac{\partial}{\partial x_i} \left[\Gamma_\varphi \frac{\partial \varphi}{\partial x_i} \right] + S_\varphi$$

φ is a general variable and Γ is the transport coefficient.

Eq. 7 and 8 - Empirical relations for μ and k

Viscosity is a measure of the internal resistance between neighboring fluid particles [56]. In a Newtonian fluid the viscous stresses and the rate of deformation are proportional. All variables are split into a mean and a fluctuating part (see see Figure 10). This is called Reynolds decomposition. The time average of the fluctuating part is introduced (Reynolds averaging, see Ch. 2.7 Turbulence) into the general transport equation (eq. 13).

For incompressible flows there are no relation between pressure and density. A reference pressure, p_0 , is used to obtain the density from the ideal gas law.

(eq. 14)

$$\rho = \frac{p_0}{RT}$$

The temperature, T, is in Kelvin and R is universal gas constant. When using the finite volume approach to discretise the momentum equation (eq. 11), one can say the pressure is acting as a surface force. As there is no equation for pressure, it is common to use an iterative procedure, such as PIMPLE, to solve the “pressure problem” (see Ch. 2.9.6 Solver) [24, 53].

2.6.2 DISCRETISATION

Discretisation is the heartbeat of finite volume methods. All equations which are to be solved must be discretised, which can be described in three steps. The first step is to generate a grid with control volumes. A system of notations for the point of interest and neighbouring points must be established. The clever trick is step 2 of integrating the governing equations. It is done over the control volume yielding a discretised equation at its nodal point. The discretised equations have a clear physical interpretation - mass balanced over the control volume. Central differencing is the simplest way of calculating gradients at the control volume faces as it uses linear approximation [53].

Each nodal point must involve a discretised equation to approach step 3. The distribution at nodal points is the resulting system of linear algebraic equations, a matrix M , given by;

$$q = M^{-1} * y \quad (\text{eq. 15})$$

where q is a vector of q values at next time step (unknown), M is an $N \times N$ matrix and y is a source vector. This is solved by any suitable matrix solution technique (see Ch. 3.2.1 Code formulation) [53, 57].

2.7 TURBULENCE

Turbulence is “a state of continuous instability”. When turbulence is present, it usually dominates all other flow phenomena and results in increased energy dissipation, mixing, heat transfer, and surface drag. The processes in the atmosphere, is a chaotic and random state of motion which, takes place at higher Reynolds numbers, Re (eq. 16) [53, 56, 58].

The three dimensional quantities describing a flow are characteristic length and velocity, d and $|U|$ respectively, and kinematic viscosity ($\nu = \mu/\rho$, which for air differ according to temperature). The Reynolds number is a dimensionless combination of these parameters [56, 59].

$$Re = \frac{d|U|}{\nu} \quad (\text{eq. 16})$$

The characteristic velocity and characteristic length of the larger eddies are of the same order of magnitude as the velocity scale and length scale of the mean flow. Therefore a large eddy Reynolds number is dominated by inertia effects and viscous effects are negligible. The stretching work done by the mean flow on the large eddies during these events provides the energy which maintains the turbulence. Smaller eddies are stretched strongly by the larger eddies, such that the kinetic energy is handed down in what is referred to as an energy cascade [53].

Wind flow is turbulent as a result of the passage over a rough surface or buoyancy. Turbulent flow is a 3-D flow and it is common to define the x-axis along the direction of the mean wind [34, 15].

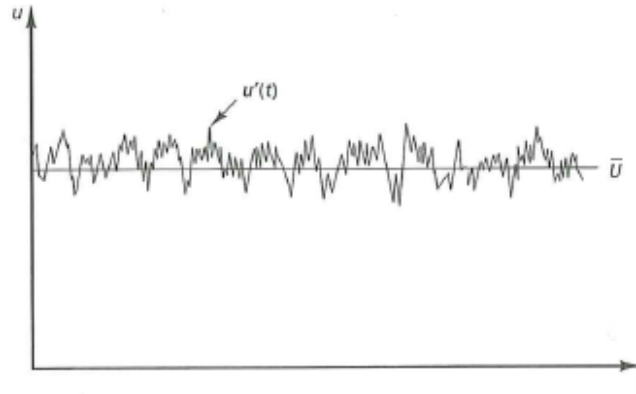


Figure 10: A typical point velocity measurement in turbulent flow [53].

Because of the random nature of turbulent flows, it is advantageous to decompose the motion into a steady mean value with fluctuation component $u'(t)$ (see Figure 10). When superimposing the fluctuating component on the mean flow we get a useful expression of the instantaneous wind at a given time: $u(t) = \bar{U} + u'(t)$. This is called the Reynolds decomposition. The turbulent flow can now be characterized in terms of the mean values and some statistical properties [53].

The kinetic energy of large-scale atmospheric circulation produces motions generally described as turbulent eddies [36]. Visualisation of turbulent flows reveals these eddies, which have a rotational flow structure with different length scale (see next chapter). This eddying motion brings, due to effective mixing, initially separated particles closely together as heat; mass and momentum are effectively exchanged. The largest turbulent eddies interact with and extract energy from the mean flow by a process called vortex stretching [58].

2.7.1 TURBULENCE LENGTH SCALES

In order to quantify turbulence one uses several length scales represented by vortices of different spatial dimensions. They can be categorised into the largest eddies, diffusive action and the smallest eddies. The largest eddies are anisotropic and the smallest eddies are isotropic (non-directional) [53]. As a result of the mixing, energy is transferred to higher wave numbers [54, 24]. For large Reynolds numbers, there are a range of high wave numbers where turbulence is determined by the TKE dissipation rate (eq. 18) and the kinematic viscosity only, according to Kolmogorov's first hypothesis. This range is usually referred to as the viscous sub-range and is statistically independent of the large scales. The smallest scales present (i.e., Kolmogorov microscales) can be expressed in terms of the rate of energy dissipation and the fluid viscosity. In order to obtain ratios for length, time and velocity one uses dimensional analysis [54].

There are other length scales, such as the integral length scale and Taylor length scale, which is a measure of large scale eddies in the production range and the size of these eddies in the inertial sub-range respectively. The former is achieved by integrating a spatial auto-correlation. The latter is obtained by a series expansion of the auto-correlation coefficient. From this has been deduced an estimate of the dissipation rate, which is used in determining the resolution and simulation times needed [54].

2.7.2 TURBULENT KINETIC ENERGY

Different fields of research uses different turbulent properties. In meteorology the fluctuations are described by the variance and root mean square (RMS). The mean kinetic energy per unit mass contained in the velocity fluctuations are one-half times these variances, based on the definition of kinetic energy. Hence one defines the TKE at a given location as follows [53, 60].

$$k = \frac{1}{2} (\overline{u'^2} + \overline{v'^2} + \overline{w'^2})$$

(eq. 17)

The smallest eddies work against viscous stresses causing dissipation of TKE. The rate of such per unit volume is given in the following way [54].

$$\varepsilon = \frac{\mu}{\rho} * \frac{\partial u'_i}{\partial x_k} * \frac{\partial u'_j}{\partial x_k} \tag{eq. 18}$$

2.7.3 TURBULENCE INTENSITY

In engineering science the turbulence intensity, I , is used. According to IEC 61400-1 it is “the ratio of the wind speed standard deviation to the mean wind speed, determined from the same set of measured data samples of wind speed, and taken over a specified period of time”.

Assuming a homogeneous terrain, (i.e., homogeneous turbulence) in the horizontal plane the statistical characteristics of turbulence varies with height only. Turbulence intensity reduces gradually with height [61]. The turbulence intensity is the average RMS velocity divided by a reference mean flow and is linked to the TKE in the following way [53].

$$I = \frac{\left(\frac{2}{3}k\right)^{1/2}}{U_{ref}} = \frac{\sigma}{U_{ref}} \tag{eq. 19}$$

Where σ in IEC 61400-3 is defined as the “standard deviation of the longitudinal component of the turbulent wind velocity at hub height”. It is an important design parameter and it follows from the equation above that it is used to calculate the turbulence intensity [12].

2.7.4 AVERAGING

A measurement of flow variables at a single point is. The values of TKE and wind speed found at a given time and point in space are instantaneous values derived by the use of a turbulence closure model. When using turbulence closure models, such as the RANS k- ε model, the turbulence itself is not resolved on a fine scale (see next chapter). This may mean an inaccurate picture of the case. The studied case is a transient case and relies on a moving wave surface, hence instantaneous values and profiles will not give the right picture. The different time steps are independent statistical events. Based on this we can define the arithmetic average as the sum of the values divided by the number of time steps [58]. However the real fluctuating wind speed, RMS, should be calculated as;

$$U' = \sqrt{U^2_{mean} + \frac{2}{3}K_{mean}} \tag{eq. 20}$$

where the former is due to large scale fluctuations and the latter is small scale (eq. 17). This is due to the sum of two uncorrelated fluctuating functions [62].

2.8 TURBULENCE MODELS

Quantitative predictions of turbulent flow systems usually rely on computational procedures, called turbulence models. Turbulence models are categorized with respect to the range of the resolved turbulence. The NS equation is ground zero for CFD simulations of the ABL and contains nonlinear terms for convection and pressure gradient which need to be solved numerically using appropriate techniques. In order to solve the NS-equations, and obtain turbulent closure, one uses Reynolds decomposition and time averages the equation. The new fluctuating terms called Reynolds stresses, $\tau_{ij} = -\rho \overline{u'_i u'_j}$, gives more equations than unknown, and

unfortunately we are unable to produce a set of reasonably solvable universal equations. Momentum equation in all three directions denotes a stress tensor which, due to symmetry, consists of 6 new unknowns. In order to solve these one relates the Reynolds stresses to the time averaged velocities [54]. Turbulence models are predicting Reynolds stresses in order to solve the RANS-equations (eq. 10) and (eq. 11). They allow the calculation of the mean flow without calculating the full time-dependent flow field [9, 24].

Covering a wide range of flow conditions and producing reasonably accurate results in the simplest way possible is the goal for turbulence models. Given the importance of turbulence in engineering applications, a substantial amount of research effort is dedicated to the development of these classical numerical methods. Computational cost and accuracy increases down the list [24, 53, 63].

1. Models based on Reynolds averaged Navier-Stokes (RANS) equations:

- Zero-equation models: mixing length model
- One-equation models: Spalart-Allmaras, k-L models, etc.
- Two-equation models: k-ε models, k-ω models, algebraic stress models (ASM), etc.
- Seven equation models: Reynolds stress models (RSM)

3. Hybrid models, i.e., models combining LES models for free-stream regions and RANS-based models in near-wall regions.

- Detached eddy simulations (DES) [24].

2. Models based on space-filtered equations:

- Large eddy simulations (LES) models.

4. Direct Numerical simulations (DNS) [53].

2.8.1 K-ε MODEL

The k-ε model is a well-established, popular and the most widespread RANS turbulence model. Boussinesq relationship, stating that Reynolds stresses are proportional to the mean rate of deformation, is utilized. The name two-equation model origins from the two extra transport terms for k and ε and (see Appendix B). From the NS-equations one may derive differential transport equations for these properties [9, 24, 53, 54].

The following (simplified) transport equation for the TKE is commonly used [24].

(eq. 21)

$$\underbrace{\frac{\partial(\rho k)}{\partial t}}_{\text{Rate of increase}} + \underbrace{\frac{\partial(\rho k U_j)}{\partial x_j}}_{\text{Convective transport}} = \underbrace{\frac{\partial}{\partial x_j} \left(\left(\mu + \frac{\mu_t}{\sigma_k} \right) \frac{\partial k}{\partial x_j} \right)}_{\text{Diffusive transport}} + \underbrace{\rho P_k}_{\text{Rate of production}} - \underbrace{\rho \epsilon}_{\text{Rate of dissipation}}$$

The Prandtl number σ_k connects the diffusivity of the TKE (i.e., turbulent transport coefficient) to the turbulent viscosity $\sigma_k = \mu_t / \Gamma_\varphi$ [24, 64].

The transport equation for dissipation of TKE reads.

(eq. 22)

$$\underbrace{\frac{\partial(\rho \epsilon)}{\partial t}}_{\text{Rate of increase}} + \underbrace{\frac{\partial(\rho \epsilon U_j)}{\partial x_j}}_{\text{Convective transport}} = \underbrace{\frac{\partial}{\partial x_j} \left(\left(\mu + \frac{\mu_t}{\sigma_\epsilon} \right) \frac{\partial \epsilon}{\partial x_j} \right)}_{\text{Diffusive transport}} + \underbrace{C_{\epsilon 1} \rho \frac{\epsilon}{k} P_k}_{\text{Rate of production}} - \underbrace{C_{\epsilon 2} \rho \frac{\epsilon^2}{k}}_{\text{Rate of destruction}}$$

P_k is the rate of production of k. For standard k-ε model the five adjustable constants are as follows [9, 24].

(eq. 23)

$$\sigma_k = 1.0, \sigma_\varepsilon = 1.3, C_{\varepsilon 1} = 1.44, C_{\varepsilon 2} = 1.92 \text{ and } C_\mu = 0.09$$

From Prandtl's mixing length theory and dimensional analysis we can calculate turbulent eddy viscosity, μ_t , represented by the nut-field;

(eq. 24)

$$\mu_t = \rho C_\mu \frac{k^2}{\varepsilon}$$

where C_μ is a dimensionless constant. It models the effects of the turbulence on the mean flow. The effective viscosity is the sum of the turbulent viscosity and the laminar viscosity ($\mu_{\text{eff}} = \mu_t + \mu_{\text{lam}}$) [54]. Since no flow specific parameters are required, such as distances to walls, the model is the simplest complete turbulence model leading to stable calculations (i.e., good convergence). [9, 24].

The model is known to perform well for many industrial flows. The common use of the model has highlighted shortcomings, such as the need for modelling of all parts, in the ε -equation. Flows, driven by thermal effects, containing large adverse pressure gradients, strong separation, swirling and rotating are some of the cases where the standard k- ε model does not perform particularly well [24].

2.8.2 LARGE-EDDY SIMULATIONS

The increased level of detail is the main advantage of the LES model. Where the previous method provides averaged results, LES gives predictions of flow characteristics and resolve turbulent flow structures. Hence a greater accuracy for flows involving flow separation or acoustic prediction is achieved [24, 53].

There is a difference in behaviour of the large and the small eddies for turbulent flows. The crux is that the larger eddies need to be computed for each problem with a time-dependent simulation. LES uses a spatial filtering to separate the larger and smaller eddies instead of time-averaging. This operation is performed on the time-dependent flow-equations [53].

Filtering of continuity equation (eq. 10) yields the LES continuity equation;

(eq. 25)

$$\frac{\partial \rho}{\partial t} + \nabla(\rho \bar{u}) = 0$$

where the over-bar as an exception indicates a filtered flow variable [53]. A disadvantage of the model is that the filter is applied to the NS-equation results in an extra viscosity term, and the model may be relatively user dependent, demanding a prior knowledge of the flow field [24].

2.9 OPENFOAM

FOAM is short for Field Operation and Manipulation and is a library of functions written in C++. It is used to create applications for solving continuum mechanics problems. OpenFOAM is mostly driven by text files and unix style commands, and is run under the Linux operating system. An alternative, used in this thesis, is to run OpenFOAM under Windows with use of Oracle VM virtual box, emulating a Linux computer. The main workflow in OpenFOAM consists of selecting a solver for the problem, creating a mesh, modifying input text files, solving the case and post-processing the results. Cells of any shape are available for mesh generation which gives a great flexibility [57].

2.9.1 OPENFOAM CASE STRUCTURE

Each new case must consist of the directories `0`, `constant` and `system`. In `constant` the mesh, material properties, and turbulence properties can be found. Number of iterations, time step, size and solution controls are found in `system`. Initial flow fields and boundary conditions can be found in `0`. The case structure is shown in the figure below [57].

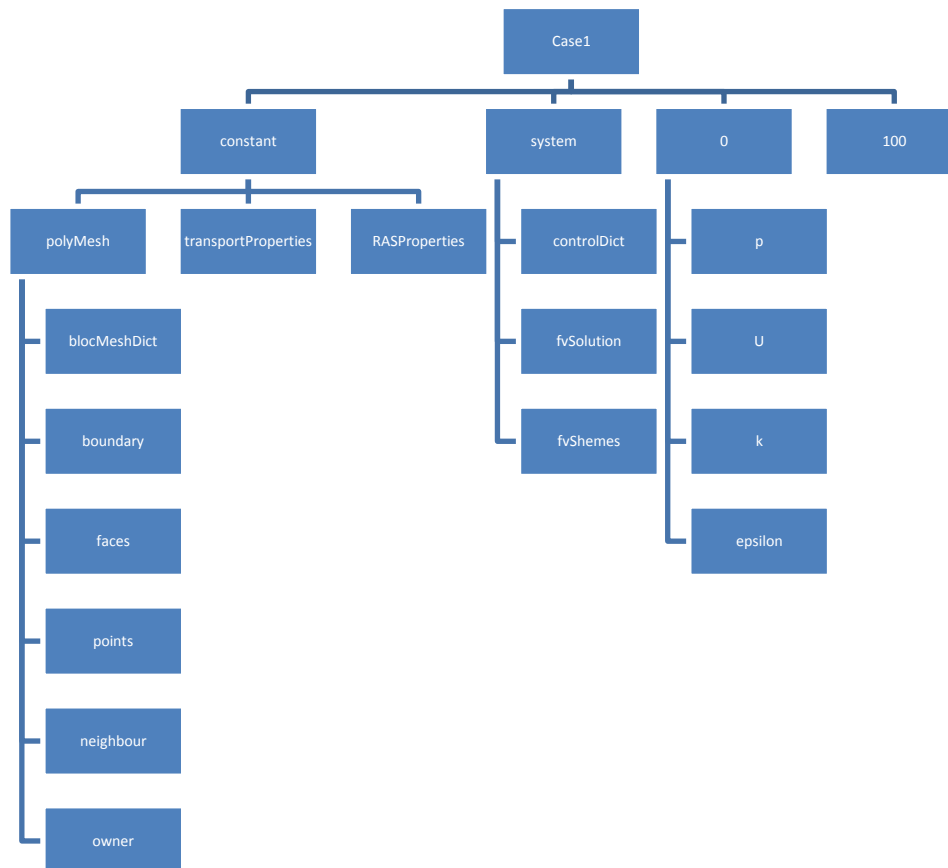


Figure 11: Case structure [57, 65].

2.9.2 FIELDS

All fields (i.e., parameters) are initialized in the `0` directory. The different boundary conditions are given for `p`, `U`, `k`, `epsilon` and `nut`. Getting the boundary conditions right is the main task for the modeler. In this specific case for this wave-wind interaction study a field called `pointDisplacement` is specially developed and added in order to define the wave state (see 3.1.3 Physical properties).

As the computation proceeds, new time dumps are written in addition to `0`. Fields are created under each time dump and include values and boundary conditions for each cell of the mesh. The dimensions in the field files must be consistent with the formulas used under calculation. Dimensions are shown in the following way in the field files [`kg m s K mol A cd`] and numbers are used to indicate the right dimension (e.g., `m/s` is defined as `[0 1 -1 0 0 0 0]`).

2.9.3 DICTIONARIES

Under the directories `system` and `constant`, dictionaries can be found. They consist of controls, material properties, etc. dependent on the solver used. In dictionaries whose names are given the suffix `...properties`, the physical properties of the case are stored. `controlDict` and `transportProperties` are examples of dictionaries [57].

In the dictionary `controlDict`, one can define start time, end time, time step, write interval, functions etc. There are twelve types of functions. After the key word `outputControl` one can choose to write `timeStep` or `outputTime`. The `timeStep` writes the probe data every time step, while the `outputTime` writes the probe data every time a time dump is written. One should use `timeStep 1` for steady state cases, while for transient cases one makes use of the Courant number (eq. 26). In the dictionary `fvSolution` one finds solvers to invert the matrix (eq. 15) and the type of pressure-velocity coupling used [57].

2.9.4 MESH

The information about the computed mesh is found in `polyMesh`. Here `points`, `faces`, `cells`, `patch`, `boundary`, `neighbour`, `owner` and sometimes `cellZones`, `faceZones` and `pointZones` are found. `points` are defined as locations in space, `faces` as lists of points, and `cells` as lists of faces. `patch` is faces that form the boundary of the mesh, `boundary` is a list of patches, `neighbour` is a list of neighbor cell labels and `owner` is a list of owner cell labels [57].

There are three possibilities for generation of the mesh. `blockMesh` can be used to generate a relatively simple mesh consisting of several `blocks`. The `blocks` entry is a list of eight vertices (i.e., `points` that define the geometry) to make a block. Each block specifies the number of cell in each radial direction. The `snappyHexMesh` utility uses hexahedra and split-hexahedra to automatically generate 3-D meshes [63]. It is also possible to convert a mesh to OpenFOAM specific mesh by the use of different available applications in the OpenFOAM toolbox. The mesh should always be checked using the command '`checkMesh`' [57]. Further details on meshing will not be given in this thesis seeing as it is not relevant when using an established case.

2.9.5 BOUNDARY CONDITIONS

In order to solve a CFD problem, boundary and initial conditions are essential. There are two types of boundary conditions; the "Dirichlet" describes the dependent value by a value on a patch, `fixedValue`. "Neumann", on the other hand, specifies a gradient at the boundary patches. `fixedGradient`. Only the former and a derivation from it, `movingWallVelocity`, are used in this project (see Ch. 3.1.2 Boundary and initial conditions) [63].

The conditions close to a wall are assumed to be described by "the universal velocity-profile". Yielding a laminar region closest to the wall, viscous sub-layer, with a linear relationship between two dimensionless parameters, velocity u^+ and distance from the wall y^+ . Further away from the wall the flow is turbulent and there is a log-law relationship, hence it often being referred to as the log law layer ($30 < y^+ < 500$). In order to calculate the boundary layer it is recommended to have average $y^+ < 1$ and $30 < y^+ < 300$ to model the boundary layer [53, 54].

2.9.6 SOLVER

Within the OpenFoam tool box there are almost 100 different solvers for calculations of various flows, stress methods and other disciplines [63]. Solving a case is done by typing the application name as a command. This has to be performed from the case directory. Solvers are either steady state or transient. Pressure-velocity couplings are different in steady state and transient solvers. The discretisation is "state-of-the-art" in CFD and usually not considered by the user seeing as there are almost countless options (see Ch.

2.6.2 Discretisation) [53, 57].

Even though there are no equations for pressure, the pressure links the momentum balance in the three directions (eq. 11) and is solved from the continuity equation (eq. 10) by the use PIMPLE. PIMPLE has merged the two algorithms Semi-Implicit Method for Pressure Linked Equations (SIMPLE) and Pressure Implicit with Splitting of Operators (PISO). The derivation makes use of the relatively straightforward SIMPLE algorithm, which is a way of solving the NS-equations (see Appendix C).

2.9.7 POST-PROCESSING

OpenFOAM does not plot the residuals automatically hence any output must be saved to a file by use of the command `'application | tee <filename>'`. Afterwards convergence can be checked with the command `foamLog <filename>`. This creates the directory `logs` where text files for residuals can be found and plotted graphically. The command `'paraFoam'` opens ParaView where graphical post-processing operations can be performed. For detailed explanation of the built-in post-processing utilities, please refer to [63].

For transient cases one expects accurate results for each time step, while for steady state one single relevant solution is present. An important factor in the output of transient cases is the Courant number defined as;

$$Co = \frac{\delta t * |U|}{\delta x} \quad (\text{eq. 26})$$

where δt is the time step, $|U|$ is the magnitude of the velocity through that cell and δx represent the size of the smallest cell. Thus the Courant number is the fraction of flow during a time step which passes through a cell. This is an important factor in transient simulations and is found as an output for every time step. For complex cases, as this one, it is beneficial to use `adjustTimeStep`, as it will be automatically adjusted to fit the `maxCo` defined [63]. The residuals mean and max Courant number indicates whether the time step is small enough for a decent time discretization. However a too small Courant number yields computation time lost. Max courant number gives more stable solution if it is < 1 . The residuals for U in x, y and z-direction should also be $\ll 1$. For pressure the residual appears twice for PIMPLE, due to the two loops for solving pressure. If the courant number is large, more than two loops are required. To ensure a converged solution when using PIMPLE, the continuity error of the last loop must stay small, max and mean Courant number cannot become large and the initial residuals of the last outer loop should be relatively small [57].

3 METHODOLOGY

In this part of the thesis methods of work are described. The theory used as basis has been written in chapter 2 Theory, and the results will be presented and discussed in chapter 4 Results and discussion. This project is composed of sensitivity studies on two main elements; different inlet wind conditions (case 1) and wave states (case 2) and comparisons with Sullivan et al. (2008) [6] (case 3). The following is a detailed description of my work and a description of the set ups (see Appendix D). In chapter 3.1 the setup for the “standard-case” are described. Chapter 3.2 gives a brief overview of the solver and code used for the simulations. Chapter 3.3 concerns the grid independence study and chapter 3.4 explains the setup of case 3. Finally, chapter 3.5 explains how the post-processing has been done.

The first weeks of the project work were more or less only dedicated to research and study of literature. Numerical simulations of wave-wind interactions are apparently a quite immature field of research, and relevant available literature is scarce. Some journals etc. were handed over by Kalvig, some were found on an “its-learning” group called “Vindturbin-modellering” formed by Obhrai, Eliassen and Kalvig amongst others at UiS. Some literature was discovered using various search engines such as Scencedirect, Scopus, Google Scholar and regular Google searches. A few books on wind and waves were borrowed from the library at UiS. Last but not least, relevant master theses were found on <http://brage.bibsys.no/UiS/>. For CFD purposes, <http://www.cfd-online.com/> has been thoroughly used when looking for guidance on preparing the cases. A practical guide in writing, by Jacobsen (2008) [66], have been beneficial in the design and writing process of this thesis.

3.1 PRE-PROCESSING

3.1.1 MESH GENERATION

In order to obtain correct results accurate grids are vital. Grid generation may be the most important pre-processing step because the accuracy of the CFD solution depends on it. The starting point for the “standard-case” in this project is the case “wFD_a3”, short for waveFadeDisplacement_aligned3, provided by Kalvig. The “standard-case” is used and referred to unless other comments are made.

Since the model makes use of a dynamic mesh, the mesh created at the beginning is updated at each time step with `blockMesh`. The initial domain was, in Cartesian coordinates, (250 25 50) discretised using (200 20 40) grid points. In order to save calculation time the number of cells in y-direction was sat to 1 yielding a 2-D simulation with 8.000 cells (see Figure 12). A reasonable simplification is to think that the wave does not vary in the y-direction and hence we can see this as a 2-D problem [44]. For k-ε this assumption of a 2-D simplification holds because the TKE is the sum of the three velocity vectors and thus we can have a 2-D case even though turbulent flows are 3-D [53]. To start with the height of the domain was increased to 150 m to include the entire height of an offshore wind turbine. However this did not produce any interesting results, even with a wind speed of 40 m/s, hence the original height was kept as a basis for the sensitivity simulations.

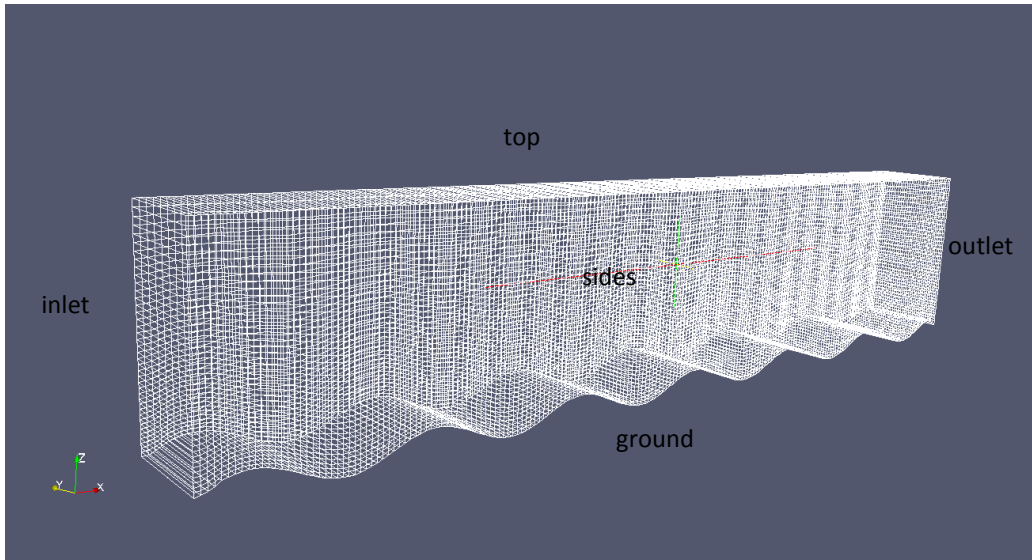


Figure 12: Domain and mesh.

3.1.2 BOUNDARY AND INITIAL CONDITIONS

After completing the mesh generation, initial fields set up were studied. A common simplification is to set the initial fields to be uniform, as in this case. As we are dealing with an incompressible case only the relevant pressure development is of interest, so it is set to uniform and zero for convenience (see Appendix E).

In the velocity field (see Appendix F), the `internalField` is uniform and is set to the same fixed value as the uniform wind speed at the inlet, due to divergence problems at high wind speeds. For the “standard-case” a wind speed of 10 m/s is used (see Figure 8). On the ground patch the boundary condition used initially was fixed zero. It does not take account for the moving particles on the surface of the wave and the effect may at first be seen in cell number two. Seeing as a no-slip condition is not possible to implement on a moving surface, `movingWallVelocity` which defines the same speed as the vertical velocity of the moving cell, is used (except for the grid independence study). This boundary condition takes account for the particle movement in the wave as it becomes a vector (see Appendix D.2). Finding the correct way to implement this boundary condition was rather comprehensive. Eventually it was done by stopping the simulation after 10 s, changing the boundary condition at this time step for all the processors and restarting the simulation which will then read from the latest time step.

Using a logarithmic wind profile at the inlet was considered at an early stage but cyclic boundary condition was preferred. It is a periodic boundary condition treating two boundary regions as if they are physically connected. It was defined in the `boundary` file for inlet and outlet and in all the initialization files, but because of limitations in the code to handle this boundary condition on a moving mesh it was unsuccessful and a uniform inlet was used. `inletOutlet` condition is used at the outlet, to prevent mass re-entry from the outlet. The last patches are `top` and `frontAndBack` where a slip condition is assumed (see Appendix F) [63].

Rough approximations for the TKE inlet distributions can be calculated from the following equations [67].

$$k = \frac{3}{2} (I * U)^2 \quad (\text{eq. 27})$$

The inlet turbulent intensity is assumed to be 5 % [67]. The dissipation rate value in the `epsilon` file is calculated by;

$$(\text{eq. 28})$$

$$\varepsilon = \frac{C_{\mu}^{0.75} * k^{1.5}}{l}$$

where l is the turbulence length scale assumed to be 7 % of the inlet height (i.e., equivalent pipe diameter) [53, 54].

Different initial values for initiation of TKE and the dissipation rate have been tried earlier because the code is sensitive to changes of these parameters. The current values calculated are $k = 0.5 \text{ m}^2/\text{s}^2$ (eq. 27) and $\varepsilon = 0.015 \text{ m}^2/\text{s}^3$ (eq. 28) for all the cases based on the “standard-case” (see Appendix G and Appendix H). In the `nut` file surface roughness is defined $0.01 \text{ m}^2/\text{s}$, considered being sufficiently low (see Appendix I). Although the surface roughness should increase with increasing wind speed (eq. 7), it may be assumed that the ocean surface waves provide the effective roughness hence the “wall roughness” is kept constant for all simulations [68].

3.1.3 PHYSICAL PROPERTIES

In `transportProperties` a Newtonian transport model were chosen, because air is a Newtonian fluid, and kinematic viscosity was defined to be $1.5 \times 10^{-5} \text{ m}^2/\text{s}^2$. Using characteristic velocity and height of the domain 10 m/s and 50 m respectively, this implies a Reynolds number of $\text{Re} = 3,33 \times 10^7$, which is a high Reynolds number on which k- ε model is mainly applicable [54, 56]. The k- ε model and its coefficient (eq. 23) were selected in `RASProperties`.

In order to implement a moving wave surface Kalvig. in co-operation with Manger, ordered a modification in the code from OpenCFD and thereafter some modifications in this new code was needed in particular the development of fading wave ends. When implementing the faded wave ends, Manger used the boundary type `waveDisplacement` available in the git repository for OpenFOAM2.1x. He developed the user defined `waveFadeDisplacement` by adjusting the wave at the ends of the domain so the wave gradually develops/disappears (ensuring stability). In `pointDisplacement` the setup of the wave state has been defined (see Appendix J). The parameters describing the wave state in this context are amplitude, wave speed, and wavelength, referring to wave properties defined in Ch. 2.3.1 Wind sea. When choosing these values it was done according to the theoretical steepest wave ($a/L = 3/40 \approx 1/14$) as the intention was to see an impact on the flow field. For clarification the wavelength in `pointDisplacement` is from wave trough to crest therefore the real wavelength is two times the wavelength defined there. With wavelength of 40 m the wave speed was chosen to be 8 m/s, according to linear dispersion relation (eq. 4).

3.2 SOLVING

In this thesis a transient solver for incompressible flow of Newtonian fluids on a moving mesh using the iterative PIMPLE algorithm called `pimpleDyMFoam` is used (see 2.9.6 Solver) [63].

3.2.1 CODE FORMULATION

Multi-grid methods use a coarse grid with fast solution times to smoothen out high frequency errors¹⁵ and to generate starting solutions for the finer grid [69]. In this case a linear solver with smoothing called Geometric Agglomerated algebraic MultGrid (GAMG) is defined to solve the inverted matrix (eq. 15). A tolerance is given, indicating how accurately the equation is solved. If the initial residual is smaller than this value, the equation is not solved anymore. The relative tolerance identified with `relTol` defines how accurate the equation is solved inside a loop. If a case diverges early it often helps to set this value to a small value. In this case the value is set to zero to force the solution to converge to the solver tolerance. If a case diverges early it often helps to set this value to a small value. Relaxation factors are tuning tools to make a steady state solution converge, set to 1.0 (see Appendix K) [57, 55].

¹⁵ The error field frequency is the gradient of error from node to node [77].

Discretisation schemes are defined in `fvSchemes` (see Appendix L) starting with the time derivative scheme used for the $\partial/\partial t$ -term. In this project we are only dealing with transient cases and hence a genuine transient scheme called Euler is set as default. It is a first order bounded and implicit scheme¹⁶. Further on in the text file, the scheme is used to calculate gradients at cell centres. `grad(p)` is always recommended to be discretised with `Gauss linear` and generally for good meshes. `Gauss` indicates the use of the discretisation method “Gauss theorem” afterwards `linear` (i.e., central differencing) should be selected [57]. In this case default `Gauss linear` and `Gauss linear` for `grad(p)` and `grad(u)` are used. The `snGradSchemes` defines whether or not the solver uses non-orthogonal correction. Interpolation schemes are used to interpolate variables at the cell faces. In `fluxRequired` the variables for which the flux is computed are listed. In this case and the majority of other cases, only pressure is listed since the flux is computed after the pressure equation is solved.

3.2.2 RUNNING THE CODE

Two scripts are defined in order to facilitate the start-up of the different simulations `Allclean` and `Allrun` (see Appendix O).

In `decomposeParDict` the decomposing of the processors are defined. The utility `decomposePar` partitions the domain into separate domains for each processor. It has the ability to cut the domain in all three directions and it was found that cutting the domain with planes normal to the flow direction contributed to a decrease in simulation time. The 4 subdomains were placed in the following way (2 1 2). When finished it was reconstructed using `reconstructPar`.

3.2.3 MONITORING

When experimenting with new cases it is essential to monitor the jobs. In this way one can tell what is going right and wrong. For each simulated parameter, a report line is written with the solver name, the variable that is solved, its initial and final residuals and number of iterations. This was followed by the use of `tail -f log.pimpleDyMFoam`. In order to monitor the jobs in ParaView as they were running, `reconstructPar -latestTime` were executed.

3.2.4 CONTROL

An advantage of OpenFOAM is the great flexibility it offers with respect to time control. When the original setup was run for the first time, the disk space on the virtual machine was filled up. A compromise was done after considering what information needed. The `writeInterval` was changed to 0.5 and `purgeWrite` to 50 in the `controlDict` (see Appendix M). The value of the integer in `purgeWrite` represents the number of time directories stored [63]. However a virtual machine with much greater disk space was installed at a later stage. Due to problems with divergence initially, as a result of small time steps, `maxCo` were halved to 0.5. In most textbooks the initial value of 1.0 is preferred, yielding the solution progresses more slowly and stable in this case (eq. 26).

In transient simulations a kind of stationary state is reached when the result approaches what is called a “semi steady state”. In order to obtain this, the fluid should pass through the domain 10 times for a laminar case [10, 63]. The fact that this is a turbulent case does not make any difference and the end time should probably be 250 s according to this rule [62]. However, simulations showed that the influence of the change in end time on the wind speed and TKE profiles were down to the fourth decimal (see Appendix P). Hence it was decided to stick with end time 100 s, which makes the fluid pass through the domain approximately four times for the “standard-case”.

¹⁶ An implicit scheme is when a physical property only at the new time level is used [53].

3.3 GRID INDEPENDENCE STUDY

All credible and reliable CFD-simulations must document a grid independent solution. This is obtained when a solution is approximately equal regardless of an increasing grid resolution. The way of doing this is to increase your number of cells and compare the profiles and curves of the relevant parameters. In such a case one can continue working with the smallest number of cells. A good approach is to double the number of cells for each simulation [62]. In a 2-D case this implies an increasing in number of cells by the factor square root of two. Nevertheless in this case the increase of cells in x and z-direction was increased/decreased only by approximately 25 % each time because it was aimed at obtaining a grid independent solution with the smallest cell number possible. To determine if the solution is independent of the grid size, solutions from 4.500, 12.500 and 18.000 cells was compared against the solutions from the 8.000 cell simulation. The results are from time step 100.

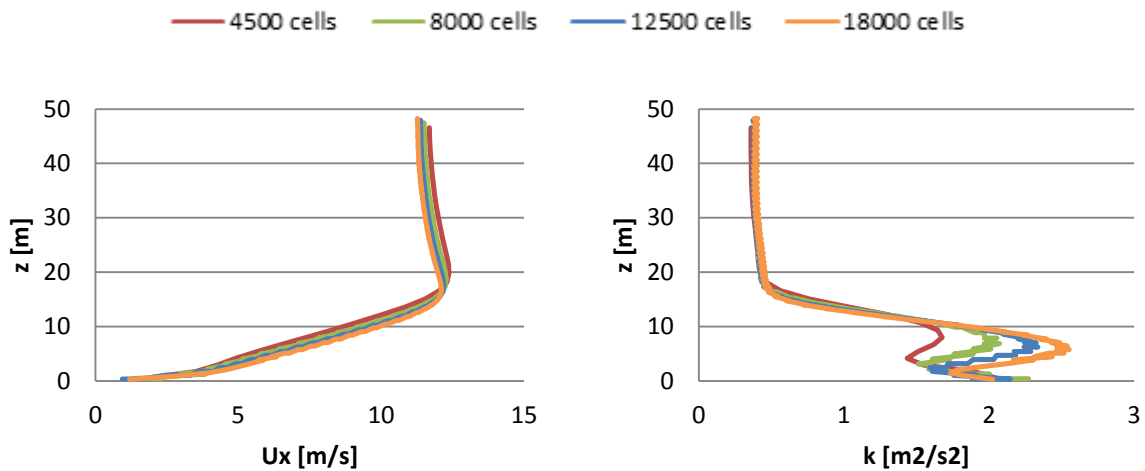


Figure 13: Grid independence study, vertical profile of horizontal wind speed¹⁷ and TKE at $x = 125$ m.

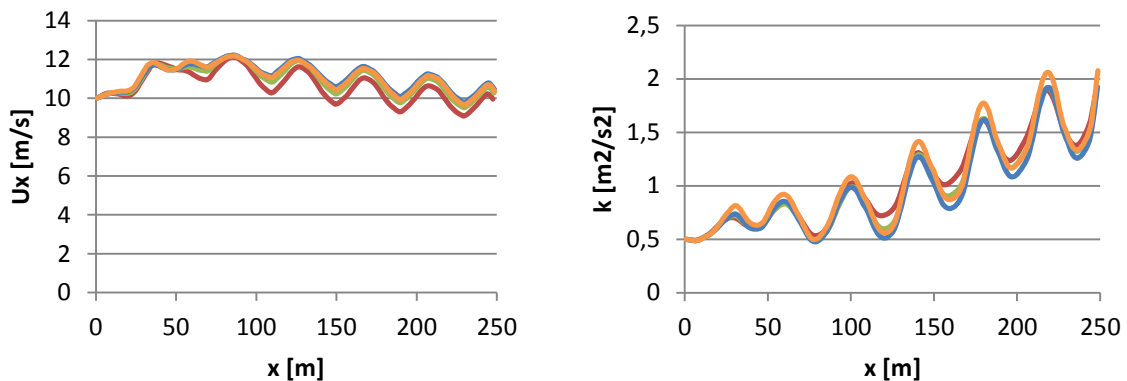


Figure 14: Grid independence study, horizontal profile of horizontal wind speed and TKE at $z = 15$ m.

As shown in Figure 13 and Figure 14, grid independent solutions were obtained for wind speed and TKE calculations. In general the vertical profiles show great compliance, although there is some discrepancy for TKE in the in the lowest 10 m of the domain. It is common that it is harder to obtain a grid independent solution for TKE, because it is dependent on the gradient of the wind speed. Small changes in wind speed yield great impact

¹⁷ Hereafter the notation U_x , U_y and U_z is used for wind speed in x, y and z-direction as in OpenFOAM.

on the TKE, hence the TKE demanding a better resolution. The horizontal profiles show a clearer pattern that highest cell number implies highest values for horizontal wind speed and the greatest amplitude for TKE. In addition TKE indicates that the flow is not fully developed, a continuous increasing value implies that the domain size could have been larger in the x-direction. Seeing as the reported results indicates a satisfactory good match for the two simulations with the highest number of cells it was stated that a grid independent solution was obtained for 12500 cells which implies a grid resolution of $(\Delta x, \Delta z) = (1, 1)$ (see Appendix N).

3.4 SULLIVAN ET AL. (2008) SETUP

The idea behind copying the setup of Sullivan et al. (2008) [6] (hereafter named Sullivan's) was to test the experience gained so far "up scaling" in order to simulate swell conditions. If the results of the computational demanding LES experiment will be visible with this k- ϵ model it would be an interesting discovery. Then a flexible and computational cost efficient case will be available for further experiments.

The computational 2-D domain (1200 1 100) m used is equal to the 3-D LES experiments is in the x-direction but only 100 m in z-direction compared to Sullivan's 800 m. The reduction in z-direction is due to limitations in computational force as running the case on a powerful cluster failed. Nevertheless only the lowest 100 m is examined and the case. It was discretised with one the same grid resolution used for the "standard-case" hence grid independence is believed to still apply. Making use of the same methodology as for the "standard-case" the boundary conditions are; $k = 0.1 \text{ m}^2/\text{s}^2$ and $\epsilon = 0.07 \text{ m}^2/\text{s}^3$, and end time is 1000 s.

The imposed wave has an amplitude $a = 1.6 \text{ m}$, wavelength $L = 100\text{m}$, and based on linear dispersion (eq. 4) the wave speed $c = 12.5 \text{ m/s}$. The surface roughness was $z_0 = 2 \cdot 10^{-4} \text{ m}^2/\text{s}$ and the geostrophic wind $U_g = 5\text{m/s}$ at inlet and at top. The reason for also defining a velocity at the top was in order to compensate for the reduced height of the domain. Sullivan's makes use of $z_i = 400 \text{ m}$ which is the nominal thickness of the boundary layer (i.e., initial depth of the PBL) and ζ as z-coordinate being a wave-following coordinate. However z is approximately equal to ζ and hence only z will be used for comparisons.

3.5 POST-PROCESSING

When post-processing on profiles the "plot over line" filter in ParaView has been used. Because the results from the grid independence study (see Figure 14) shows increasing TKE downstream the vertical profiles are taken at $x = 210 \text{ m}$ (see Appendix D.4) and horizontal profiles at $z = 15 \text{ m}$. All the relevant files were copied from the virtual machine with the file transfer software WinSCP. Post-processing on the velocity and TKE profiles was done in Microsoft Excel.

3.5.1 FIELDAVERAGE

As mentioned in Ch. 2.7.4 Averaging there is a need for averaging the instantaneous values. The utility `fieldAverage` is time averaging (mean) of each field for each time step and writes the results in the time directories [63]. The script for calculating `mean` and `prime2Mean` for wind speed and TKE is defined in the `controlDict` file. `prime2Mean` shows the difference between the instantaneous and averaged values in the fluctuation for wind speed ($U^2\text{Mean}$) and TKE (eq. 20). It is pivotal to average for a sufficiently long period of time. The averaging process was, due to computational limits, done by simulating with `fieldAverage` for approximately five periods after the actual end time. This was done by at first commenting out `fieldAverage` by typing `/*...*/` and removing it afterwards [57].

Due to uncertainty and lack of information on the utility used for calculating the mean values diligent effort has been made to understand this properly. The uncertainty was about its ability to handle the moving mesh. If the vertical movement of the cells are not taken into account the effect of wave movement would not be seen. A validity test was carried out by manually comparing it to instantaneous velocity profiles over one wave length in time and several locations downstream (see Ch. 4.1 Validity test of `fieldAverage`). As the flow in the

model is dependent on the x-direction, averaging in space should only be carried out when semi-stationary conditions apply. It is worth mentioning that all values below the wave crest should be neglected as values there are not always present.

3.5.2 y^+

For this turbulent computation it is fundamental to check critical values like y^+ (`yPlus`). `yplusRAS` is calculating and reporting y^+ for all wall patches, for the specified times [63]. When the values on the bottom of the internal mesh are as shown in Figure 15 they are slightly too high (see Ch. 2.9.5 Boundary conditions). It is however stated that the boundary layer and the physics on the ground is modelled satisfactory accurate as average y^+ values in the region of interest are acceptable.

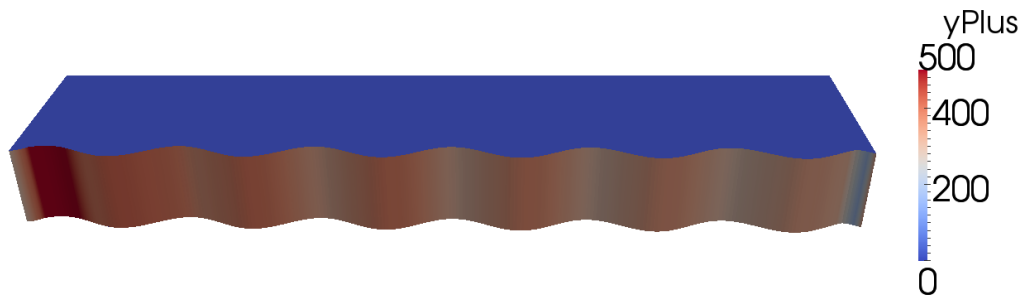


Figure 15: y^+ on the bottom of the internal mesh.

In order to obtain satisfactory y^+ values, the utility `simpleGrading` were used [63]. Uniform expansion (1 1 5) in the three directions were defined in the `blockMeshDict` implying a refining of the mesh in the z-direction (see Appendix Q). It reduced y^+ values to about one-third of the initial values with uniform expansion (1 1 2). Further grading was tested, but the results diverged for higher wind speeds.

3.5.3 RESIDUALS

After the “standard-case” were run, convergence (e.g., residuals, number of iterations, Courant number etc.) written to a logfile were checked. Instead of the common command creating the `logs` directory, `'foamLog log.pimpleDyMFoam'` was executed. The initial residuals were found in `variable_N` and the local continuity errors in `contLocal_N`. Where N indicates the occurrence inside the time step and the last one is the most important. Initial and final residuals for U in all three directions were checked in addition to the max and mean Courant number in `Courant_0` [63]. The log file output can be viewed with several programs. In this case the post-processing utility `Gnuplot`¹⁸ were preferred. Within the main case-folder a text file containing the script saved the image (.png file) of the residual plot in the `logs` folder (see Appendix R) [70].

¹⁸ Gnuplot is a portable graphing utility for Linux and many other platforms. The command-line driven source code is copyrighted [78].

4 RESULTS AND DISCUSSION

Before looking at the results it is worth having a few things in mind. The complexity of CFD leads to “trial and error” processes which are very time consuming. Countless parameters must be chosen correctly in order to obtain convergence and many test simulations have been done to achieve reliable results. An overview of the 56 simulations is found in Appendix D.3. In addition to these, several simulations that did not converge was also necessary in order to find appropriate set up of the cases.

In order to interpret the result it is useful to highlight the limitations and assumptions made. For all the simulations carried out, the wave state is simplified as it is a 2-D idealized wave and does not include changing wave amplitudes and phases. In that sense wave influence are expected to be more subtle and difficult to interpret in real observations. The effects of buoyancy can be considerable but are not taken into account in this model. As shown in Figure 7 the roughness length has an impact on the wind profile. The correct evaluation of this is a cumbersome process because the wind profile is believed not to be logarithmic during a swell condition [6]. It may be assumed that the ocean surface waves provide the effective roughness hence it is kept constant [8, 68]. Another simplification is that the Coriolis force is neglected (see Ch. 2.2 Boundary layers). In addition only uniform inlet distribution for wind speed and TKE are used. Taken these limitations and assumptions into consideration it is believed that the results are physically correct to a degree that makes it interesting and worthwhile the effort.

Periodic boundary conditions are believed to be beneficial for the simulations. In order to obtain the same results a very long domain would have been required. However this demands enormous computational power which was not available during this work. In the grid independence study it was revealed that a larger domain would possibly also have given a more stable and completely developed TKE (see Figure 14). A finer mesh would be appropriate in order to obtain lower values for y^+ .

As assumed at an early stage, there were benefits in execution time of going from 3-D to 2-D and running in parallel. The result of initially changing from 3-D to 2-D on the execution time was a reduction by a factor of 16. The benefit in speed up due to parallel was tested showing a reduction in the execution time of around 30 % when going from 1 to 2 processors and from 2 to 3 (see Appendix U). The further reduction when using 4 processors was however less. The increase in simulation time was monitored during the grid independence study, showing the increase in simulation time to be 25 % higher than the percentage increase in cell number. The reason that the simulation time is of proportional to the increase in cell number is a result of smaller time steps (eq. 26). Decomposing and reconstructing the processors will take some time as well, the latter in a class of its own when averaging. Comparisons of the different cases show a persistent pattern of increasing execution time when increasing the complexity of the simulation run. For these results it must be taken into account that other processes might have had an influence and thereby they are not very accurate.

Time averaged values of wind speed and the TKE will have the greatest discrepancy for high wind speeds and a rough wave state. For the “standard-case”, the vertical profiles of the instantaneous values and the averaged value of horizontal wind speed and TKE are very similar apart from in the lower region where instantaneous profiles have the highest value. Significant deviations between instantaneous and averaged profiles are seen for the vertical wind speed (see Appendix T.1). This seems reasonable and averaged values of vertical profiles should be preferred depending on the context. For case 1 it was intentional to see instantaneous values and it might not be that pivotal to use average values in that context either seeing as the relative difference between the profiles are the main issue. The horizontal profile figures the greatest amplitude for the instantaneous values of wind speed and TKE which corresponds to the intuitive understanding of averaging (see Appendix T.2). The time averaged has to some extent averaged out the fluctuations. . Because of this all horizontal profiles are instantaneous values. The large scale fluctuations, U^2_{Mean} , has a clear maximum in the lower region as expected because that is where the wind field is mostly influenced by the wave (see Appendix T.3) .

4.1 VALIDITY TEST OF `FIELD_AVERAGE`

One of the disadvantages with OpenFOAM is the lack of information. This validity test of the OpenFOAM averaging utility, `fieldAverage`, may prove to be useful for many others as the results of are rather interesting and clarifying. As an almost perfect match with instantaneous profiles at several time steps is seen it is believed that the process used is sufficiently accurate way of averaging in time for this context (see Figure 16). It is concluded that the utility takes the vertical cell displacement in z-direction into account. The comparison with profiles at several locations downstream shows some discrepancy which is understandable as the flow is dependent on the x-direction (see Figure 17). To fully describe the turbulent flow a new variable should be included, taking account for both the large and small scale turbulent fluctuations (eq. 20).

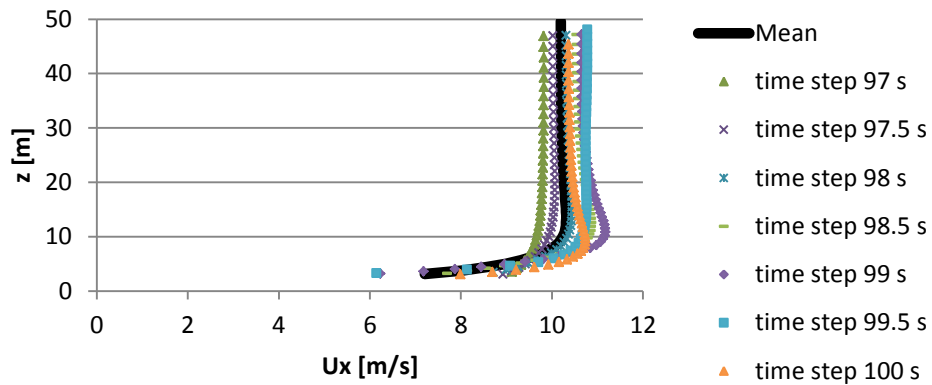


Figure 16: Mean and instantaneous values at several time steps. Wind is aligned with wave propagation. Horizontal profiles of vertical wind speed at $x = 125$ m. Mean is calculated with `fieldAverage`.

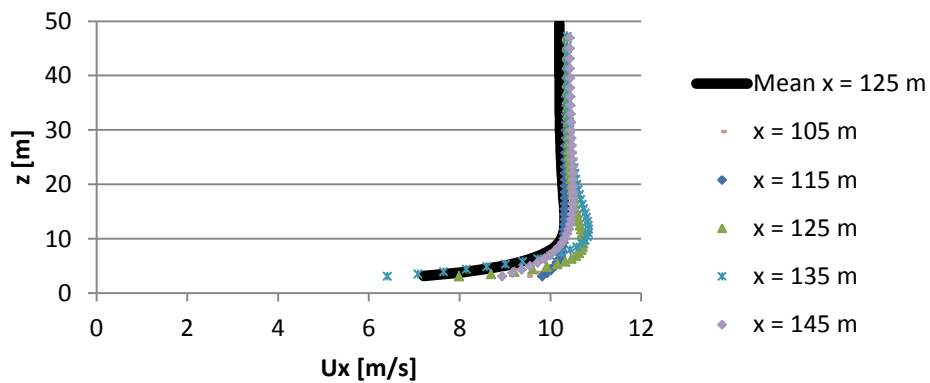


Figure 17: Mean and instantaneous values at several locations downstream. Wind is aligned with wave propagation. Horizontal profiles of vertical wind speed. Mean is calculated with `fieldAverage`.

The figures presented hereafter use both instantaneous and average value depending on their purpose. Thorough investigation of this matter has shown that it is most important to average values for vertical profiles when comparing simulations with different wave states. If not one might end up comparing a wind profile over crest with a wind profile over trough which is noticeably different [9]. It must be taken into consideration for all the instantaneous profiles that an average might look different.

4.2 CASE 1, WIND SPEEDS AND DIRECTION

In case 1 different wind speeds, in the interval 5 m/s to 30 m/s, are studied in detail. This applied wind can be thought of as the geostrophic winds and it has been tested both aligned and opposed with the wave propagation. The wave has amplitude $a = 3.0$ m, wavelength $L = 40$ m, and wave speed $c = 8.0$ m/s. When the wind speed is changed, the initial conditions for k and ϵ should be changed (eq. 27), (eq. 28). It has been tested that a change makes an impact on the TKE. The reason for keeping them constant is that they are only initialization values. One may say that the case creates its own turbulence field as it increases from its initialization value (see Figure 23). In addition it is easier to compare the different simulations when these parameters are unchanged.

The sensitivity study of different wind speeds has revealed several interesting features. The vertical profiles indicates a layer with strong gradient near the surface, as the wind speed approaches the wave speed, followed by a region of approximately constant wind speed from around $z = 20$ m, violating the logarithmic wind profile law (see Figure 18 and Figure 21). The greatest impact on the wind field is seen for a young/developing sea state [41]. For such conditions a pattern that the highest wind speeds occurs somewhere around $z = 15$ [7]. Either a low-level wind maximum or a “knee” will be present in such wind profiles [6, 7, 71]. Above this region the wind speed is smoothly reduced to the geostrophic wind speed in all profiles [8].

Concentrating on case 1.A the height at which the wind speed reaches a constant value is increasing with increasing geostrophic wind speed (see Figure 18). A “knee” is present for the three youngest sea states. It is understandable that these are clearer on the instantaneous profiles as it occurs due to speed up over the wave crest. The exact curve and position of this “knee”, which occurs due to speed up over the waves, is not known as it changes downstream the wave [10]. The vertical wind profiles shows how the wind close to the wave is sucked down and the uplift further away from the surface with a maximum is at $z = 20$ (see Figure 19). The values figured are increasing with increasing wind speed as does the TKE profiles. The turbulence is large near the surface due to “wave pumping” performed by the surface wave on the flow field [72]. Looking at the horizontal profiles (see Figure 20) the wind speed and TKE seems almost unaffected for the mature sea state. The fluctuations and influence by the wave are, as expected, greater the higher the wind speed.

The wind opposing wave situation shows very straight instantaneous wind profiles (see Figure 21). This might be due to speed up over the wave crest, as time averaged profiles are significantly slowed down near the surface. For the lowest wind speed even negative wind speed occurs as it follows the direction of the wave. The vertical wind speed and TKE are similar to the aligned situation although turbulence production is highest when opposed (see Figure 22). The horizontal profiles show that the wind field is influenced by the wave. The horizontal profiles reveal clear “footprints” of the surface wave in the wind field (see Figure 23). Looking at the wind speed the fluctuations seems to be almost independent of the geostrophic wind speed. The TKE is however more dependent on the geostrophic wind as fluctuations are greater with greater wind applied.

It is of major interest to compare case 1.A and 1.B. Starting with the vertical wind profiles they are fairly similar for both situations as the speed up over the wave is cancelled out by averaging. The TKE profiles seem to have similar features as the wind speed for the aligned situation reaching a constant value at $z = 30$ m while the opposed does it at approximately 10 meters below (see Figure 19 and Figure 22). The horizontal profiles reveal a decreasing TKE downstream when aligned and increasing when opposed (see Figure 20 and Figure 23). The intuitive understanding was greatest TKE in the latter case as shear and vertical winds are highest. Therefore the result is believed to be physically correct as it also is supported by the results of Smedman et al. (1999) [71] and Kudryavtsev and Makin (2004) [73] who found that the turbulence production is remarkably increased in an opposed situation. The overall picture that the MBL depends on the wave state is in agreement with models of Sullivan et al. (2008) [6] and like Semedo et al. (2009) [8]. In addition the results from case 1 indicate a good match with field measurements from Smedman et al. (2009) [7] in terms of strong gradients near the surface, the characteristic “knee” and dependence on wave age.

4.2.1 CASE 1.A, WIND SPEEDS ALIGNED

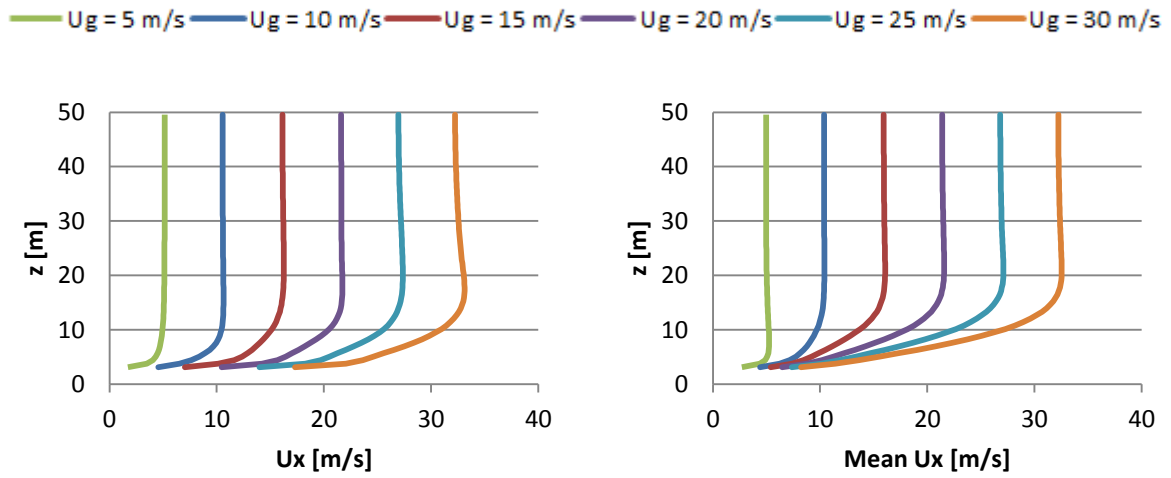


Figure 18: Various wind speeds aligned with wave propagation. Vertical profile of horizontal wind speed and mean horizontal wind speed at $x = 210$ m.

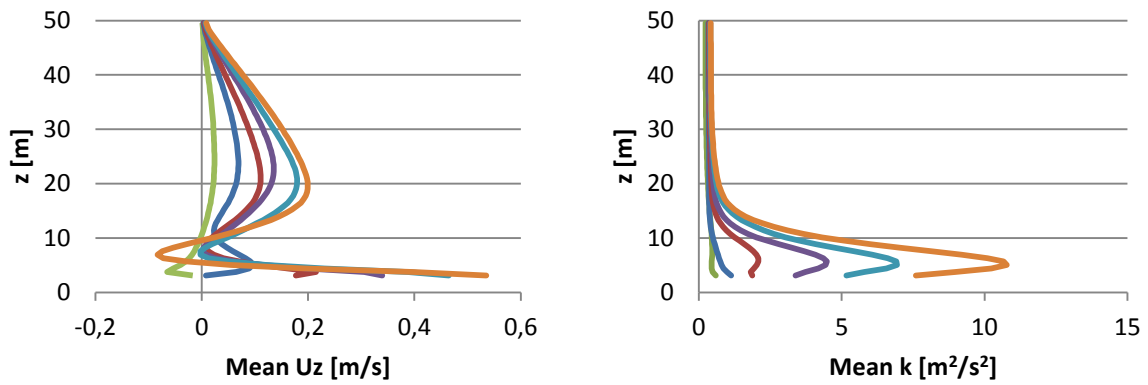


Figure 19: Various wind speeds aligned with wave propagation. Vertical profile of mean vertical wind speed and TKE at $x = 210$ m.

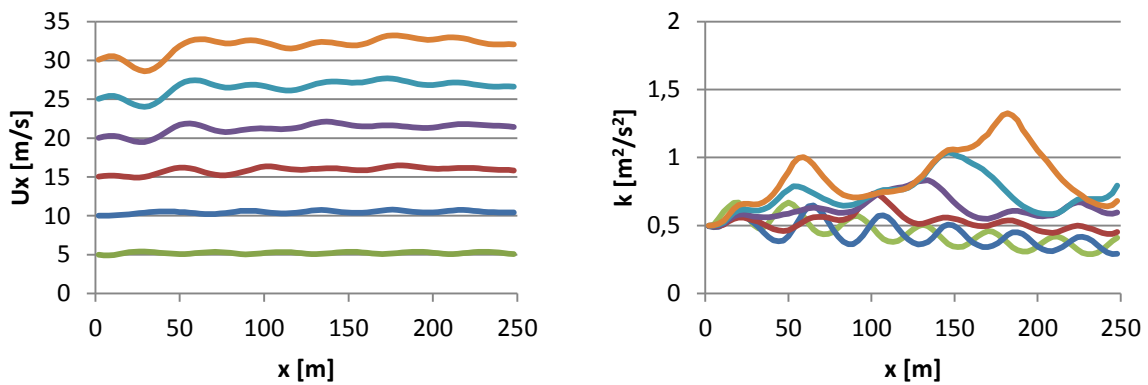


Figure 20: Various wind speeds aligned with wave propagation. Horizontal profile of horizontal wind speed and TKE at $z = 15$ m.

4.2.2 CASE 1.B, WIND SPEEDS OPPOSED

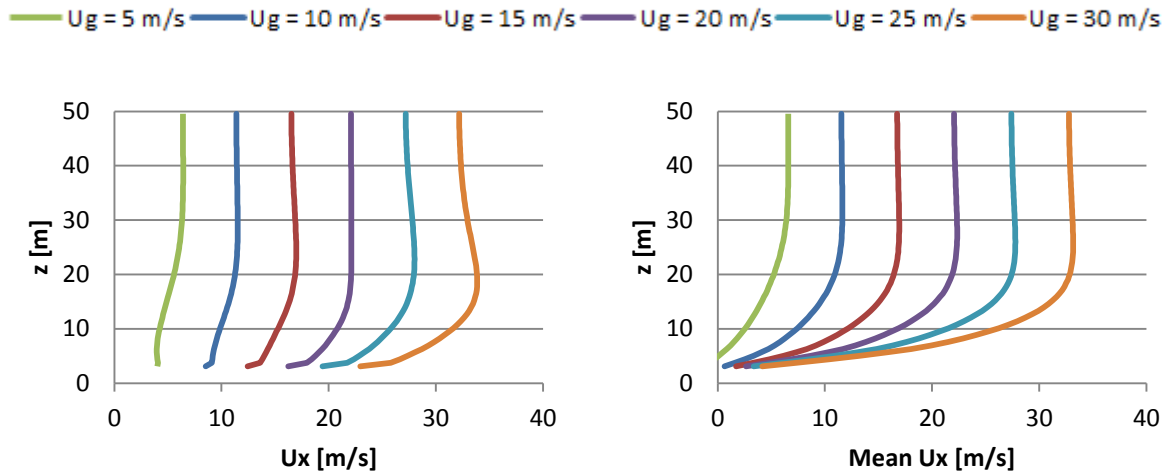


Figure 21: Various wind speeds opposed with wave propagation. Vertical profile of horizontal wind speed and mean horizontal wind speed at $x = 210$ m.

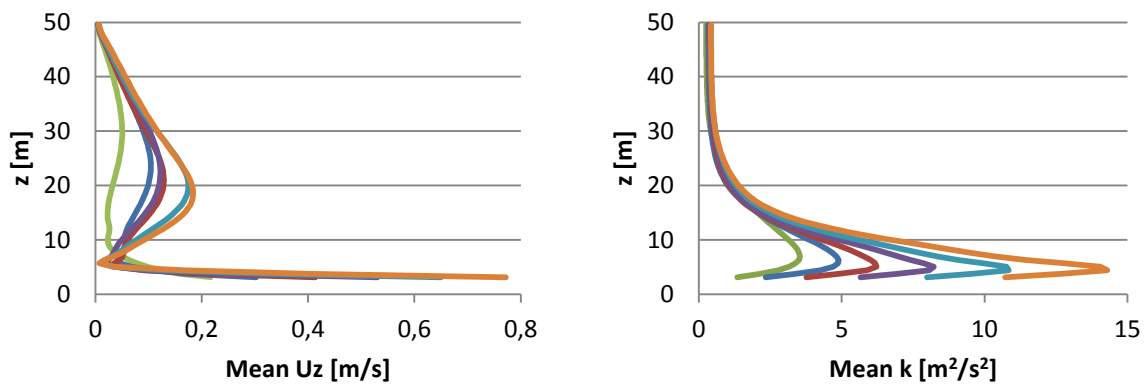


Figure 22: Various wind speeds opposed with wave propagation. Vertical profile of mean vertical wind speed and mean TKE at $x = 210$ m.

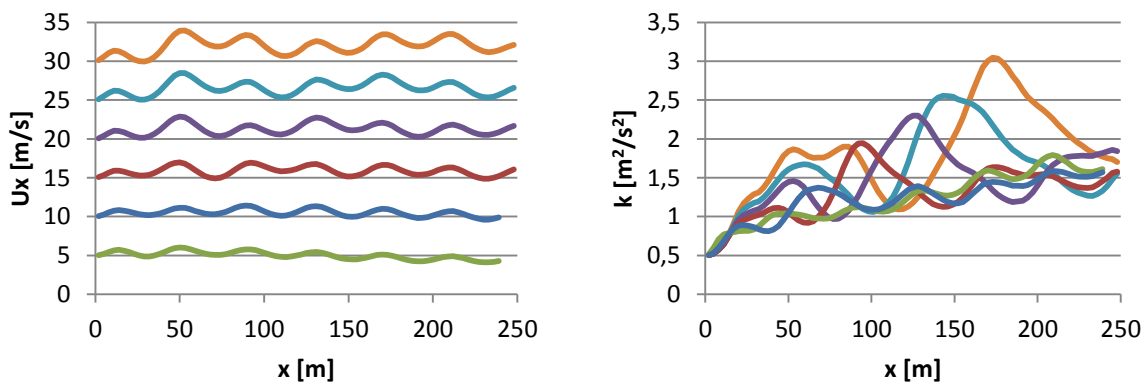


Figure 23: Various wind speeds opposed with wave propagation. Horizontal profile of horizontal wind speed and TKE at $z = 15$ m.

4.3 CASE 2, WAVE STATES

In case 2 a sensitivity study of the wave state with wind opposed with wave propagation, as it produced the most interesting result in terms of turbulence in case 1, changing one wave parameter at the time. The first simulation (green) is run with halved amplitude, wavelength according to the theoretical steepest wave and wave speed from linear dispersion. From there wavelength is doubled for the next simulation (blue) giving a lower wave slope and disobeying linear dispersion as wave speed is kept unchanged. For the third simulation (red) the wave speed is increase by one-third so that it follows linear dispersion. The last simulation (orange) is the "standard-case".

An important issue when comparing different wave states is that the vertical profiles at the same location in space may be taken at different places on the wave. Hence averaged values must be used because wind field is different from trough to crest [9].

Varying the wave parameters gives a clear sign of a coupling between the wave state and the wind field. Changing the wavelength (green-blue) shows that the steepest wave will have make greater impact on both the vertical and horizontal wind speeds (see Figure 24 and Figure 26). It slows down the vertical wind speed in the lower region and pushes it upwards such that the vertical wind speed is 1 m/s higher in the upper region (see Figure 24). The increase in wave speed (blue-red) does not influence the profiles that much. Nevertheless the greatest slowdown on the horizontal wind speed and the highest vertical wind speeds are seen for the simulation with the highest wave speed. When the amplitude is increased (red-orange) similar results as changing the wave length is seen although being clearer now. The "standard-case" is the simulation with the highest wind speeds for both profiles above $z = 20$ m.

Looking at the TKE it is, as expected, seen highest values for the most rough sea state up until $z = 30$ m (see Figure 25). Above this point the profiles for the four simulations coincide. The three most quiet sea states show very similar TKE profiles. A "turbulent spike" is seen close to the ground which Hargreaves and Wright 2007 [74] and Kalvig 2011 [9] also experienced. It is a phenomenon which might occur as a result of limitation in CFD codes. Nevertheless it is also confirmed by real life measurements due to large velocity gradients [53].

The horizontal profiles manifests the findings above (see Figure 26). For the vertical wind speed it reveals "footprints" of the surface wave on the wind profile. The wavelength is reflected in the distance between each crest on the fluctuating profile. Increasing the wavelength leads to greater fluctuations but lower wind speed at this height. Changing the wave speed does not affect the fluctuations that much but the peaks on the curves occur at different locations as the wave crests does. Once again the greatest amplitude gives greatest wave-induced wind and fluctuations. It is not as easy to interpret the horizontal TKE profiles but impacts of the wave are seen. Once again the roughest sea state fluctuate the most with the highest values, occurring above the wave crest. It shows increasing fluctuation downstream which might indicate that the flow field is not fully developed.

The simulations confirm the intuitive understanding of increasing wave states results in increasing wind speed and TKE. A younger sea state would most likely have revealed an even greater impact. Although the impact on the flow field may not be great in absolute terms, it is important to look for trends. The code has been tested for a greater range of wave states underlining the features mentioned. In order to simulate more severe sea states and study this properly larger domain would be needed. If simulations with for instance longer wavelengths are done within this domain only a few wave crests will be captured and the results will not be reliable. The relationship and interdependence of wind and wave speed is interesting. Ideally one might have any wind speed over any wave speed. Mature sea states with different swell situations are examined in the next case. This case manifests the findings of Sullivan et al. (2008) [6] and Smedman [7] and Semedo et al. (2009) [8] mentioned initially about the importance of considering the wave state when simulating turbulence.

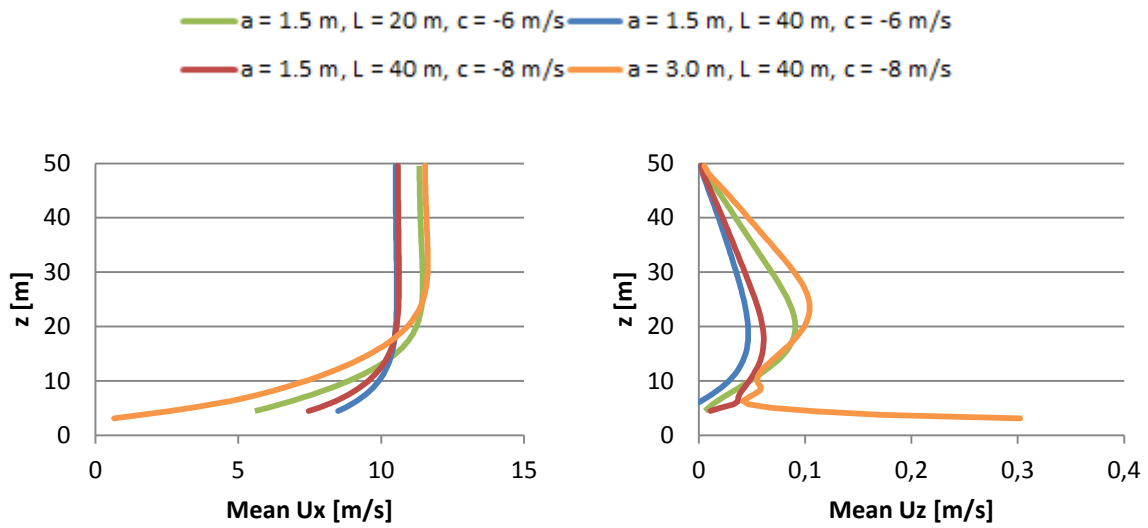


Figure 24: Various wave states opposed with wave propagation. Vertical profile of horizontal wind speed and mean horizontal wind speed at $x = 210$ m.

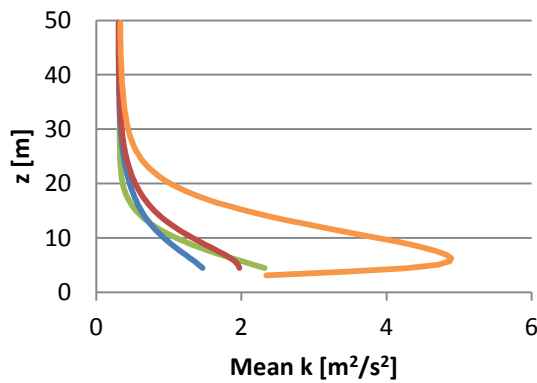


Figure 25: Various wave states opposed with wave propagation. Vertical profile mean TKE at $x = 210$ m.

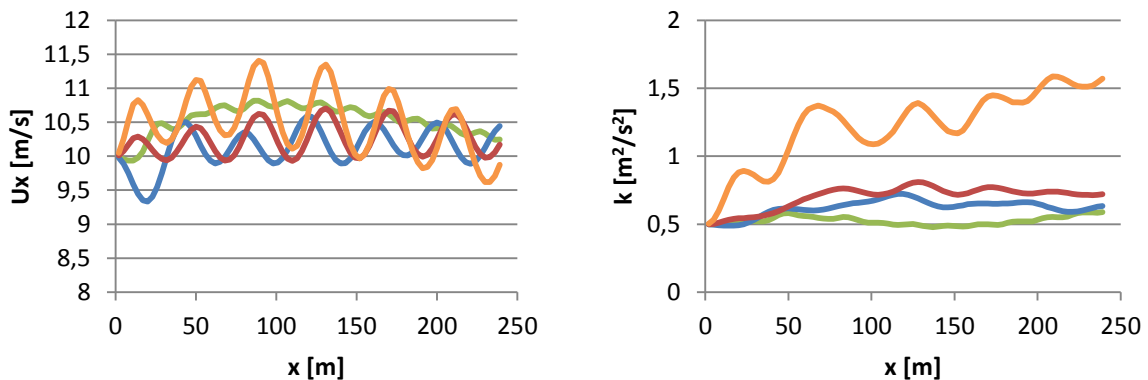


Figure 26: Various wave states opposed with wave propagation. Horizontal profile of horizontal wind speed and TKE at $z = 15$ m.

4.4 CASE 3, SULLIVAN ET AL. (2008)

In case 3 simulations comparable to Sullivan's LES simulations are performed. The domain, the wind speed and wave state are similar to Sullivan's set up and wind and turbulence over two different swell situations, a stationary bumpy surface and a flat surface is studied. The wave has amplitude $a = 1.6$ m, wavelength $L = 100$ m, and wave speed $c = 12.5$ m/s.

There are seven essential differences between the Sullivan's model and the one in this thesis. The first one is regarding the wave movements where Sullivan's is more mathematically advanced as it applies a grid transformation to the flow equations in order to get an effect of a moving wave [6]. The wave used in this thesis on the other hand really moves. The second is that although Sullivan's wave is uniform in the y -direction (2-D) the computational domain is 3-D. This makes it possible to have a small angle between the wind and waves. The fourth is that the flow in Sullivan's work is driven by geostrophic pressure gradient. In addition this reconstruction is only 100 m high compared to Sullivan's 800 m. Two completely different turbulence models are used in this project and Sullivan's being RANS and LES respectively (see 2.8 Turbulence models). Last not least Sullivan's model is periodic in horizontal direction. This is significant as the flow will pass many wave crests compared to reasonably few in this model. As a result there will be some differences in the flow field of the two models and the focus will be to obtain the same features.

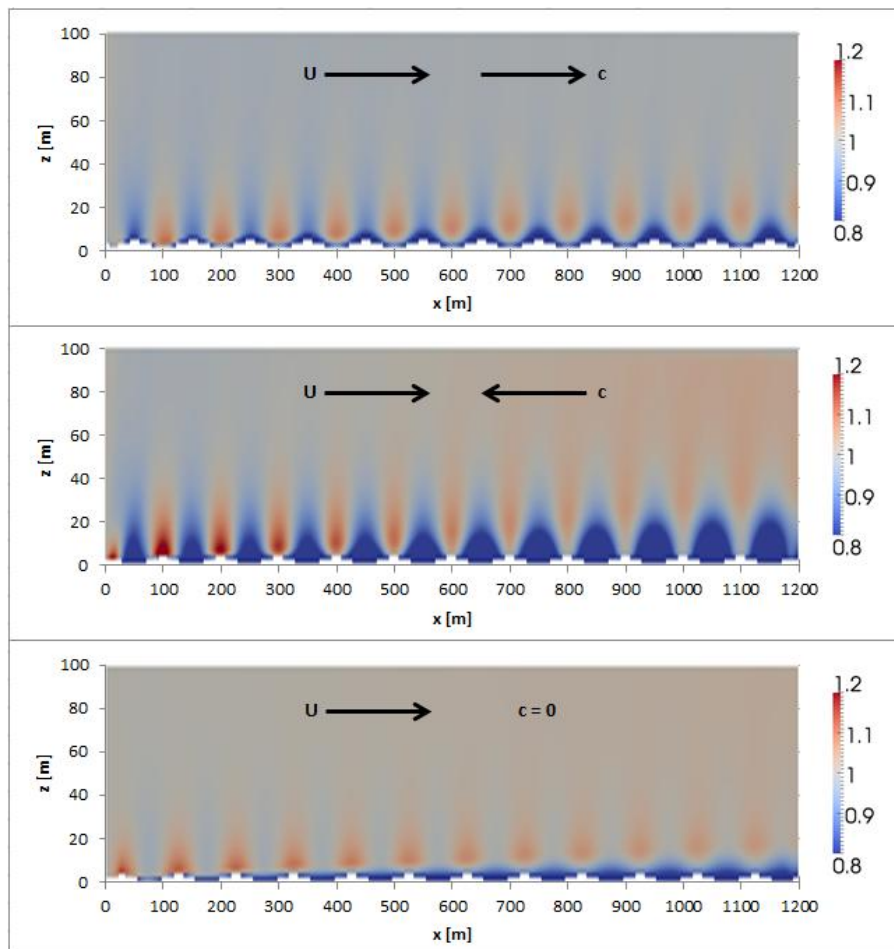


Figure 27: Contours of the horizontal wind field for the situation of aligned (top) and opposed with wave propagation (middle), and stationary waves (bottom) from the k - ϵ model. The non-dimensional field shown is mean U_x / U_g .

Note: The super geostrophic winds near the surface in all panels. The colour bar is different from Figure 28.

It is clear that the shape and direction of the wave influences the flow field. The pattern in the 3 different situations is noticeably different. Examination reveals good compliance with Sullivan's result in an aligned situation (wave age ≈ 2.5) (see Figure 27). The contours show an expected coupling between the wind and waves [6]. The horizontal wind speed is accelerated over the wave troughs and slowed down over the wave crests which are supported by Sullivan's (see Figure 28). The slowdown is greatest in an opposed situation on the other hand, where it occurs over wave crest. This leads to an increasing wind speed in the higher region in the last part of the domain. The stationary bumps have the most uniform wind speed in agreement with Sullivan's. Nevertheless accelerated winds greater than the geostrophic are visible above each wave trough, as the streamlines are compressed, which is not seen clearly for this situation in Sullivan's. Although not being able to examine the boundary layer properly as the domain is too short, there are indications that the opposed situation has the thickest boundary layer. The reason that the colour bar is different from Sullivan's is because of the applied geostrophic wind speed at $z = 100$ m for the $k-\epsilon$ model.

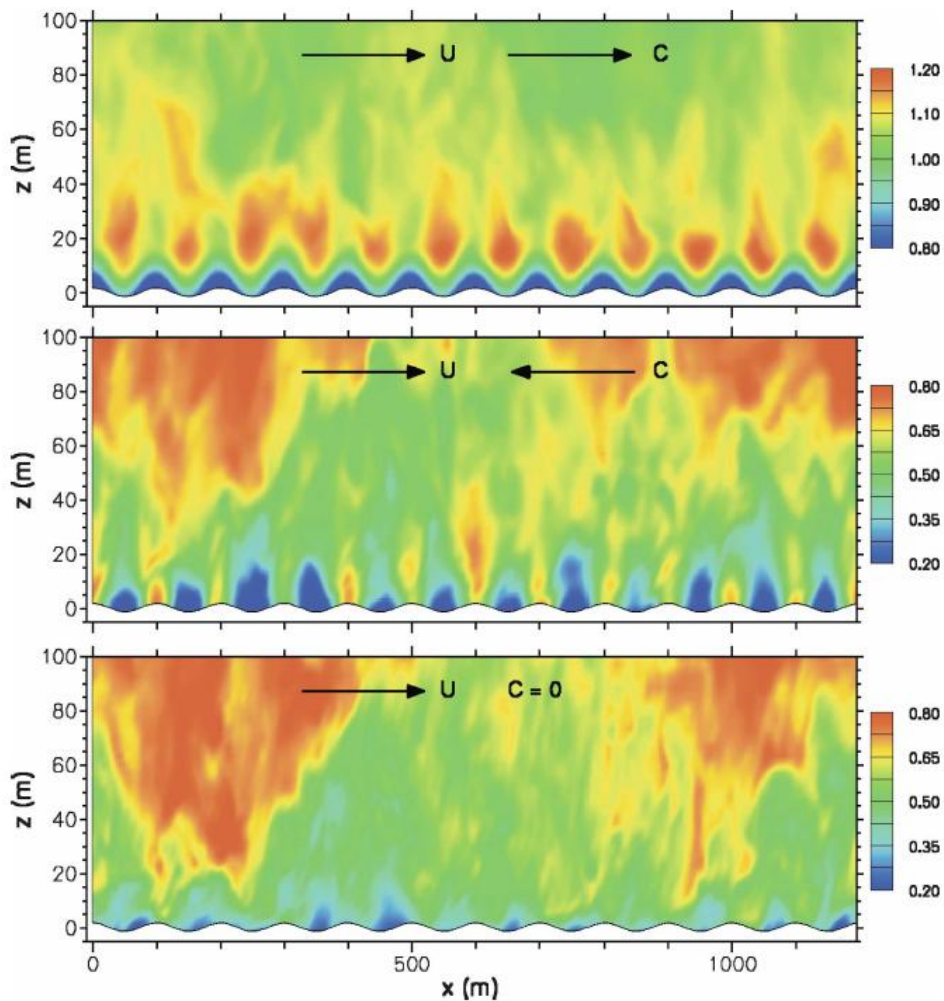


Figure 28: Contours of the horizontal wind field for the situation of aligned (top) and opposed with wave propagation (middle), and stationary waves (bottom) from Sullivan's LES model. The non-dimensional field shown is mean U_x / U_g .

Note: The colour bar changes between the top and middle panel. The super geostrophic winds near the surface in the top panel

A pressure perturbation in the front and back of the wave dumps creates a vertical wind field (see Figure 29). As stated in Sullivan's it is clearly dependent on the wind-wave orientation and wave age as the horizontal wind. For the situation of aligned waves, positive patches of uplift form downstream of the wave and upstream for the two latter situations. When positive vertical winds occur in front of the obstacles, negative are seen behind and vice versa. The values of these vertical winds are highest when opposed and lowest for stationary bumps. These results are all in agreement with Sullivan's underlining that swell conditions impacts the vertical wind field (see Figure 29).

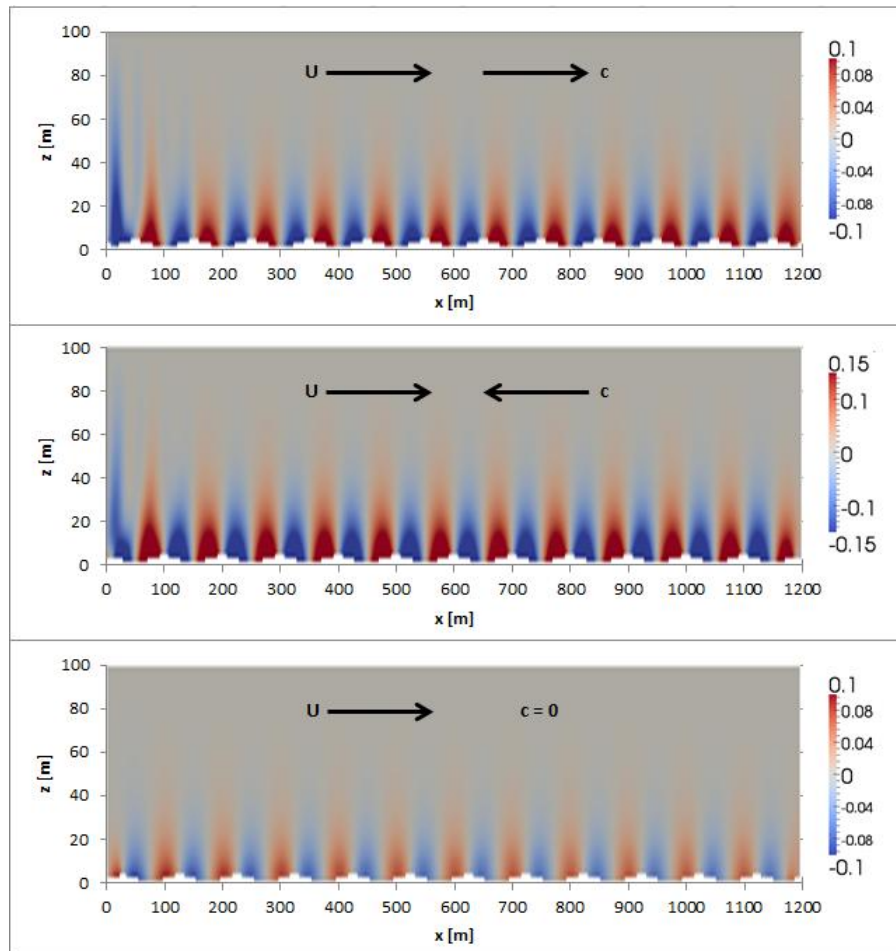


Figure 29: Contours of the vertical wind field for the situation of aligned (top) and opposed with wave propagation (middle), and stationary waves (bottom) from the k- ϵ model. The non-dimensional field shown is mean U_z / U_g .

Note: The colour bar is different for the middle panel.

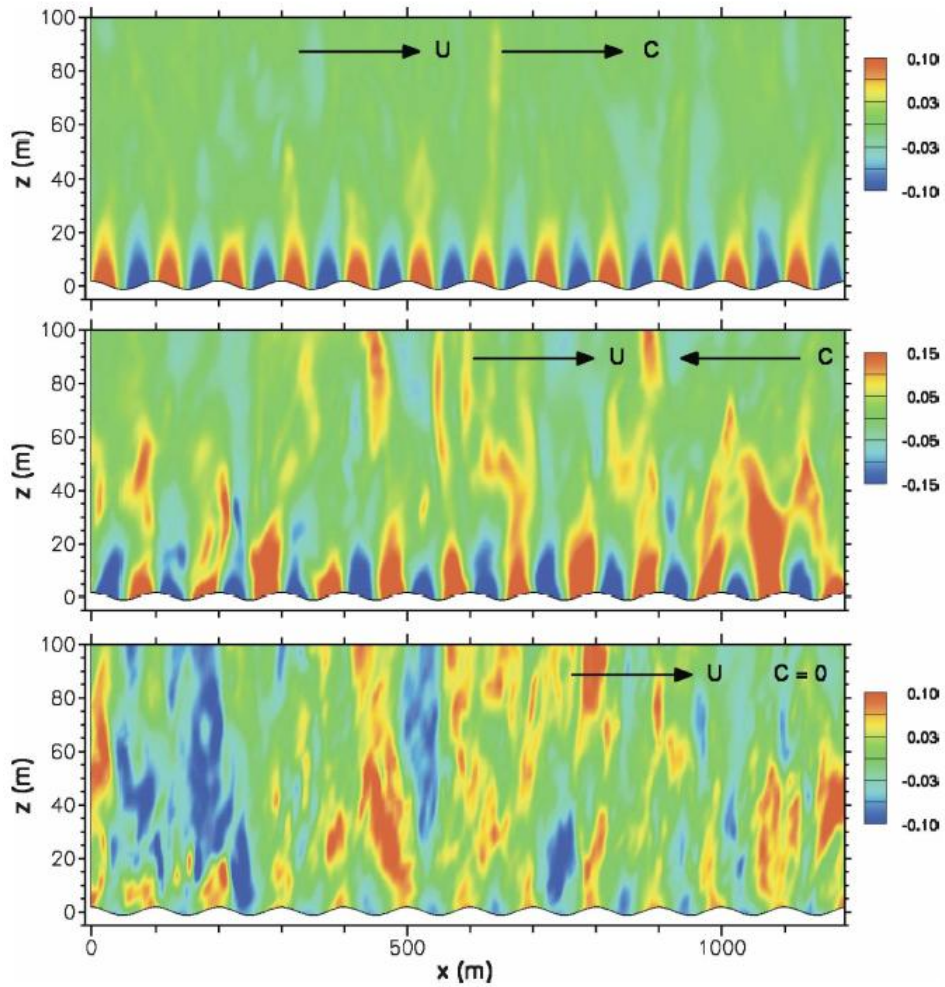


Figure 30: Contours of the vertical wind field for the situation of aligned (top) and opposed with wave propagation, (middle) and stationary waves (bottom) from Sullivan's LES model. The non-dimensional field shown is mean U_x / U_g .

Note: The colour bar is different for the middle panel.

The pressure field near the sea is a key to understanding the wave-wind interaction. The waves impact the pressure distribution well above the surface (see Figure 31). The figure shows a negative pressure at the inlet when aligned and a positive when opposed. This is because the pressure is set to zero at the outlet and hence the inlet is compensating for this. The wave drives the pressure and one can clearly see a link between direction of the wave and pressure. The weakest pressure fluctuations are seen in the aligned situation and the strongest in the opposing one. In the former the negative pressure pattern is slightly behind the wave crest and ahead for the latter. These features are very similar to the results compared to (see Figure 32).

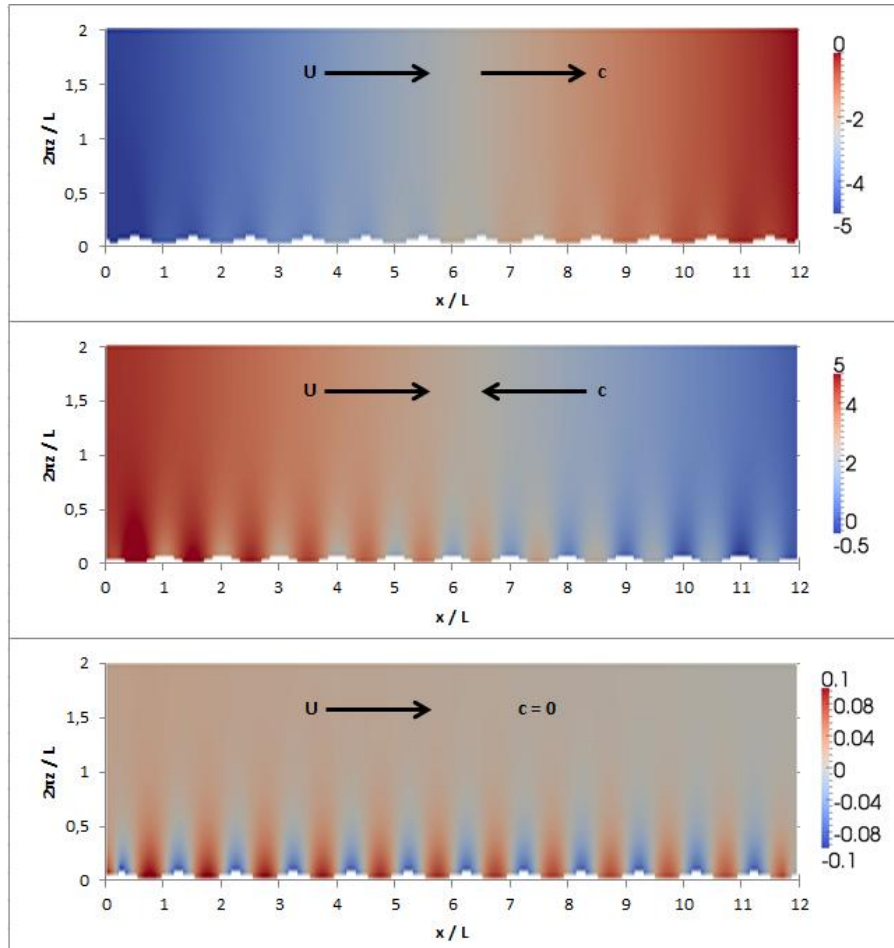


Figure 31: Contours of the pressure for the situation of aligned (top) and opposed with wave propagation (middle), and stationary waves (bottom) from the $k-\epsilon$ model. The non-dimensional pressure field shown is p / U_g^2 .

Note: The colour bar is different from Figure 32.

The vertical and horizontal coordinates in Figure 31 and Figure 32 are made dimensionless with the surface wavelength L .

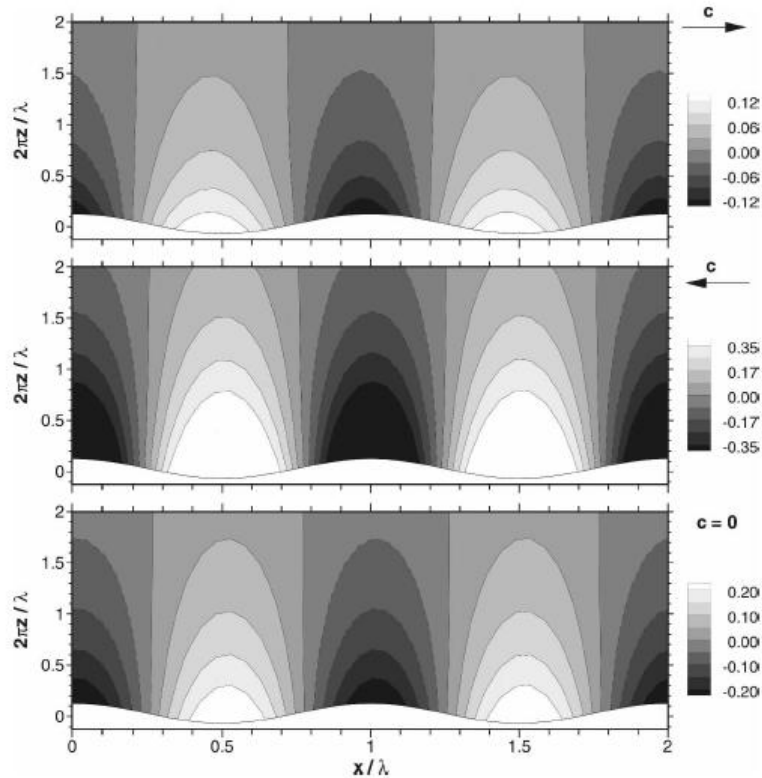


Figure 32: Contours of the pressure for the situation of aligned (top) and opposed with wave propagation, (middle) and stationary waves (bottom) from Sullivan’s LES model. The non-dimensional pressure field shown is p / U_g^2 .

Before looking at the vertical profiles it must be taken into account that Sullivan’s profiles are averaged in both time and space. The profiles for the horizontal wind deviations from the geostrophic shows reasonably good compliance for the aligned situation although Sullivan’s figures a greater low-level jet (see Figure 33). The opposed situation matches to some extent, while the stationary bumps and no waves (hidden behind the squares) does not match very well. In the LES experiments the opposed situation complies with the profiles of stationary bumps and a flat surface, while for the k-ε model the aligned does, which is not understood.

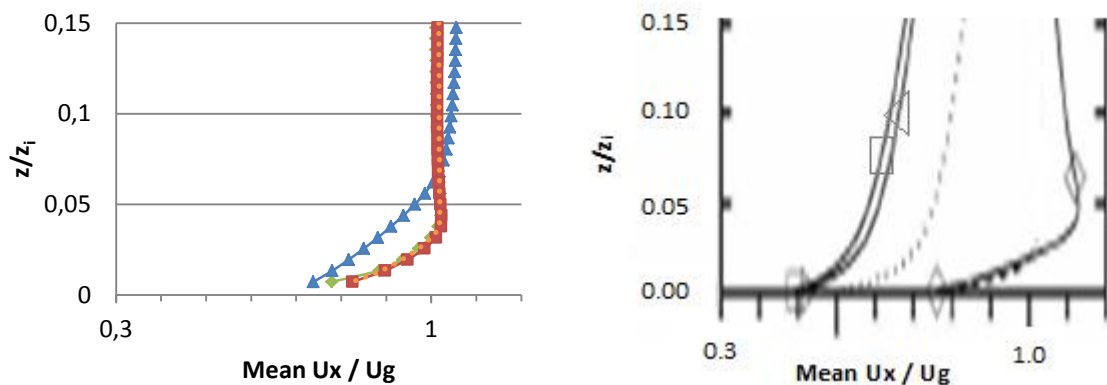


Figure 33: Vertical profile of the deviation of mean horizontal wind speed from geostrophic wind speed and mean vertical wind speed for the situation of aligned (diamonds) and opposed with wave propagation (triangles), stationary (squares) and no waves (dotted) from the k-ε model at $x = 1050$ m (left) and Sullivan’s LES model (right) .

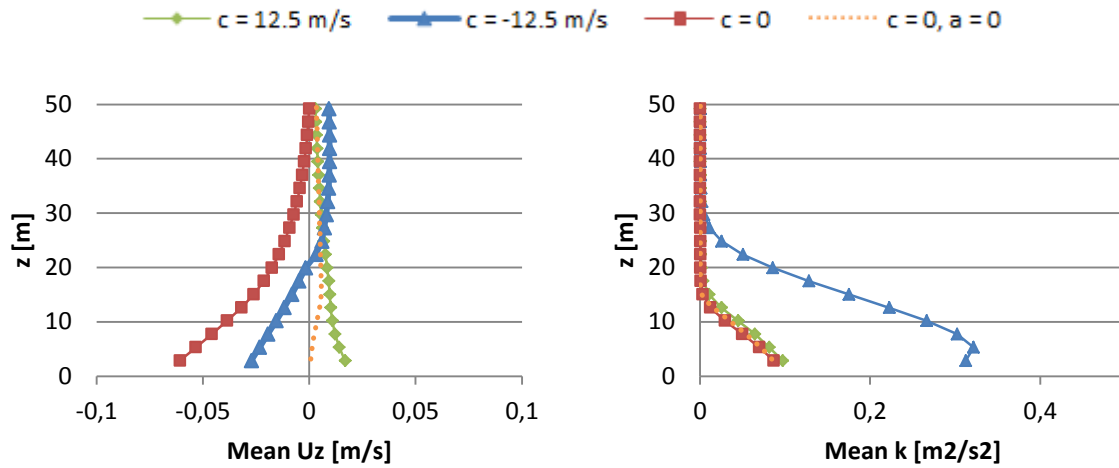


Figure 34: Vertical profile of mean vertical wind speed and mean TKE for the situation of aligned and opposed with wave propagation, opposed, stationary and no waves at $x = 1050$ m.

Note: For the situation of stationary bumps averaging in time gives the same profile as instantaneous values and hence the averaging is done in space from 5 profiles over a 200 m range.

As mentioned in Ch. 2.1.1 Extraction of wind energy, the wind flow in the vertical direction is of great importance. It has a positive gradient in the aligned and flat surface situation which seems reasonable (see Figure 34). When opposed it has a negative gradient close to the surface as the wind flow follows the wave propagation near the surface due to the Ekman's balance [6]. Looking at the TKE profile the opposed situation differs from the rest and shows the highest values until $z = 30$ m which is also in agreement with Sullivan's (see Appendix V). The other three situations show almost exactly the same profile with an aligned situation having slightly higher values in the lower region. This is in contrast to Sullivan's where the stationary bumps have the next highest turbulence production. Nevertheless the TKE dependence on wind-wave orientation, wave age and the wave state in general is highlighted in this and the reference model.

LES is much more demanding and the results are not necessarily better [9]. In general the results highlights that waves may impact the entire MBL. Although many features from Sullivan's are seen it needs to be underlined that the results from the $k-\epsilon$ model presented here are less refined and accurate. At the same time the $k-\epsilon$ model is easier and demands less computational force.

4.5 RESIDUALS

As shown in Figure 35 the residual values are satisfactory. The reason that no information is provided before time step 10 is that the simulation is restarted at that time step and only the newest log file is kept. It is most demanding to obtain small values for pressure. The value of U_y might be dependent on the fact that there is only one cell in the y -direction. It is important that local continuity errors are small (see Appendix S). However residuals are satisfactory when a case is converging and no further focus on this matter is needed.

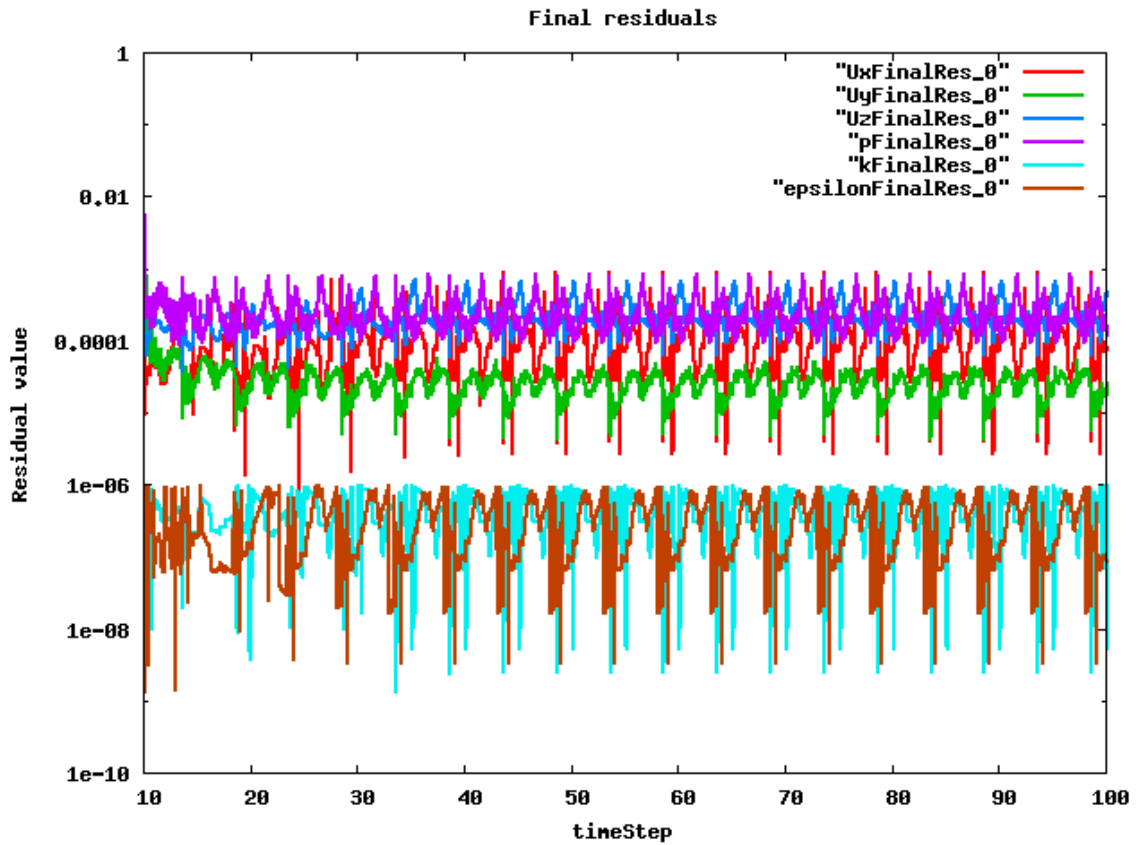


Figure 35: Final residuals "standard-case"

5 CONCLUSIONS

5.1 CONCLUDING REMARKS

In order to examine the interaction between wave and atmospheric wind a k - ϵ model with the capability of solving a moving sinusoidal wave was established. The model was used to simulate a wide range of wave states with different wind speeds aligned and opposed with the waves.

First of all it can be concluded that there is a need to be critical when interpreting results of simulations and treat them as complementary to real-life measurements. Models can at best give an impression of wind-wave interactions. The precision is to a large extent dependent on the spatial resolution. The model used is grid independent and has fairly good values for y^+ providing a good basis for the sensitivity studies. Periodic boundary conditions would be a major benefit for the simulations as the flow is not fully developed at the outlet of the domain.

The introduction of the time averaging function was very interesting and a validity test, comparing it to instantaneous profiles in time and space, was successful. It has been proved that averaging vertical profiles provided more reliable results, in particular for high wind speeds and roughest wave states, while horizontal profiles on the other hand should use instantaneous values. It is believed that the averaging procedure is physically correct and takes the wave movement into account because it is in general agreement with a manual averaging in time and space. This is an important discovery as documentation on the averaging utility is lacking.

Analysis of the wind profiles with several setups shows a persistent pattern and various interesting features. The overall picture that the wind field in MBL depends on the wave state and this is in agreement with Sullivan et al. (2008) [6] and Smedman et al. (1999) [71]. In addition the results from the sensitivity studies indicate a good compliance with measurements like Semedo et al. (2009) [8]. The wind speeds are highest over the wave crest as stated by Kalvig et al. (2011) [10] and Janssen (1989) [41]. For the simulations with a young/developing sea state we therefore notice a wind maximum or a "knee" at $z = 15$ m. Below this point the wind speed decreases rapidly with height, although being close to constant above that point. Studying the horizontal and vertical profile of wind speed and TKE it was found that the values are lower and less fluctuating for an aligned than opposed situation and this was as anticipated. This is supported by the findings of Sullivan et al. (2008) [6], Smedman et al. (1999) [71] and Kudryavtsev and Makin (2004) [73]. The latter part of the sensitivity study was focusing on a changing wave state. The steeper the wave the greater the impact on the wind profile. "Footprints" of the surface wave are visible in the flow field.

The fact that fast-running swells have an effect on the wind field in the MBL is highlighted in our model. It is shown that the wave speed relative to the wind speed is pivotal. In agreement with Sullivan's it is concluded that the mean wind profile and TKE are conditional on the very nature of the wave. An aligned situation accelerates the flow over the wave crest and increases the boundary layer thickness while it is decelerated close to the surface when opposed. This deceleration yields the highest vertical wind speeds and turbulence production. Although the LES experiment is believed to give the most precise and refined picture the less demanding k - ϵ model used highlights the same features.

The research question has been well answered, and all the goals and objectives outlined initially have been fulfilled. Unfortunately some important discoveries were made after all the simulations were run. There are many stumbling points when working with CFD, and in particular with OpenFOAM, where scarce documentation means a high input threshold. However it pays off to take on the steep learning curve, as there are no expensive licenses which other similar programs have. Hopefully this thesis has given some useful answers to other readers. It will be helpful in the further PhD work of Kalvig and hopefully also in the research found project undertaken by UiS and StormGeo.

5.2 FUTURE WORK

The established model has been further improved showing promising results. However it presents areas for future improvement. There are several interesting aspects which would be interesting to study, this includes:

- More detailed analysis of the wave-wind interaction including a convection term taking account for buoyancy, periodic boundary conditions a more realistic wave and various surface roughness's including a study of momentum flux with a finer mesh. Seeing as the code used in this project does not handle a periodic boundary condition it is recommended to create a flat surface before/after the wave where the wind flow will resemble a logarithmic profile. Alternatively a larger domain would probably achieve the same results.
- 3-D simulation with the capability to have an angle between the wind and wave directions.
- Case study and comparisons with observations such as the FINO data. The FINO data are real observations from a measurement platform in the North Sea [75].
- Experimenting with different turbulence models. Test the different RANS models and examine the different result in comparison with LES modelling.
- Turbulence post-processing. How can one get the best representation of the turbulent flow when using $k-\epsilon$? Will the TKE alone give the best picture and how can instantaneous speed be added? The time average utility used is not a complete way of doing this and a new variable including both wind speed and TKE should be added (eq. 20).
- Scale up in order to simulate larger wave amplitudes which follow linear dispersion. Implement one or several turbines in order to study wake interactions and search for the optimal positioning of the turbines in a farm. This requires high performance computers.

Some of these aspects will be embedded in the PhD work of Kalvig, at UiS/StormGeo in corporation with NORCOWE.

BIBLIOGRAPHY

- [1] US Gov, Dept of Energy, "Energy Information Administration – Official Energy statistics from the U.S. Government," 2009. [Online]. Available: <http://www.eia.doe.gov>. [Accessed Januar 2010].
- [2] US Gov, Dept of Energy, "US Dept of Energy on Green House Gases," 2009. [Online]. Available: <http://www.eia.doe.gov/bookshelf/brochures/greenhouse/Chapter1.htm>. [Accessed Januar 2012].
- [3] Dolores EM, "Why offshore wind energy?," Madrid Spain, 2010.
- [4] European Commission, *Commission welcomes adoption of climate energy*, Brussels: Press Release, 2009.
- [5] Sykes B, de Villiers P, *Carbon trust, Offshore wind power: big challenge big opportunity*, Liverpool: Renewable UK, 2010.
- [6] Sullivan PP, Edson JB, Hristov T, McWilliams JC, "Large-eddy simulations and observations of atmospheric marine boundary layers above nonequilibrium surface waves," *Journal of the Atmospheric Sciences*, vol. 65, no. 4, pp. 1225-1245, 2008.
- [7] Smedman A, Högström U, Sahlee E, Drennan WM, Kahma KK, Pettersson H, Zhang F, "Observational study of marine atmospheric boundary layer characteristics during swell," *Journal of the Atmospheric Sciences*, vol. 66, no. 9, pp. 2747-2763, 2009.
- [8] Semedo A, Saetra Ø, Rutgersson A, Kahma KK, Pettersson H, "Wave-induced wind in the marine boundary layer," *Journal of the Atmospheric Sciences*, vol. 66, pp. 2256-2271, 2009.
- [9] Kalvig S, "ABL simulations by the use of OpenFOAM and the K-Epsilon model," UiS, Project work for the the course DOF710, 2011.
- [10] Kalvig S, Gugmestad OT, Winther N, "A literature review on implications of wave-influenced wind and atmospheric stability for offshore wind energy," UiS, StormGeo, 2011.
- [11] Kalvig S, *Wave-Wind interaction and changing atmospheric stability - implications for design requirements and energy output for offshore wind turbines*, UiS: Project work for the the course DOF210, 2010.
- [12] Kalvig S, *Simulation of wave induced wind fluctuation with OpenFOAM*, Paris: StormGeo, 2011.
- [13] Lie Ø, "Skal finne ut når vinden blåser," *Teknisk Ukeblad*, pp. 14-15, 15. March 2012.
- [14] Obhrai C, Kalvig S, Gudmestad OT, *A review of current guidelines and research on wind modelling for the design of offshore wind turbines*, UiS, 2012.
- [15] Obhrai C, *Improved Design Criteria and Forecast for Energy Yield from Offshore Wind Turbines*, UiS, StormGeo, 2011.
- [16] Encyclopædia Britannica., "windmill," Encyclopædia Britannica Online Academic Edition. Encyclopædia Britannica Inc., 2012. [Online]. Available: <http://www.britannica.com/EBchecked/topic/645158/windmill>. [Accessed February 2012].

- [17] Encyclopædia Britannica. , "history of technology," Encyclopædia Britannica Online Academic Edition. Encyclopædia Britannica Inc., 2012. [Online]. Available: <http://www.britannica.com/EBchecked/topic/1350805/history-of-technology>. [Accessed February 2012].
- [18] Morthorst PE, Auer H, Garrard A, Blanco I, *The economics of wind power*, Wind energy - the facts, 2009.
- [19] Williams A, "A Buoyant Future for Floating Wind Turbines?," Renewable energy world, May 2011. [Online]. Available: <http://www.renewableenergyworld.com/rea/news/article/2011/05/a-buoyant-future-for-floating-wind-turbines>. [Accessed February 2012].
- [20] Renewable UK, "Wind energy technology," 2010. [Online]. Available: <http://www.bwea.com/ref/tech.html>. [Accessed January 2012].
- [21] Siemens Danmark , "Fakta om offshore vindmøller i Danmark," 2012. [Online]. Available: <http://www.nwe.siemens.com/denmark/internet/dk/presse/klimaloesninger/Pages/Fakta-Off-shore.aspx>. [Accessed March 2012].
- [22] Renewable UK, "How does an offshore wind farm work?," 2010. [Online]. Available: <http://www.bwea.com/offshore/how.html>. [Accessed January 2012].
- [23] NEK IEC 61400-3, "Wind turbines, Part 3: Design requirements for offshore wind turbines," Geneva, Switzerland, 2009.
- [24] Khalil M, Melheim JA, Sælen L, "Modelling in FLACS - Wind progress report 2011," NORCOWE, 2012.
- [25] Vestavind Offshore, "Facts about Havsul I," [Online]. Available: <http://vestavindoffshore.no/havsul/fakta-om-havsul/?spraak=en>. [Accessed January 2012].
- [26] Díaz-González F, Sumper A, Gomis-Bellmunt O, Villafañila-Robles, R, "A review of energy storage technologies for wind power applications," *Renewable and Sustainable Energy Reviews*, vol. 16, pp. 2154-2171, 2012.
- [27] Korpass M, Holen TA, Hildrum R, "Operation and sizing of energy storage for wind power plants in a market system," *Electrical Power and Energy Systems* , vol. 25, pp. 599-606, 2003.
- [28] Burton T, Sharpe D, Jenkins, D, Bossanyi E, *Wind energy handbook*, John Wiley & Sons, Ltd, 2001.
- [29] DNV, RISØ, "Guidelines for Design of Wind turbines," DSI Grafisk Service, Copenhagen, Denmark, 2001.
- [30] Renewable energy UK, "Betz Limit," January 2007. [Online]. Available: <http://www.reuk.co.uk/Betz-Limit.htm>. [Accessed February 2012].
- [31] Hartwanger D, Horvat A, "3D modelling of a wind turbine using CFD," NAFEMS Conference, United Kingdom, 2008.
- [32] NEK IEC 61400-1, "Wind turbines, Part 1: Design requirements for wind turbines," 2005.
- [33] Wagner R, Antoniou I, Pedersen SM, Courtney NS, Jørgensen HE, "The Influence of the Wind Speed Profile on Wind Turbine Performance Measurements," *Wind energy*, vol. 12, pp. 348-362, 2009.

- [34] Dyrbye C, Hansen SO, Wind loads on structures, John Wiley & Sons, 1996.
- [35] Edson J et al, "The coupled boundary layers and air-sea transfer experiments in low winds," *Bulletin of the American Meteorological Society*, vol. 88, no. 3, pp. 341-356, 2007.
- [36] Pyatt HE, Albrecht BA, Fairall C, Hare JE, Bond N, Minnis P, Ayers JK, "Evolution of Marine Atmospheric Boundary Layer Structure across the Cold Tongue - ITCZ Complex," *Journal of Climate*, vol. 18, pp. 737-753, 2005.
- [37] Sikora TD, Ufermann S, "Chapter 14. Marine atmospheric boundary layer cellular convection and longitudinal roll vortices," in *Synthetic aperture radar marine users manual*, Washington, DC, US. Department of commerce, 2004, pp. 321-330.
- [38] Grachev AA, Fairall CW, "Upward momentum transfer in the marine boundary layer," *Journal of Physical Oceanography*, vol. 31, pp. 1698-1711, 2001.
- [39] Nilsson OE, Rutgersson A, Smedman AS, Sullivan PP, "Convective boundary-layer structure in the presence of wind-following swell," *Quarterly Journal of the Royal Meteorological Society*, 2012.
- [40] Edson J, Paluszkiwicz T, Sandgathe S, Vincent L, Goodman L, Curtin T, Hollister J, Colton M, "Coupled Marine Boundary Layers and Air-Sea Interaction Initiative: Combining Process Studies, Simulations, and Numerical Models," 1999.
- [41] Janssen PAEM, "Wave-induced Stress and the Drag of Air Flow over Sea Waves," *Journal of Physical Oceanography*, vol. 19, pp. 745-754, 1989.
- [42] Hanley KE, Belcher SE, Sullivan PP, "A global climatology of wind-wave interaction," *Journal of Physical Oceanography*, vol. 40, pp. 1263-1282, 2010.
- [43] Semedo A, Sušelj K, Rutgersson A, Sterl A, "A global view on the Wind sea and Swell Climate and Variability from ERA-40," *Journal of Climate*, vol. 24, pp. 1461-1479, 2011.
- [44] Parr H, Holter Ø, Ingebretsen F, Fysikk og energiressurser, Oslo, 2010.
- [45] Young IR, Wind generated ocean waves, Elsevier, 1999.
- [46] Stokes GG, On the theory of oscillatory waves, Camb Trans viii, 1847.
- [47] NORSOK N-003, "Actions and action effects," Standard Norge, 2007.
- [48] Ardhuin F, Chapron B, Collard F, "Observation of swell dissipation across oceans," *Geophysical research letters*, 2009.
- [49] Makin VK, *On the Possible Impact of Following-Swell on the Atmospheric Boundary Layer*, Springer Science+Business Media BV, 2008.
- [50] Vikebø F, Furevik T, Furnes G, Kvamstø NG, Reistad M, "Wave height variations in the North Sea and on the Norwegian Continental Shelf, 1881-1999," *Continental Shelf Research*, pp. 251-263, 2002.
- [51] Bykjedal Ø, Kravik R, Kjeller Vindteknikk, "Oppdragsrapport A10-09," NVE, Oslo, 2009.

- [52] Anda I, "Petroleum safety authority Norway," September 2005. [Online]. Available: <http://www.ptil.no/nyheter/tropisk-storm-kan-ikke-ramme-norsk-sokkel-article2247-24.html>. [Accessed Januar 2012].
- [53] Veersteg HK, Malalasekera W, An Introduction to Computational Fluid Dynamics, Essex, England: Pearson Education Limited, Second edition, 2007.
- [54] Hjertager BH, *Computatinal Analysis of Fluid Flow Processes*, UiS, Corrected 2009.
- [55] Digraaskar DA, "Simulatinos of flow over wind turbines," University of Massachusetts, 2010.
- [56] Tritton DJ, *Physical fluid dynamics*, Oxford Science Publications, 1988.
- [57] Hjertager BH, *Lecture Notes in OpenFOAM*, UiS, 2009.
- [58] George WK, *Lectures in Turbulence for the 21st Century*, Gothenburg, Sweden: Department of Applied Mechanics Chalmers University of Technology.
- [59] eFunda, "Properties of air," eFunda, Inc, 2012. [Online]. Available: http://www.efunda.com/materials/common_matl/show_gas.cfm?MatlName=Air0C. [Accessed February 2012].
- [60] Eugster AN, "Onshore lidar wind profile measurements at Utsire and their benefit for offshore wind turbine design and operation," University of Bergen, 2011.
- [61] Tennekes H, Lumley JL H, *A first course on turbulence, 11th edition*, MIT Press, 1987.
- [62] Hjertager BH, Interviewee, *Private communication*. [Interview]. 2012.
- [63] Ltd OpenCFD, *OpenFOAM: The Open Source CFD Toolbox. User Guide*, OpenFOAM Foundation, 2011.
- [64] Hjertager BH, Hjertager O LK, Solberg T, "Experimental and Computational Studies of Turbulent Mass Transfer in a Mixing Channel," *International Journal of Chemical Reactor Engineering*, vol. 6, 2008.
- [65] Kverneland R, Tøge GE, *Heat transfer analysis of EAL H317*, UiS: Project work for the the course MOM430, 2011.
- [66] Nygaard LP, *Writing for Scholars*, Universitetsforlaget, 2008.
- [67] Hjertager BH, *OpenFOAM Tutorials*, UiS, 2009.
- [68] Jenkins AD, "A Simplified Quasi-Linear Model for Wave Generation and Air-Sea Momentum Flux," *Journal of physical oceanography*, vol. 23, pp. 2001-2018, 1993.
- [69] Behrens T, *OpenFOAM's solvers for linear systems of equations*, Technical University of Denmark, 2009.
- [70] CFDComputing, "Power of Numerical Simulatino," CFDComputing.com © 2009-2012, [Online]. Available: http://cfdcomputing.com/documents/residual_plot_foam.htm. [Accessed April 2012].
- [71] Smedman A, Högström U, Bergström H, Rutgersson A, Kahma KK, Pettersson H, "A case study of air-sea interaction during swell conditions," *Journal of geophysical research*, vol. 104, no. 11, pp. 25,833-25,851,

1999.

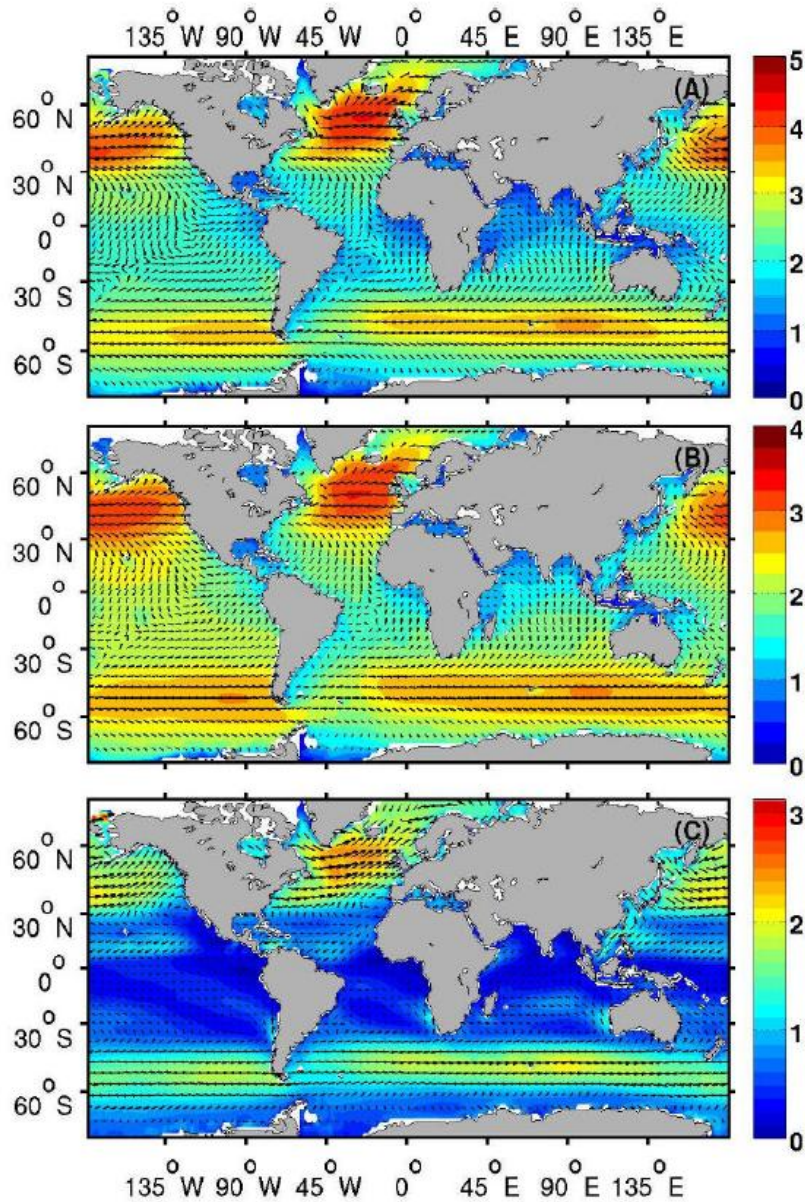
- [72] Sullivan PP et al, *A large eddy simulation model of high marine boundary layers above a spectrum of resolved moving waves*, 2010.
- [73] Kudryavtsev VN, Makin VK, "Impact of Swell on the Marine Atmospheric Boundary Layer," *Journal of physical oceanography*, vol. 34, pp. 934-949, 2004.
- [74] W. N. Hargreaves DM, "On the use of the k- ϵ model in commercial CFD software to model the neutral atmospheric boundary layer," *Journal of Wind Engineering and Industrial Aerodynamics*, vol. 74, pp. 232-237, 2007.
- [75] Foreman R, Emeis S, *The importance of humidity for stability at FINO 1 (North Sea)*, 2009.
- [76] LinkedIn, "OpenCFD," [Online]. Available: <http://www.linkedin.com/company/opencfd-limited>. [Accessed February 2012].
- [77] CFD Online, "Multigrid methods," February 2012. [Online]. Available: http://www.cfd-online.com/Wiki/Multigrid_methods. [Accessed March 2012].
- [78] Williams T, Kelley C, "Gnuplot," March 2012. [Online]. Available: <http://www.gnuplot.info/>. [Accessed April 2012].
- [79] Bird RB, Stewart WE, Lightfoot EN, *Transport Phenomena*, Wiley, 1960.
- [80] ENOVA SF, "Our history and mission," 2012. [Online]. Available: <http://www.enova.no/about-enova/259/0>. [Accessed June 2012].

APPENDICES

Appendix A: Seasonal average H_s for waves, swell and wind sea	55
Appendix B: Core equations k-E model.....	57
Appendix C: Pimple algorithm.....	58
Appendix D: Trial summary	59
Appendix E: p file	62
Appendix F: U file	63
Appendix G: k file.....	64
Appendix H: epsilon file	65
Appendix I: nut file	66
Appendix J: pointDisplacement.....	67
Appendix K: fvSolution	69
Appendix L: fvSchemes	71
Appendix M: controlDict file.....	72
Appendix N: blockMeshDict file	74
Appendix O: Startup scripts	76
Appendix P: endTime 250 s	77
Appendix Q: Grading of the mesh.....	79
Appendix R: Residual scripts	80
Appendix S: Residual plots	82
Appendix T: Mean vs. instantaneous values	84
Appendix U: Execution time.....	85
Appendix V: Sullivan et al. (2008), TKE.....	86

APPENDIX A: SEASONAL AVERAGE H_s FOR WAVES, SWELL AND WIND SEA.

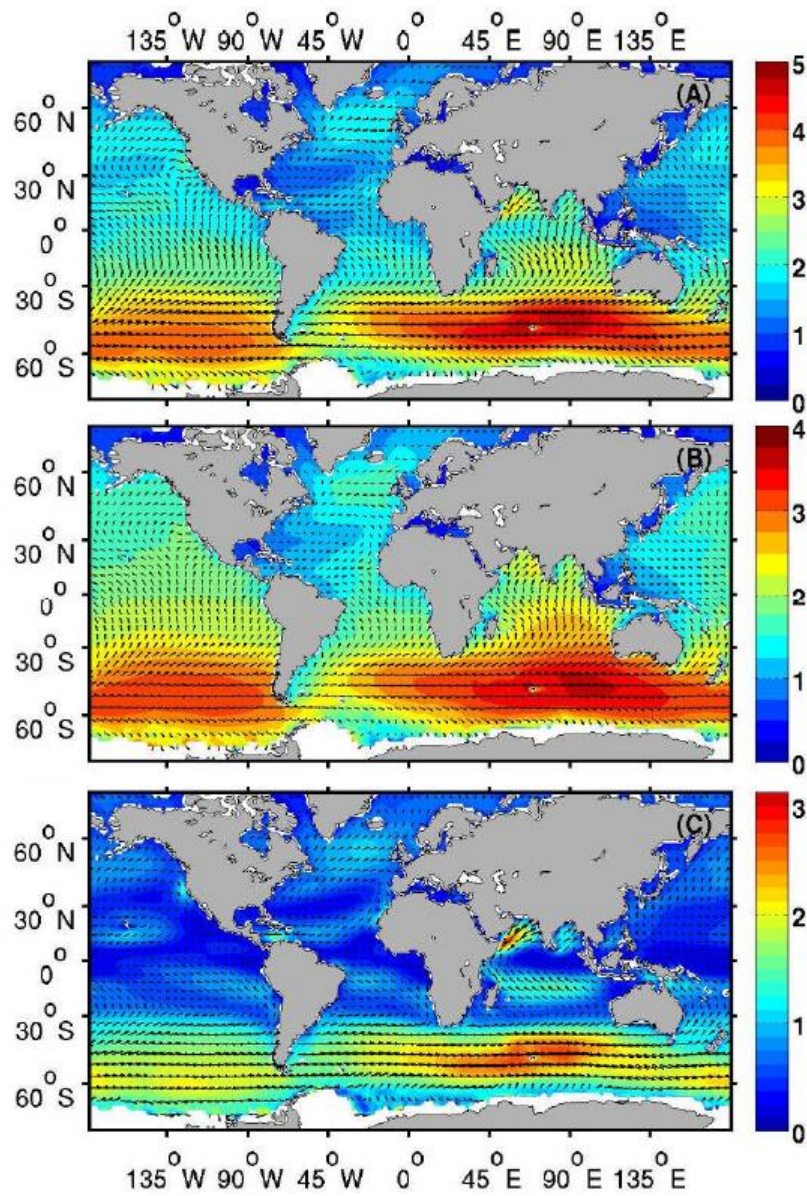
APPENDIX A.1: SEASONAL AVERAGES FOR DECEMBER, JANUARY AND FEBRUARY



The figure shows of H_s and θ_m (panel A), H_s^s and θ_m^s (panel B), and H_s^w and θ_m^w (panel C). H_s is in meters and θ is degrees.

Note: The arrows are scaled with the background fields. The color scales vary between the sub-figures [43].

APPENDIX A.2: SEASONAL AVERAGES FOR JUNE, JULY AND AUGUST



The figure shows of H_s and θ_m (panel A), H_s^s and θ_m^s (panel B), and H_s^w and θ_m^w (panel C). H_s is in meters and θ is degrees.

Note: The arrows are scaled with the background fields. The color scales vary between the sub-figures [43].

APPENDIX B: CORE EQUATIONS K-E MODEL

The steady state transport equations for turbulent kinetic energy, k , and turbulent dissipation, ε , are;

(eq. 29)

$$\frac{\partial}{\partial z} \left(\frac{\mu_t}{\sigma_k} \frac{\partial k}{\partial z} \right) + G_k - \rho \varepsilon = 0$$

(eq. 30)

$$\frac{\partial}{\partial z} \left(\frac{\mu_t}{\sigma_\varepsilon} \frac{\partial \varepsilon}{\partial z} \right) + C_{\varepsilon 1} G_k \frac{\varepsilon}{k} - C_{\varepsilon 2} \rho \frac{\varepsilon^2}{k} = 0$$

where;

(eq. 31)

$$G_k = \mu_t \left(\frac{\partial \mathbf{u}}{\partial z} \right)^2$$

expresses the production of turbulent kinetic energy [9].

APPENDIX C: PIMPLE ALGORITHM

Initial guess on the intermediate p^* , u^* , v^* , φ^*

1. Solve discretised momentum equation
2. Solve pressure correction equation
3. Correct pressure and velocity ($p = p^* + p'$ etc.)
4. Solve all other discretised transport equations
5. Check for convergence (if not repeat 1-4)

The PISO algorithm performs a second correction step. It starts with assuming pressure fields etc. as SIMPLE and then follows step 1-3 of the SIMPLE algorithm. From there it continues:

4. Solve second pressure correction equation (eq. 32).
5. Correct pressure and velocities
Set $p = p^{***}$ etc.
6. Solve all other discretised transport equations.

In the end both algorithms sets $p^* = p$ etc. and repeats until convergence [53].

The second corrector step solves the discretised momentum equations for u^{**} and v^{**} once more and obtaining the twice corrected velocity field u^{***} , v^{***} . Substituting these into the discretised continuity equation gives the second pressure correction equation [53].

$$a_{I,J}P''_{I,J} = a_{I+1,J}P''_{I+1,J} + a_{I-1,J}P''_{I-1,J} + a_{I,J+1}P''_{I,J+1} + a_{I,J-1}P''_{I,J-1} + b''_{I,J} \quad (\text{eq. 32})$$

From this one obtains the second correction field p'' and the twice corrected pressure field yields [53].

$$p^{***} = p^{**} + p'' = p^* + p' + p'' \quad (\text{eq. 33})$$

When using a transient PIMPLE solver one gets two loops; inner and outer. The inner loop differs from the PISO loop by solving the continuity equation [57].

Simulation	Description	executionTime [s]	fieldAverage [s]	Status
13	wFD_a2.1 n = 2 (2-1-1)'	3335		OK
14	wFD_a2.2 n = 3 (3-1-1)'	2342		OK
15	wFD_a2.3 n = 4 (2-2-1)'	2065		OK
<hr/>				
	<u>wFD_a4.x</u> <u>Various wind speed</u>			
16	wFD_a4.0 U = 5 m/s *	912	25	OK
	wFD_a4.1 U = 10 m/s (= wFD_a1.8 *)	1106,54	25	OK
17	wFD_a4.2 U = 15 m/s *	1759,2	25	OK
18	wFD_a4.3 U = 20 m/s *	2223,6	25	OK
19	wFD_a4.4 U = 25 m/s *	2773,2	25	OK
20	wFD_a4.5 U = 30 m/s *	3366	25	OK
21	wFD_a4.6 U = 35 m/s *	4120		OK
	U = 30 m/s, k = 3.4m ² /s ² , E =			
22	wFD_a4.7 0.3m ² /s ³ '	4440		OK
<hr/>				
	<u>wFD_a5.x</u> <u>Various wave amplitude</u>			
22	wFD_a5.0 a = 1 m '	2090		OK
23	wFD_a5.1 a = 1,5 m '	1900	15	OK
24	wFD_a5.2 a = 2 m '	2250		OK
	wFD_a5.3 a = 3 m (= wFD_a1.2 ')	2130		OK
25	wFD_a5.5 a = 4,5 m '	2750	15	OK
<hr/>				
	<u>wFD_a6.x</u> <u>Various wave length</u>			
26	wFD_a6.0 L = 20 m '	2715	10	OK
27	wFD_a6.1 L = 40 m (= wFD_a1.2 ')	2130		OK
28	wFD_a6.2 L = 80 m '	1900	30	OK
29	wFD_a6.3 L = 120 m '	1650	50	OK
30	wFD_a6.4 L = 160 m '	1540		OK
31	wFD_a6.5 L = 200 m '	1430		OK
<hr/>				
	<u>wFD_a7.x</u> <u>Various wave speed</u>			
32	wFD_a7.0 c = 6 m/s '	1600	30	OK
	wFD_a7.1 c = 8 m/s (= wFD_a1.2 ')	2130		OK
33	wFD_a7.2 c = 18 m/s '	2343	10	OK
34	wFD_a7.3 c = 24 m/s '	2700		OK
<hr/>				
	<u>wFD_a8.x</u> <u>Various wave state</u>			
	wFD_a8.0 a = 0, L = 0, c = 0 (= wFD_s0.1 ')	530	15	OK
35	wFD_a8.1 a = 1.0 m, L = 14 m, c = 5 m/s '	1590	30	OK
36	wFD_a8.2 a = 2.0 m, L = 28 m, c = 7 m/s '	1690	42	OK
37	wFD_a8.3 a = 3.0 m, L = 42 m, c = 8 m/s '	3920	52	OK
38	wFD_a8.4 a = 4.0 m, L = 56 m, c = 9 m/s '	2140	60	OK
39	wFD_a8.5 a = 5.0 m, L = 70 m, c = 10 m/s '	2325	67	OK

Simulation	Description	executionTime [s]	fieldAverage [s]	Status
<u>wFD_a9.x</u> <u>Sullivan 2008 setup</u>				
40	wFD_a9.0 c = 12,5 m/s *	69339	50	OK
41	wFD_a9.1 c = -12,5 m/s *	90836	50	OK
42	wFD_a9.2 c = 0 *	79830		OK
43	wFD_a9.3 c = 0, a = 0 *	53713	50	OK
44	wFD_a9.4 c = 0, 375 000 celler '	152214		OK
<u>wFD_ox</u> <u>Opposed</u>				
45	wFD_o0.0 c = -12 m/s	1600	15	OK
46	wFD_o0.2 Standard-case opposed *	1458	25	OK
<u>wFD_o8.x</u> <u>Various wave state</u>				
47	wFD_o8.1 a = 1.5 m, L = 20 m, c = -6 m/s *	1462	20	OK
48	wFD_o8.2 a = 1.5 m, L = 40 m, c = -6 m/s *	978	35	OK
49	wFD_o8.3 a = 1.5 m, L = 40 m, c = -8 m/s *	1024	25	OK
<u>wFD_o4.x</u> <u>Various wind speed</u>				
50	wFD_o4.0 U = 5 m/s *	1000,8	25	OK
	wFD_o4.1 U = 10 m/s (= wFD_o0.2 *)	1458	25	OK
51	wFD_o4.2 U = 15 m/s *	1977,6	25	OK
52	wFD_o4.3 U = 20 m/s *	2580	25	OK
53	wFD_o4.4 U = 25 m/s *	3129,6	25	OK
54	wFD_o4.5 U = 30 m/s *	3603,6	25	OK
<u>wFD_s0.x</u> <u>Stationary</u>				
55	wFD_s0.0 c = 0	848		OK
56	wFD_s0.1 c = 0, a = 0	530	15	OK

APPENDIX D.4: X-Z SLICE SHOWING VERTICAL PROFILE AT X = 210 M



APPENDIX E: P FILE

This file contains boundary and initial conditions for the pressure.

```
dimensions      [0 2 -2 0 0 0 0];

internalField   uniform 0;

boundaryField
{
    outlet
    {
        type      fixedValue;
        value     uniform 0;
    }
    inlet
    {
        type      zeroGradient;
    }
    ground
    {
        type      zeroGradient;
    }
    top
    {
        type      slip;
    }
    frontAndBack
    {
        type      slip;
    }
}
```

APPENDIX F: U FILE

This file contains boundary and initial conditions for the velocity.

```
dimensions      [0 1 -1 0 0 0 0];

internalField   uniform (10 0 0);

boundaryField
{
    ground
    {
        type      //fixedValue;
                  movingWallVelocity;
        value      uniform (0 0 0);
    }

    inlet
    {
        type      fixedValue;
        value      uniform (10.0 0 0);
    }

    outlet
    {
        type      inletOutlet;
        inletValue uniform (0 0 0);
        value      uniform (0 0 0);
    }
    top
    {
        type      slip;
    }
    frontAndBack
    {
        type      slip;
    }
}
```

APPENDIX G: K FILE

This file contains boundary and initial conditions for the TKE.

```
dimensions      [0 2 -2 0 0 0 0];

internalField   uniform 0.5;

boundaryField
{
    outlet
    {
        type      zeroGradient;
    }
    inlet
    {
        type      fixedValue;
        value     $internalField;
    }
    ground
    {
        type      kqRWallFunction;
        value     $internalField;
    }
    top
    {
        type      slip;
    }
    frontAndBack
    {
        type      slip;
    }
}
```

APPENDIX H: EPSILON FILE

This file contains boundary and initial conditions for the dissipation of TKE.

```
dimensions      [0 2 -3 0 0 0 0];

internalField   uniform 0.015;

boundaryField
{
    outlet
    {
        type      zeroGradient;
    }
    inlet
    {
        type      fixedValue;
        value     $internalField;
    }
    ground
    {
        type      epsilonWallFunction;
        value     $internalField;
    }
    top
    {
        type      slip;
    }
    frontAndBack
    {
        type      slip;
    }
}
```

APPENDIX I: NUT FILE

This file contains boundary and initial conditions for the turbulent eddy viscosity.

```
dimensions      [0 2 -1 0 0 0 0];

internalField   uniform 0;

boundaryField
{
    outlet
    {
        type          zeroGradient;
    }
    inlet
    {
        type          zeroGradient;
    }
    ground
    {
        type          nutkRoughWallFunction;
        Ks            uniform 0.2; //Ks = 20 z0
        Cs            uniform 0.5;
        value         uniform 0.0;
    }
    top
    {
        type          slip;
    }
    frontAndBack
    {
        type          slip;
    }
}
```

APPENDIX J: POINTDISPLACEMENT

This file describes the wave state.

```
dimensions      [0 1 0 0 0 0 0];

internalField   uniform (0 0 0);

boundaryField
{
    ground
    {
        type          waveFadeDisplacement;
        amplitude      (0 0 3.0);
        waveSpeed       8.0;
        waveLength      (20.0 0 0);
        totalWaveSectionLength 250.0;
        fadeLength      5.0;
        value           uniform (0 0 0);
    }
    inlet
    {
        type          zeroGradient;
    }
    top
    {
        type          fixedValue;
        value         uniform (0 0 0);
    }
    outlet
    {
        type          zeroGradient;
    }
}
```

```
frontAndBack
{
    type          zeroGradient;
}

}
```

APPENDIX K: FVSOLUTION

This file contains the equation solvers, tolerances and algorithms.

```
solvers
{
  p
  {
    solver          GAMG;
    tolerance       1e-7;
    relTol          0.01;
    smoother        GaussSeidel;
    nPreSweeps      0;
    nPostSweeps     2;
    cacheAgglomeration on;
    agglomerator    faceAreaPair;
    nCellsInCoarsestLevel 10;
    mergeLevels     1;
  }

  pFinal
  {
    $p;
    tolerance       1e-7;
    relTol          0;
  }

  "(U|k|epsilon)"
  {
    solver          PBiCG;
    preconditioner  DILU;
    tolerance       1e-06;
    relTol          0.1;
  }

  "(U|k|epsilon)Final"
  {
    $U;
    tolerance       1e-06;
    relTol          0;
  }

  cellDisplacement
  {
    solver          GAMG;
    tolerance       1e-5;
    relTol          0;
    smoother        GaussSeidel;
    cacheAgglomeration true;
    nCellsInCoarsestLevel 10;
    agglomerator    faceAreaPair;
    mergeLevels     1;
  }
}

PIMPLE
{
  nOuterCorrectors 3;
  nCorrectors       1;
  nNonOrthogonalCorrectors 1;
}
```

```
relaxationFactors
{
    "U.*"      1.;
    "k.*"      1.;
    "epsilon.*" 1.;
}
```

```
cache
{
    grad(U);
}
```

APPENDIX L: FVSCHEMES

This file contains the numerical schemes.

```
ddtSchemes
{
    default          Euler;
}

gradSchemes
{
    default          Gauss linear;
    grad(p)          Gauss linear;
    grad(U)          Gauss linear;
}

divSchemes
{
    default          none;
    div(phi,U)       Gauss upwind grad(U);
    div((nuEff*dev(T(grad(U)))) Gauss linear;
    div(phi,epsilon) Gauss upwind;
    div(phi,k)       Gauss upwind;
}

laplacianSchemes
{
    default          Gauss linear limited 0.333;
}

interpolationSchemes
{
    default          linear;
}

snGradSchemes
{
    default          limited 0.333;
}

fluxRequired
{
    default          no;
    p;
}
```

APPENDIX M: CONTROL DICT FILE

This file contains input parameters essential for the creation of the database.

```

libs ("libwaveFadeDisplacement.so");

application      pimpleDyMFoam;

startFrom        latestTime;

startTime        0;

stopAt           endTime;

endTime          100;

deltaT           0.01;

writeControl     adjustableRunTime;

writeInterval    0.5;

purgeWrite       50;

writeFormat      ascii;

writePrecision   6;

writeCompression uncompressed;

timeFormat       general;

timePrecision    6;

runTimeModifiable yes;

adjustTimeStep  yes;

maxCo            0.5;

functions
{
fieldAverager1
    {
        type          fieldAverage;
        functionObjectLibs ( "libfieldFunctionObjects.so" );
        enabled        true;
        cleanRestart    true;
//      outputControl  timeStep;
//      outputControl  outputTime;
//      outputInterval  1000;
        fields
        (
            U
            {
                mean          on;
                prime2Mean    on;
                base           time;
            }

            k
            {

```

```
        mean          on;  
        prime2Mean    on;  
        base          time;  
    }  
};  
};  
}
```

APPENDIX N: BLOCKMESHDICTIONARY FILE

This file contains input for the generation of the mesh.

```
convertToMeters 1;

vertices
(
    (0 0 0)
    (250 0 0)
    (250 25 0)
    (0 25 0)
    (0 0 50)
    (250 0 50)
    (250 25 50)
    (0 25 50)
);

blocks
(
    hex (0 1 2 3 4 5 6 7) (250 1 50) simpleGrading (1 1 5)
);

edges
(
);

boundary
(
    top
    {
        type patch;
        faces
        (
            (4 5 6 7)
        );
    }

    inlet
    {
        type patch;
        faces
        (
            (0 4 7 3)
        );
    }

    outlet
    {
        type patch;
        faces
        (
            (2 6 5 1)
        );
    }

    ground
    {
        type wall;
        faces
        (
```

```
        (0 3 2 1)
    );
}

frontAndBack
{
    type patch;
    faces
    (
        (1 5 4 0)
        (3 7 6 2)
    );
}
);

mergePatchPairs
(
);
```

APPENDIX O: STARTUP SCRIPTS

NB! If the case is copied one has to make sure the scripts are made executable by using `chmod 777 Allclean` and `chmod 777 Allrun` when running the case for the first time.

APPENDIX O.1: ALLCLEAN

```
# Source tutorial clean functions
. $WM_PROJECT_DIR/bin/tools/CleanFunctions

cleanCase
rm -rf VTK
rm -rf constant/cellToRegion constant/polyMesh/sets
rm -rf constant/polyMesh/sets
rm -rf constant/cellLevel
rm -rf constant/cellZones
rm -rf constant/faceZones
rm -rf constant/faces
rm -rf constant/neighbour
rm -rf constant/owner
rm -rf constant/pointZones
rm -rf constant/points
rm -rf constant/refinementHistory
rm -rf constant/surfaceIndex
rm -rf 0/yPlus
rm -rf 0/y
rm -rf testSample
rm -rf constant/polyMesh/boundary
```

APPENDIX O.2: ALLRUN

```
# Source tutorial run functions

. $WM_PROJECT_DIR/bin/tools/RunFunctions

# single processor calculation
#runApplication blockMesh
#runApplication snappyHexMesh -overwrite
#runApplication setSet -batch makeZones
#runApplication setsToZones -noFlipMap
#runApplication simpleWindFoam
#runApplication yPlusRAS

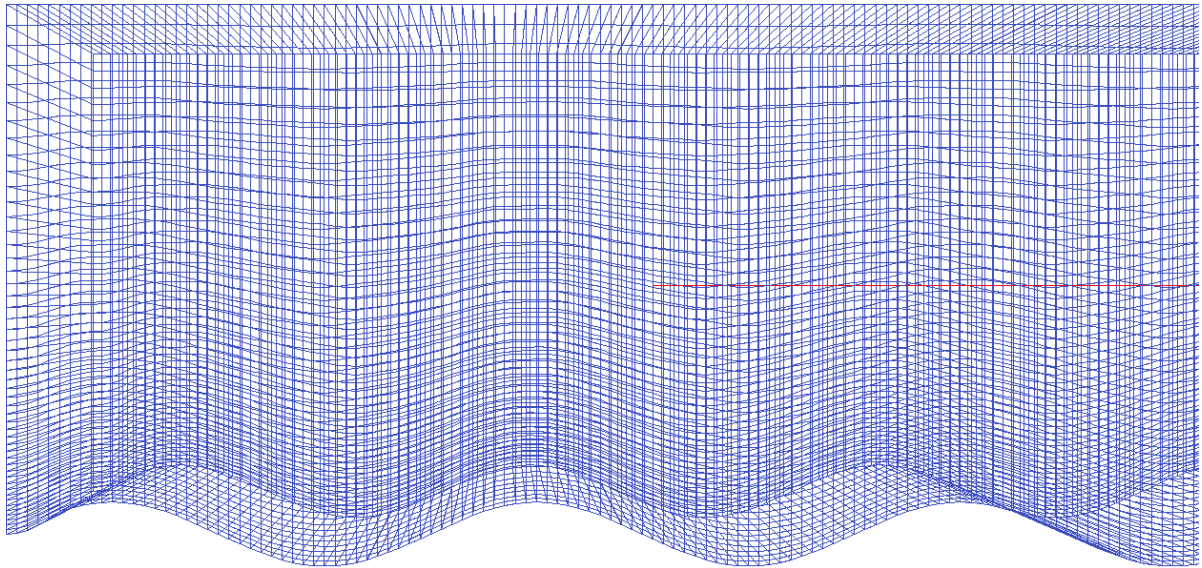
# parallel computing
runApplication blockMesh
#runApplication snappyHexMesh -overwrite
runApplication setSet -batch makeZones
runApplication setsToZones -noFlipMap
runApplication decomposePar
#runParallel simpleWindFoam 4
runParallel pimpleDyMFoam 4
runApplication reconstructPar
runApplication yPlusRAS
```

APPENDIX P: ENDTIME 250 s

z	profile_125_k		profile_125_U	
	k	U _x	endTime 100	endTime 250
0,43307	2,00608	2,00615	2,31901	2,31898
1,30175	1,87702	1,87707	3,36143	3,36151
2,1755	1,43816	1,43821	3,5076	3,50776
3,05435	1,26673	1,26679	3,769	3,7692
3,93834	1,3239	1,32397	4,23752	4,23774
4,82749	1,45669	1,45675	4,80959	4,80982
5,72184	1,58945	1,5895	5,41819	5,41844
6,62141	1,69283	1,69287	6,0354	6,03565
7,52623	1,75491	1,75493	6,64833	6,64859
8,43634	1,76877	1,76877	7,25141	7,25167
9,35177	1,73687	1,73685	7,84125	7,84152
10,2725	1,66089	1,66085	8,41444	8,41471
11,1987	1,54534	1,54528	8,96699	8,96725
12,1303	1,39788	1,39781	9,49352	9,49377
13,0673	1,22939	1,22931	9,98674	9,98697
14,0098	1,05441	1,05433	10,4371	10,4373
14,9577	0,88858	0,88851	10,8323	10,8325
15,9113	0,74605	0,746	11,1593	11,1595
16,8704	0,63603	0,63598	11,4079	11,4081
17,8351	0,56027	0,56024	11,5759	11,576
18,8054	0,51384	0,51382	11,6714	11,6715
19,7814	0,4881	0,4881	11,7093	11,7094
20,7631	0,4747	0,47469	11,7082	11,7082
21,7505	0,46725	0,46725	11,6826	11,6826
22,7437	0,46196	0,46196	11,6425	11,6425
23,7427	0,45699	0,45699	11,5954	11,5954

24,7476	0,45164	0,45164	11,5452	11,5452
25,7583	0,4458	0,4458	11,4942	11,4942
26,7749	0,4396	0,4396	11,444	11,4439
27,7975	0,43326	0,43326	11,3949	11,3949
28,826	0,427	0,427	11,3477	11,3477
29,8606	0,42099	0,42099	11,3024	11,3024
30,9011	0,41538	0,41538	11,2592	11,2592
31,9478	0,41027	0,41027	11,2179	11,2179
33,0006	0,40571	0,40571	11,1786	11,1786
34,0595	0,4017	0,4017	11,1409	11,1409
35,1246	0,3982	0,3982	11,105	11,105
36,1959	0,39517	0,39517	11,0709	11,0709
37,2735	0,39257	0,39257	11,0386	11,0385
38,3574	0,39034	0,39034	11,0079	11,0079
39,4476	0,38844	0,38844	10,9789	10,9789
40,5442	0,38683	0,38683	10,9514	10,9514
41,6472	0,38544	0,38544	10,9253	10,9253
42,7567	0,38426	0,38426	10,9006	10,9006
43,8726	0,38324	0,38324	10,8771	10,8771
44,995	0,38235	0,38235	10,8547	10,8547
46,124	0,38159	0,38159	10,8332	10,8332
47,2596	0,38094	0,38094	10,8126	10,8126
48,4018	0,38038	0,38038	10,7926	10,7926

APPENDIX Q: GRADING OF THE MESH



The figure shows x-z slice of the wireframe.

APPENDIX R: RESIDUAL SCRIPTS

```

set title "Final residuals"
set logscale y
set yrange [+0.0000000001 : 1]
set xlabel "timeStep"
set ylabel "Residual value"
plot "UxFinalRes_0" w l lw 3
replot "UyFinalRes_0" w l lw 3
replot "UzFinalRes_0" w l lw 3
replot "pFinalRes_0" w l lw 3
replot "kFinalRes_0" w l lw 3
replot "epsilonFinalRes_0" w l lw 3
set terminal png
set output 'FinalRes.png'
replot

```

```

set title "Residuals"
set logscale y
set yrange [+0.0001 : 1]
set xlabel "timeStep"
set ylabel "Residual value"
plot "Ux_0" w l lw 3
replot "Uy_0" w l lw 3
replot "Uz_0" w l lw 3
replot "p_0" w l lw 3
replot "k_0" w l lw 3
replot "epsilon_0" w l lw 3
set terminal png
set output 'Residuals.png'
replot

```

```

set title "Local and global continuity errors"
set logscale y
set yrange [+0.000000000001 : 0.00001]
set xlabel "timeStep"
set ylabel "Error value"
plot "contGlobal_0" w l lw 3
replot "contLocal_0" w l lw 3
set terminal png
set output 'Cont.Errors.png'
replot

```

```

set title "Residual iterations"
set yrange [+0.001 : 7]
set xlabel "timeStep"
set ylabel "Number of iterations"
plot "UxIters_0" w l lw 3
replot "UyIters_0" w l lw 3
replot "UzIters_0" w l lw 3
replot "pIters_0" w l lw 3
replot "kIters_0" w l lw 3
replot "epsilonIters_0" w l lw 3
set terminal png
set output 'Residualiterations.png'
replot

```

```

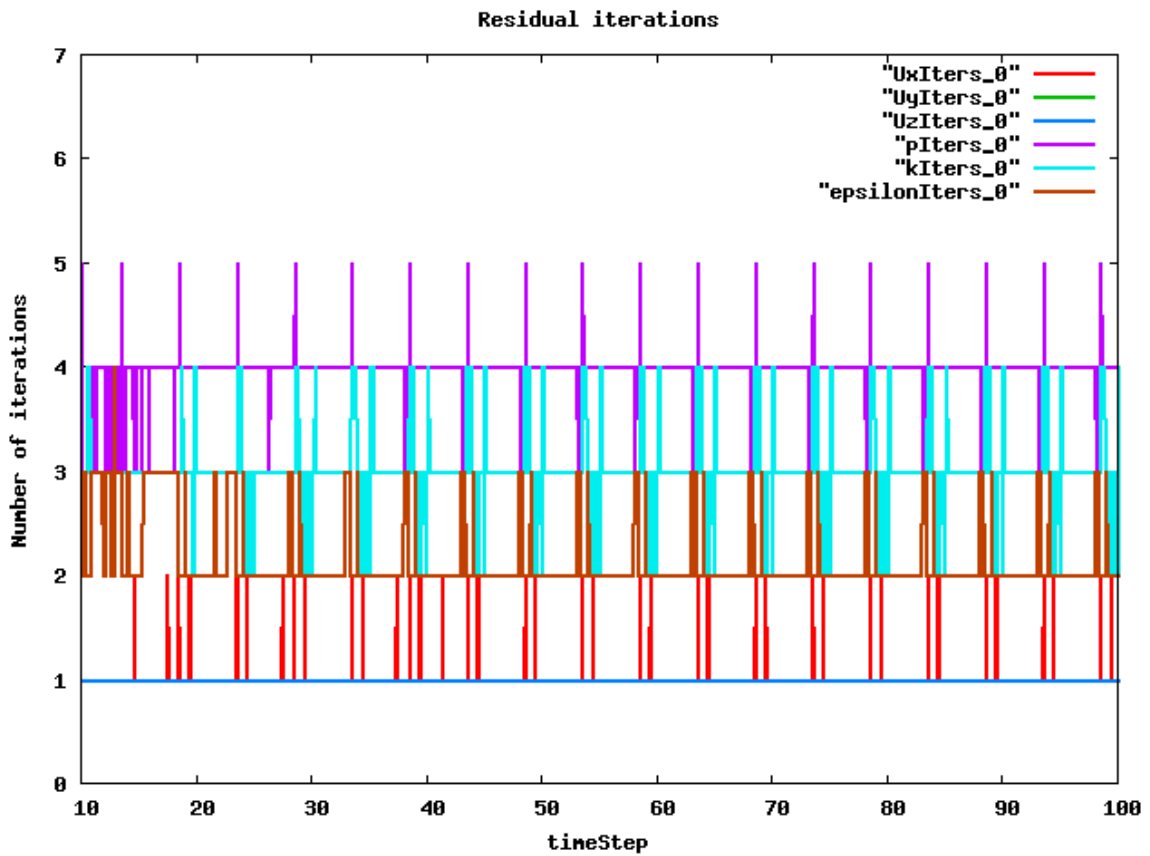
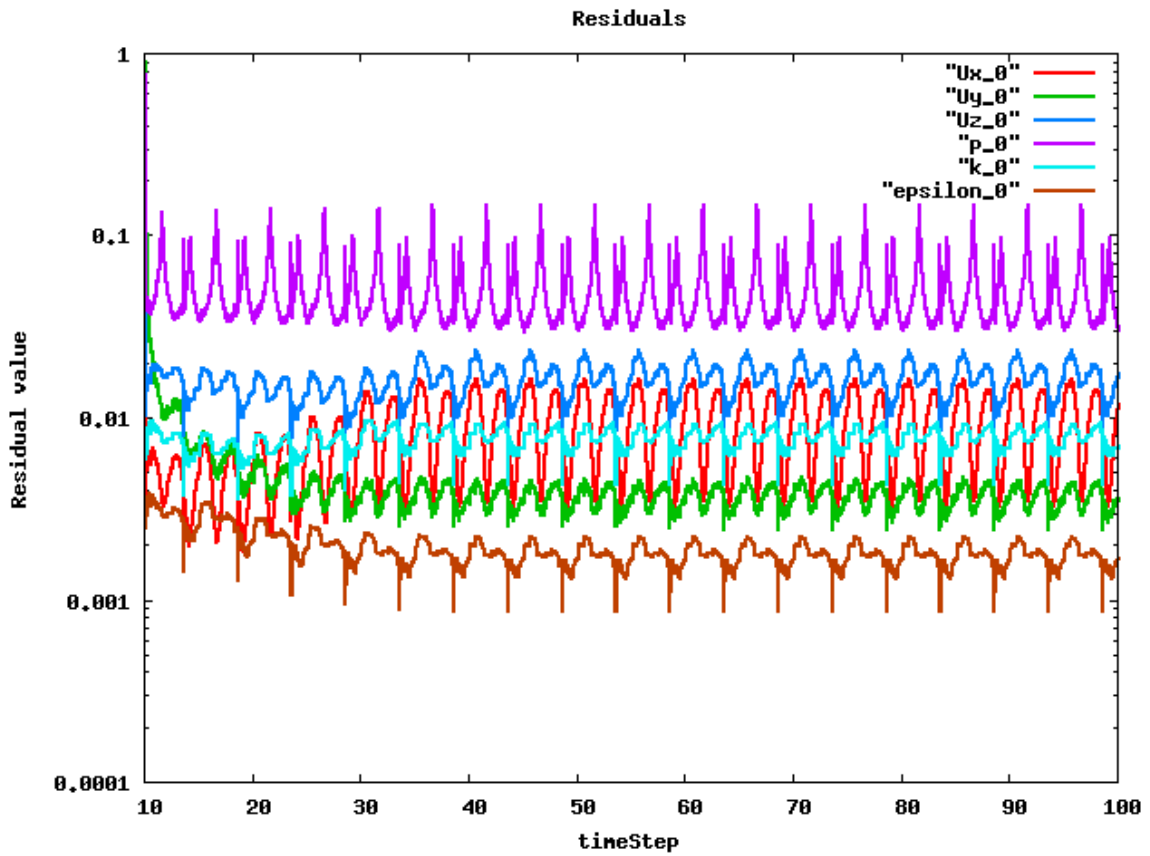
set title "Max Courant number"
set logscale y
set xlabel "timeStep"
set ylabel "Residual value"
plot "CourantMax_0" w l lw 3

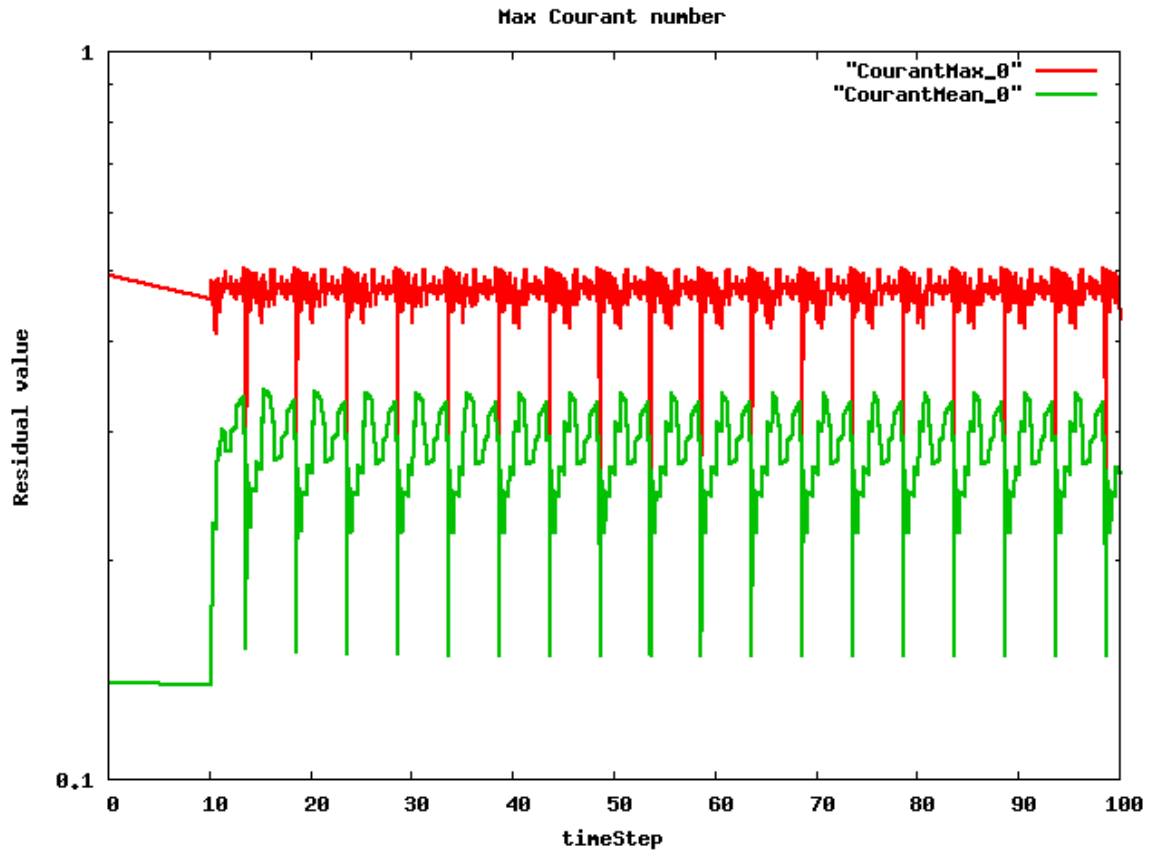
```

```
replot "CourantMean_0" w l lw 3
set terminal png
set output 'MaxCourant.png'
replot

set title "Max Courant number"
set logscale y
set xlabel "timeStep"
set ylabel "Residual value"
plot "CourantMax_0" w l lw 3
replot "CourantMean_0" w l lw 3
set terminal png
set output 'MaxCourant.png'
replot
```

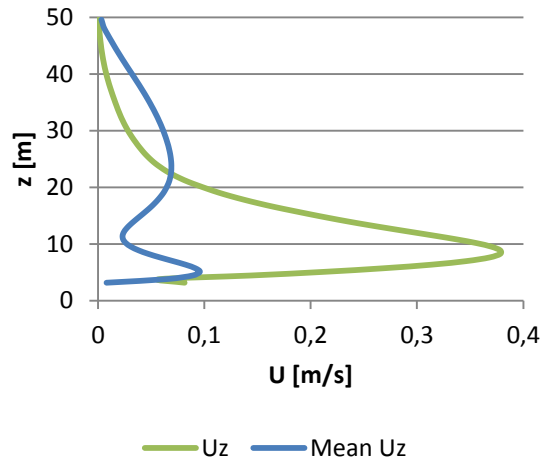
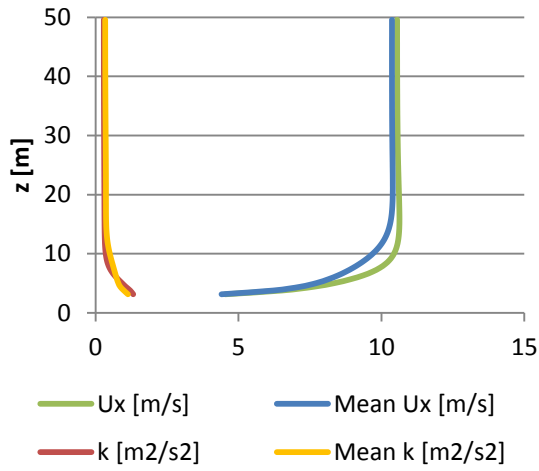
APPENDIX S: RESIDUAL PLOTS





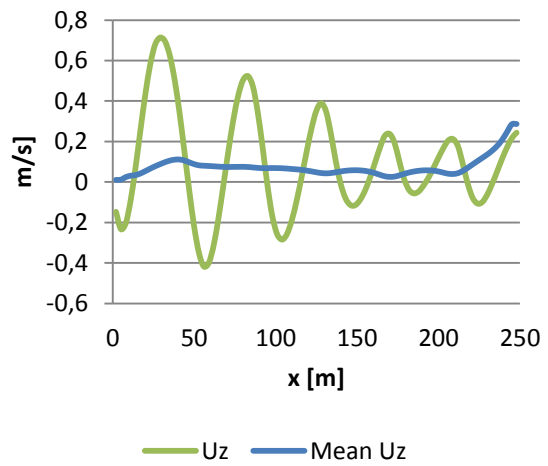
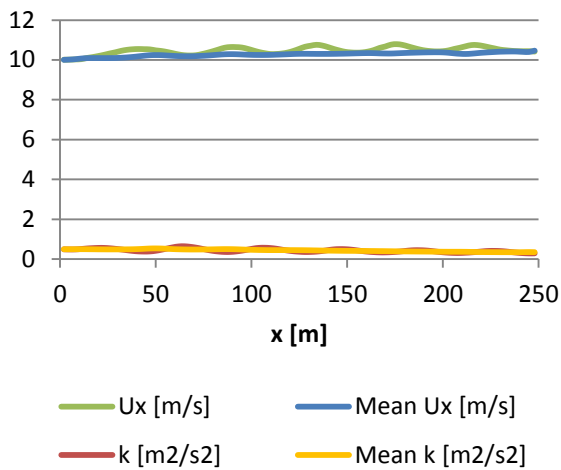
APPENDIX T: MEAN VS. INSTANTANEOUS VALUES

APPENDIX T.1: VERTICAL PROFILES AT x = 210 M



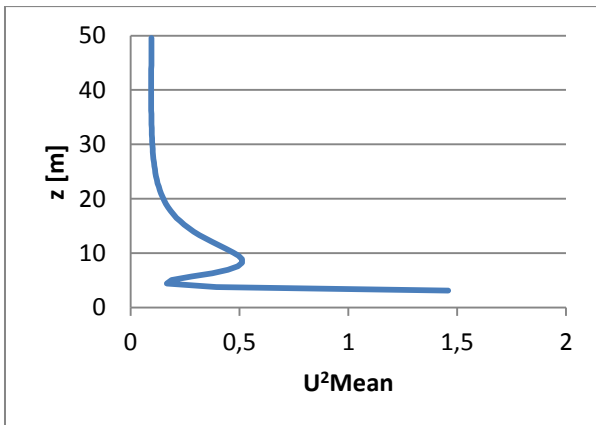
The figures show the “standard-case”, aligned situation.

APPENDIX T.2: HORIZONTAL PROFILES AT z = 15 M



The figures show the “standard-case”, aligned situation.

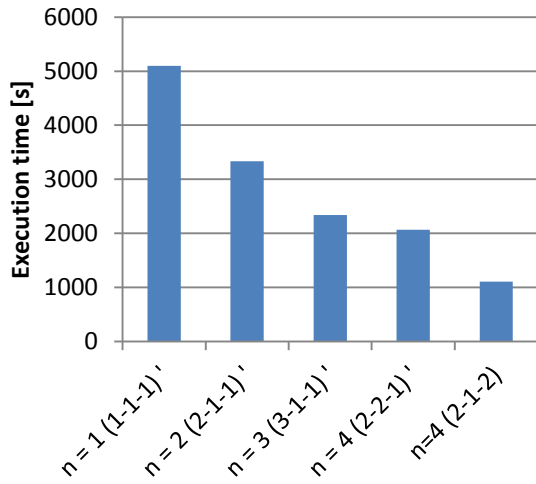
APPENDIX T.3: U²MEAN



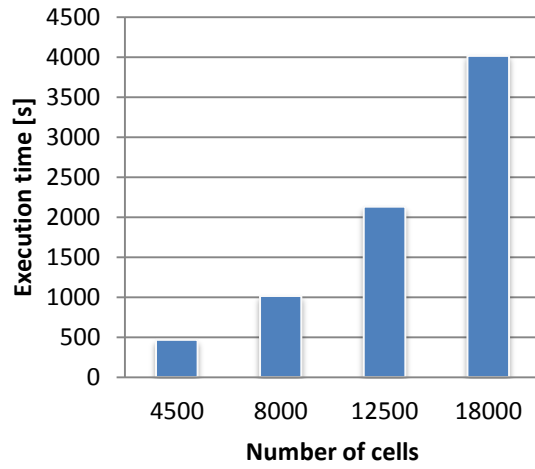
The figure shows the “standard-case”, aligned situation.

APPENDIX U: EXECUTION TIME

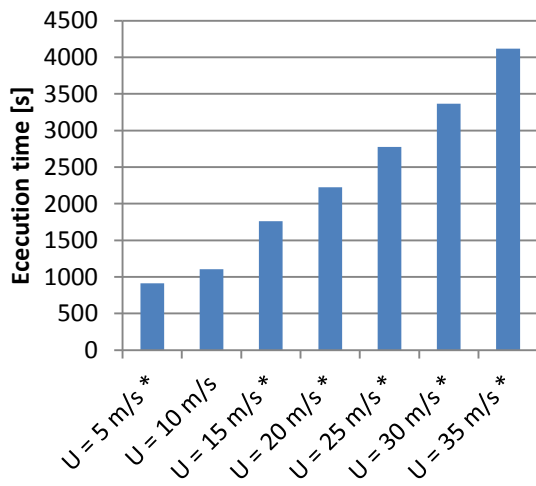
Running in parallell



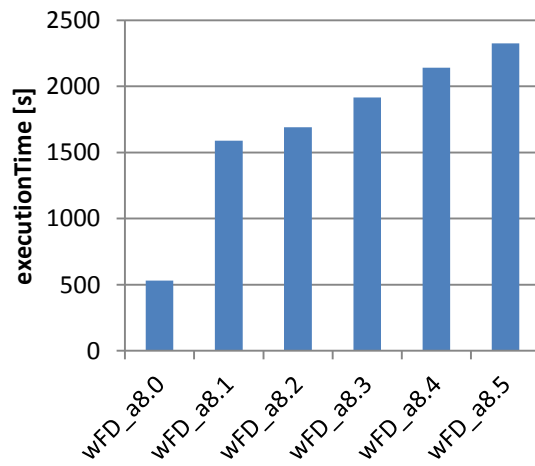
Grid independence study



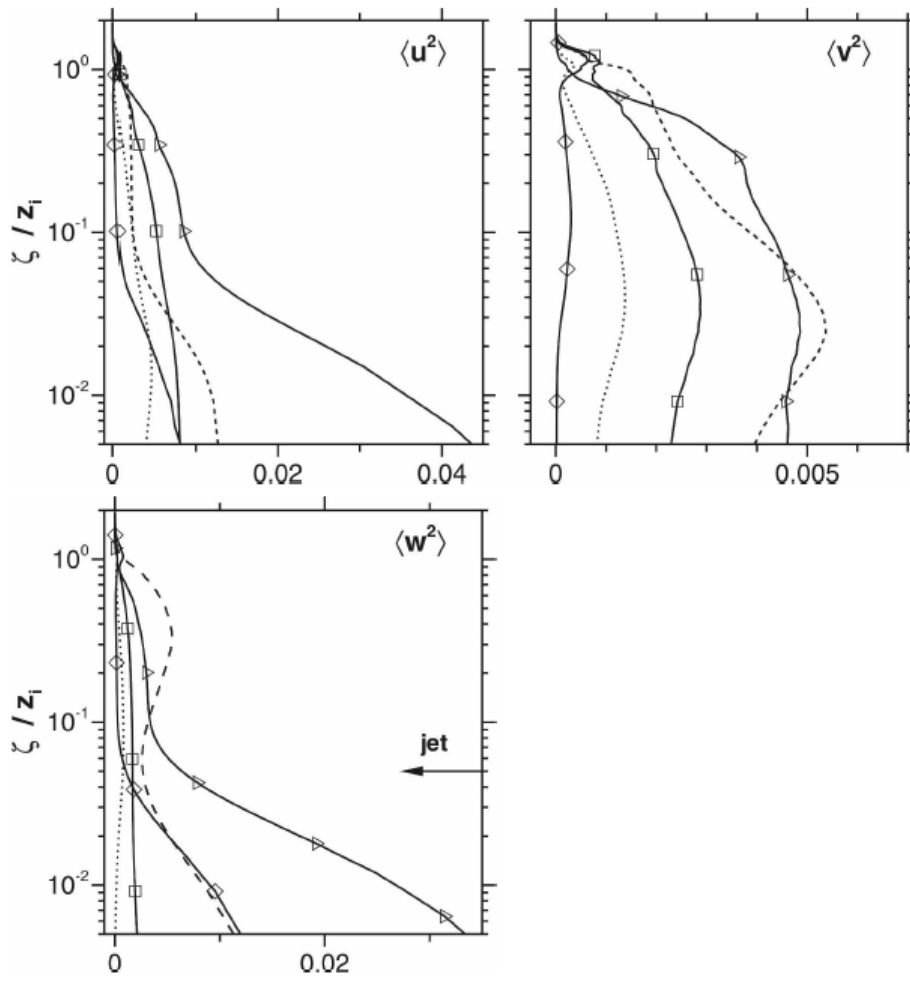
Case 1.A



Case 2.D



APPENDIX V: SULLIVAN ET AL. (2008), TKE



The figure shows vertical profiles of the non-dimensional resolved variance components $\bar{u}'_i \bar{u}'_j / U_g^2$. The results are shown in linear-logarithmic coordinates with the vertical axis non-dimensionalized by the initial height of the inversion $z_i = 400$ m. The situations of interest are aligned (diamonds) and opposed with wave propagation (triangles), stationary (squares) and no waves (dotted). The horizontal arrow shows the vertical location of the low-level wind maximum in the aligned situation.